

# Investigation of a Multilevel Inverter for Electric Vehicle Applications

OSKAR JOSEFSSON

*Department of Energy and Environment*  
CHALMERS UNIVERSITY OF TECHNOLOGY  
Göteborg, Sweden 2015



THESIS FOR THE DEGREE OF DOCTOR OF PHILOSOPHY

**Investigation of a Multilevel Inverter  
for Electric Vehicle Applications**

OSKAR JOSEFSSON



Division of Electric Power Engineering  
Department of Energy and Environment  
CHALMERS UNIVERSITY OF TECHNOLOGY  
Göteborg, Sweden 2015

**Investigation of a Multilevel Inverter  
for Electric Vehicle Applications**

Oskar Josefsson  
ISBN 978-91-7597-174-2

© Oskar Josefsson, 2015.  
except where otherwise stated.  
All rights reserved

Doktorsavhandlingar vid Chalmers tekniska högskola  
Ny serie nr 3855  
ISSN 0346-718X

Department of Energy and Environment  
CHALMERS UNIVERSITY OF TECHNOLOGY  
SE-412 96 Göteborg  
Sweden  
Telephone + 46 (0)31 772 10 00

Printed by Chalmers Reproservice,  
Gothenburg, Sweden, 2015

*To my family*



# Abstract

Electrified vehicles on the market today all use the classical two-level inverter as the propulsion inverter. This thesis analyse the potential of using a cascaded H-bridge multilevel inverter as the propulsion inverter. With a multilevel inverter, the battery is divided into several parts and the inverter can now create voltages in smaller voltage levels than the two-level inverter. This, among other benefits, reduces the EMI spectrum in the phase cables to the electric machine. It is also shown that these H-bridges can be placed into the battery casing with a marginal size increase, and some addition of the cooling circuit performance. The benefit is that the separate inverter can be omitted.

In this thesis, measurements and parameterisations of the battery cells are performed at the current and frequency levels that are present in a multilevel inverter drive system. The derived model shows a great match to the measurements for different operating points and frequencies.

Further, full drive cycle simulations are performed for the two analysed systems. It is shown that the inverter loss is greatly reduced with the multilevel inverter topology, mainly due to the possibility to use MOSFETs instead of IGBTs. However, the battery packs in a multilevel inverter experience a current far from DC when creating the AC-voltages to the electric machine. This leads to an increase of the battery loss but looking at the total inverter-battery losses, the system shows an efficiency improvement over the classical two-level system for all but one drive cycle. In the NEDC drive cycle the losses are reduced by 30 % but in the demanding US06 drive cycle the losses are increased by 11 % due to the high reactive power demand at high speed driving. These figures are valid for a plug-in hybrid with a 50 km electrical range where no filter capacitors are used. In a pure electric vehicle, there is always an energy benefit of using a multilevel converter since a larger battery will have lower losses. By placing capacitors over the inputs of the H-bridges, the battery current is filtered. Two different capacitor chemistries are analysed and experimentally verified and an improvement is shown, even for a small amount of capacitors and especially at cold operating conditions.

## **Keywords**

Electric Vehicle (EV), Plug-in Electric Vehicle (PEV), Multilevel Inverter (MLI), Two-level Inverter (TLI), Integrated Charger, Drive Cycle, Efficiency, Battery modelling, LiFePO<sub>4</sub>.



# Acknowledgement

The financial support from the Swedish Energy Agency and Volvo Car Corporation is gratefully appreciated.

I would like to direct a very special thank you to my examiner and main supervisor Torbjörn Thiringer, the support and discussions are truly appreciated. Thank you for taking the time! I would also like to thank Sonja Lundmark as co-supervisor and Anders Lindskog for the introduction of the project.

A big thank you to all the colleagues at the division of Electric Power Engineering, the atmosphere among the colleagues is excellent and it has been a privilege to work here and to just sit down and have a chat in the lunch room. A sincere thank you to my very special friends and office colleagues David Steen and Elias Hartvigsson for making it a pure joy coming to work.

At last I want to thank my family and friends. It is you who add value to my life, thank you for being part of it!

Oskar Josefsson  
Göteborg, February 2015



# Contents

<b>Abstract</b>	<b>v</b>
<b>Acknowledgement</b>	<b>vii</b>
<b>List of Nomenclatures</b>	<b>xiii</b>
<b>1 Introduction</b>	<b>1</b>
1.1 Background . . . . .	1
1.2 Purpose of work . . . . .	4
1.3 Contributions . . . . .	4
<b>2 Drive system topologies and control</b>	<b>7</b>
2.1 Two-level inverter . . . . .	7
2.1.1 PWM . . . . .	7
2.1.2 Third harmonic injection(THI)-PWM . . . . .	8
2.2 Cascaded full-bridge multilevel inverter . . . . .	10
2.2.1 Fundamental Selective Harmonic Elimination (FSHE)	11
2.2.2 Balancing strategy for MLI . . . . .	16
2.3 Electric machine and torque control . . . . .	16
2.4 Charger . . . . .	17
<b>3 Inverter loss modeling</b>	<b>21</b>
3.1 Power electronic components . . . . .	21
3.1.1 MOSFET losses . . . . .	22
3.1.2 IGBT losses . . . . .	23
3.1.3 Diode losses . . . . .	25

3.1.4	Miscellaneous power electronic components . . . . .	26
3.2	Two level inverter (TLI) . . . . .	26
3.2.1	Conduction losses . . . . .	27
3.2.2	Switching losses . . . . .	28
3.2.3	Total losses . . . . .	29
3.3	Multilevel inverter (MLI) . . . . .	29
3.3.1	Conduction losses . . . . .	29
3.3.2	Switching losses . . . . .	30
3.3.3	Total losses . . . . .	31
<b>4</b>	<b>Case setup &amp; inverter waveform verification</b>	<b>33</b>
4.1	Small PEV reference vehicle . . . . .	33
4.1.1	Electric machine . . . . .	34
4.1.2	Test vehicle battery . . . . .	35
4.1.3	Filter capacitors for the MLI system . . . . .	37
4.1.4	Test vehicle power electronic components . . . . .	38
4.1.5	Drive cycle presentation . . . . .	39
4.2	Experimental system . . . . .	39
4.3	Experimental base verification . . . . .	41
4.3.1	Output waveforms and harmonics . . . . .	41
4.3.2	Total Harmonic Distortion . . . . .	45
4.3.3	Balancing using the experimental setup . . . . .	46
4.3.4	Battery current verification with the experimental setup	48
<b>5</b>	<b>Small PEV power train loss evaluation</b>	<b>51</b>
5.1	Efficiency calculations . . . . .	51
5.1.1	Inverter . . . . .	51
5.1.2	Battery . . . . .	56
5.1.3	Combined inverter and battery losses . . . . .	59
5.1.4	Loss comparison . . . . .	61
5.1.5	Charging . . . . .	65
5.2	Drive cycle evaluation . . . . .	66
5.2.1	NEDC . . . . .	66
5.2.2	FTP75 . . . . .	68
5.2.3	HWFET . . . . .	69

5.2.4	US06 . . . . .	70
5.2.5	Comparison between proposed topology and classical inverter . . . . .	71
5.3	40 kWh battery . . . . .	72
5.4	Slim sizing of the inverter semiconductors . . . . .	74
<b>6</b>	<b>Battery loss modeling</b>	<b>77</b>
6.1	Parameter extraction . . . . .	78
6.2	Verification in experimental system . . . . .	79
6.2.1	Representative operating points for the full scale system	83
6.2.2	Battery model performance in the MLI . . . . .	84
6.3	Drive cycle evaluation for battery losses . . . . .	86
<b>7</b>	<b>Filter capacitor influence</b>	<b>89</b>
7.1	System overview . . . . .	89
7.1.1	Battery cell . . . . .	89
7.2	Capacitor configurations . . . . .	92
7.3	Model verification . . . . .	94
7.4	Frequency analysis . . . . .	95
7.5	Drive cycle analysis . . . . .	98
7.6	Cold climate performance . . . . .	102
<b>8</b>	<b>Proposal for packaging of the inverter-battery unit and its cooling circuit</b>	<b>107</b>
8.1	Two-level inverter . . . . .	109
8.2	MOSFET equipped cell voltage monitor modules . . . . .	110
8.2.1	Thermal resistance of the MOSFETs . . . . .	113
8.2.2	Thermal properties of the PCB . . . . .	113
8.2.3	Heat sink for CVMM . . . . .	113
8.2.4	Cooling circuit temperature increase due to battery losses	114
8.2.5	Resulting thermal analysis for the MOSFET-enhanced CVMM system . . . . .	114
8.3	Slim sized inverters . . . . .	115
<b>9</b>	<b>Conclusions</b>	<b>117</b>
<b>10</b>	<b>Future Work</b>	<b>119</b>

**References**

**121**

# List of Nomenclatures

The following list presents nomenclatures that are used throughout this thesis:

<b>MLI</b>	Multilevel Inverter
<b>TLI</b>	Two-level Inverter
<b>THI</b>	Third Harmonic Injection
<b>FSHE</b>	Fundamental Selective Harmonic Elimination
<b>CVMM</b>	Cell Voltage Monitor Module
<b>ESR</b>	Equivalent Series Resistance
$V_{CE}$	IGBT collector emitter voltage
$I_C$	IGBT collector current
$V_{tIGBT}$	IGBT fixed voltage drop
$R_{onIGBT}$	IGBT resistance
$V_{DS}$	MOSFET drain source voltage
$I_D$	MOSFET drain current
$R_{onMOSFET}$	MOSFET resistance
$T_{on}$	Transistor turn on time
$T_{off}$	Transistor turn off time
$V_{Diode}$	Diode anode cathode voltage
$I_{Diode}$	Diode anode current
$V_{tDiode}$	Diode fixed voltage drop

$R_{Diode}$	Diode resistance
$Q_{rr}$	Diode reverse recovery charge
$K_{rr}$	Diode reverse recovery equivalent loss parameter
$E_{RR}$	Diode reverse recovery energy
$V_{drr}$	Diode voltage at reverse recovery
$E_{on}$	Transistor turn on energy
$E_{off}$	Transistor turn off energy
$C$	Capacitance of one MLI H-bridge input capacitor
$n$	Number of H-bridges for one phase in the MLI
$N$	Number of voltage levels one phase can produce
$V_{DC_{ML}}$	Input voltage for each H-bridge in the MLI
$V_{DC_{TL}}$	Input voltage for the TLI
$U_{phase_{RMSMAX}}$	Maximum phase voltage that can produced by the inverters
$U_{phase_{RMSMAXTHI}}$	Maximum phase voltage that can produced by the TLI when controlled with third harmonic injection
$h$	Harmonic number
$U_{ML}(h)$	Harmonic value at harmonic $h$ for the MLI
$\alpha_1$	Angle where the first H-bridge is turned on
$\alpha_2$	Angle where the second H-bridge is turned on
$\alpha_3$	Angle where the third H-bridge is turned on
$V_{out}(t)$	Inverter reference output voltage
$\hat{U}$	Amplitude of inverter reference output voltage
$\omega$	Frequency of inverter reference output voltage
$\varphi$	Phase difference of inverter output voltage and current
$a$	Magnitude of third harmonic component



$\hat{I}$	Amplitude of inverter output current
$f_{fund}$	Frequency of inverter reference output voltage
$T_f$	Time period of inverter reference output voltage
$f_{sw}$	Switching frequency of the TLI
$m_a$	Modulation index
$D(t)$	Duty cycle of the TLI
$P_{condIGBT_{1H}}$	Conduction losses for the upper transistor in the TLI
$P_{condIGBT_{1L}}$	Conduction losses for the lower transistor in the TLI
$P_{condDiode_{1H}}$	Conduction losses for the upper diode in the TLI
$P_{condDiode_{1L}}$	Conduction losses for the lower diode in the TLI
$P_{conductionIGBT_{s1}}$	Average conduction losses for the transistors in one leg in the TLI
$P_{conductionDiodes_1}$	Average conduction losses for the diodes in one leg in the TLI
$P_{switchIGBT_{1H}}$	Switching losses for the upper transistor in the TLI
$P_{switchIGBT_{1L}}$	Switching losses for the lower transistor in the TLI
$P_{rrDiode_{1H}}$	Switching losses for the upper diode in the TLI
$P_{rrDiode_{1L}}$	Switching losses for the lower diode in the TLI
$P_{switchIGBT_{s1}}$	Average switching losses for the transistors in one leg in the TLI
$P_{rrDiodes_1}$	Average switching losses for the diodes in one leg in the TLI
$P_{LossTLI}$	Average total loss in the TLI
$V_{drop}$	Phase voltage drop in the MLI
$P_{conductionMLI}$	Conduction losses for the MLI
$E_{on_{\alpha_{1...6}}}$	Turn on energy at switching instance 1 to 6

$E_{off\alpha_{1...6}}$	Turn off energy at switching instance 1 to 6
$E_{rr\alpha_{1...6}}$	Reverse recovery energy at switching instance 1 to 6
$P_{switchMLI}$	Average switching losses in the MLI
$P_{LossML}$	Average total loss in MLI
$u_{sd}$	Stator voltage in d-direction
$u_{sq}$	Stator voltage in q-direction
$i_{sd}$	Stator current in d-direction
$i_{sq}$	Stator current in q-direction
$\psi_m$	Magnetic flux density
$p$	Pole pairs
$R_s$	Stator resistance
$L_d$	Inductance in d-direction
$L_q$	Inductance in q-direction
$U_{phaseRMS}$	Machine phase voltage
$I_{phaseRMS}$	Machine phase current
$\angle \vec{u}_s$	Angle of machine voltage relative to machine position
$\angle \vec{i}_s$	Angle of machine current relative to machine position
$\Delta T_{waterTLIinverter}$	Temperature rise in water due to the inverter losses in the TLI case
$\Delta T_{waterTLIbattery}$	Temperature rise in water due to the battery losses in the TLI case
$\Delta T_{waterMLIinverter}$	Temperature rise in water due to the inverter losses in the MLI case
$\Delta T_{waterMLIbattery}$	Temperature rise in water due to the battery losses in the MLI case
$\Delta T_{waterMLItotal}$	Temperature rise in water due to the combined battery and inverter losses in the MLI case

$\Delta T_{J-A}$	Temperature difference between the junctions and ambient air for the transistors
$T_{junction_{TLIinverter}}$	Temperature of the junctions of the IGBTs in the TLI
$P_{TLIinverter}$	TLI inverter losses used for thermal calculations
$P_{TLIbattery}$	TLI battery losses used for thermal calculations
$P_{MLIinverter}$	MLI inverter losses used for thermal calculations
$P_{H-bridge}$	MLI inverter losses for each H-bridge used for thermal calculations
$P_{MLIbattery}$	MLI battery losses used for thermal calculations
$\frac{\Delta V}{\Delta t}$	Water flow in cooling circuit
$C_p$	Specific heat capacity of the cooling fluid
$\rho$	Density of the cooling fluid
$R_{th_{J-water}}$	Thermal resistance from the junctions of the transistors to the cooling water
$R_{th_{J-C}}$	Thermal resistance from the junctions of the transistors to the case
$R_{th_{C-H}}$	Thermal resistance from the cases of the transistors to the heat sink
$R_{th_{H-A}}$	Thermal resistance from the heat sink of the transistors to ambient air
$R_{th_{J-A}}$	Combined thermal resistance from the junctions of the transistors to ambient air



# Chapter 1

## Introduction

### 1.1 Background

Electrified vehicles (EVs) are occupying an increasing part of the market share for personal vehicles, both in the form of hybrid electric vehicles (HEVs) but also pure battery electric vehicles (BEVs). Lately, most focus has been spent on the development of vehicles that can be charged from the network, plugin electric vehicles (PEVs), with a driving distance of at least 20-30 km on pure electricity. For the automotive manufacturer, one important challenge is to develop a PEV with as long driving distance as possible for a given battery size i.e. high drive train efficiency. A lot of development resources are spent on developing an aerodynamic vehicle which still attracts the customer in terms of design and storage capabilities. Additionally, focus has to be spent on optimising the energy conversion from the chemical energy in the battery, through the power electronics as electrical power and finally to mechanical energy by the electrical machine.

To be able to optimise all the power conversions in the vehicle, good understanding of the behaviour of the different components are needed. It is also important to understand the operating points in terms of speed and torque that the car is operated at, so that the components are optimised not only at one operating point, but for the average of the whole operating region. A lot of research has been done in modeling the efficiency for electrified vehicles. Some simulation aspects are shown in [1] and [2], dealing with both the physical modeling as well as the electrical one. It is shown that even though it is important to analyse the efficiency of each component, the different components determine the operation points for each other and therefore the complete drive train must be incorporated in the vehicle efficiency analysis since it is the combined total efficiency which is of interest.

The control strategy used for the power electronics highly affects the losses in the vehicle as is shown by [3] and [4]. Also, depending on how the vehicle is used, some control strategies show a better performance. Having accurate models of the different components, but also how they affect each other depending on the control and operating point is of high importance in order to achieve a good simulation result [5]. Since the car is operated in a wide speed range, simulations of full drive cycles are important to evaluate the actual performance in the whole operating range and not only a few operating points. It is of course also vital that the models are verified against measurements and/or empirical data, other models and analytical calculations wherever possible.

To be able to compare how good an electric vehicle drive train is, test procedures are needed. Different test procedures for EVs are explained in [6] where it is stated that one problem for making accurate testing is to describe equivalent fuel consumptions for an electric vehicle since other vehicles are measured in liters of fossil fuel per kilometer. Today, PEVs are often counted as zero-emission vehicles but this might in the future change since a lot of the electricity is still produced by fossil fuels, and then the energy efficiency in the electrified vehicles will be of much more importance than today. In order to compare different electric drive trains it is important to spend the focus to minimizing the drive train losses and thereby get the lowest fuel consumption for a given vehicle.

In order to evaluate different topologies of EVs, an analysis of the market is needed [7]. It is stated by [8] and [9] that all EVs on the market today use the same power electronic concept; the two-level inverter (TLI). However, it is indicated that an increase in research is expected for the power electronics used for propulsion to develop competitive EVs [10]. The power electronics placed in an EV need to meet some special requirements and is discussed in [11] and [12]. Different power electronic packages, for example, give different advantages in terms of cooling which also affect the design of the cooling circuits and packaging possibilities.

In EVs, as mentioned in the previous paragraph, the TLI is the far most used power electronic converter today. It uses six power electronic switches to create the voltage needed for an electrical machine, see Fig. 2.1. Due to the demand of a high voltage level, IGBTs are often used. The IGBTs have relatively high losses compared to MOSFETs at this power level, so it would be beneficial to be able to use the MOSFET technology at a lower voltage level. One way to be able to use MOSFETs is to divide the battery into smaller units with lower voltage, and use one inverter for each battery module. The outputs of the inverters are then series connected to be able to create the voltage magnitude that the electric machine requires. This inverter type is called a cascaded multilevel inverter (MLI) and can be seen

in Fig. 2.4. This converter topology is becoming popular for power system applications such as FACTS and HVDC [13]. How suitable this inverter type is as propulsion inverter in electrified vehicles is however not evaluated so far.

Regarding battery representation, a battery can electrically be described in many ways, see [14], [15], [16] and [17]. In simulations of electrified vehicles, the far most common way is to describe it as a purely resistive voltage source with an open source voltage that is state of charge(SOC) dependant. However, the battery currents are far from DC [18] when using a MLI to propel the vehicle and these models do not consider the frequency components that the battery modules are subject to in a MLI drive system (1 Hz-10 kHz). Sometimes, in literature, the Randles model is used, [19], [20], [21] and [22], to account for the filtering effects the battery is subjected to during a drive cycle of the car which are in the range of seconds to minutes. A common way to capture the high frequency behaviour of the battery is to use electrochemical impedance spectroscopy. A problem with this method is that the parameters are subtracted at very low current levels, and might give different results than a subtraction made at the operating point at which the battery will be used in [23].

The PEV must have a charger to be able to charge the battery from the grid. In the great majority of the electrical vehicles out on the market today, the charger is a stand-alone component. It can be either an on-board charger that is located in the vehicle, or it can be an off-board charger located at different locations in the infrastructure. It is advantageous if the propulsion power electronics can be used also for charging; then the separate power electronics in the on board charger is not needed, and space needs as well as cost can be reduced. This has been showed to work with the TLI, see [24], however, the consequences when doing the same with the MLI, is not yet evaluated for a vehicle application.

The advantages and benefits of using a MLI in an electrified vehicle are discussed in [25] and in [26]. It is stated that the MLI has almost no electromagnetic interference (EMI) and is therefore a safer and more accessible choice to have in a vehicle. One other benefit is for example if one battery cell in the battery pack has a lower capacity compared to the rest of the cells, the whole battery pack does not need to be used at the capacity level of this weakest single cell. In a TLI this is the case but for the MLI only the cells within that battery group would need to be used less. The efficiency is also discussed in general terms but without any quantification. The efficiency is only predicted to be higher than the one for the TLI.

Obviously the MLI has advantages regarding EMI and battery utilisation, however, traceable results of the benefits of using a MLI in electrified vehicles from an energy point of view, and to what extent, is missing.

## 1.2 Purpose of work

A possibility to improve the total electric drive train efficiency and thus to utilize the energy stored in the battery of the electrified vehicle, could be to use the MLI concept as an alternative to the commonly used TLI. However, this needs too be quantified using comparative calculations for these two inverter topologies, using adequate model representations.

The purpose of this thesis is therefore to analyse the opportunities of using a MLI as the propulsion inverter in an electrified vehicle. The main focus is made on the energy efficiency when using different drive cycles and control strategies in order to quantify the energy losses. Furthermore, since the MLI inverter loads the battery with a current far from DC, an adequate loss model must be parameterized, verified and implemented.

Finally, an important objective is to propose how the MLI could be practically implemented and to make a crude thermal evaluation.

## 1.3 Contributions

According to the author the following contributions not found in previous available literature have been made with this thesis.

- Quantified the losses in an electric power train for the MLI in a complete torque-speed map, and put it in relation to the losses in a TLI. This analysis is done, including the battery energy loss consequences, in order to determine the difference between the systems for all relevant operating points of the electric vehicle. Results also presented in [27] and [28].
- Performed an analysis of the electrical losses for the combined battery-inverter systems for different drive cycles in order to be able to quantify the energy losses for the two systems. Results also presented in [28].
- Presented a proposal of implementation of the MLI system, removing the discrete inverter, and performed a rough conservative thermal evaluation of the suitability of such an implementation.
- Derived and quantified the importance of using an adequate battery representation for the MLI vehicle application, and verified these losses experimentally.
- Determined the energy loss consequences when using different types of capacitors to alleviate the battery cells. This analysis is done both theoretically and experimentally and the resulting EMI consequences are also indicated.



- Experimentally verified the battery current waveforms from a MLI and experimentally proved the possibility to balance the battery groups during driving.



## Chapter 2

# Drive system topologies and control

To evaluate the performance and efficiency of a multilevel inverter (MLI) used as the propulsion inverter, knowledge about the system is needed. To draw conclusions about the benefits, a reference system is also needed. Therefore, two different inverter topologies will be studied in this thesis. The cascaded multilevel inverter (MLI) and the classical two-level inverter (TLI).

### 2.1 Two-level inverter

The TLI is by far the most common propulsion inverter used in electrified vehicles. It consists of six switches divided into three legs, see Fig. 2.1. An anti-parallel diode is placed in anti-parallel to each switch to allow current to flow in the reverse direction as well. The battery is connected to the input of the inverter supplying it with a voltage level of  $V_{DC_{TL}}$ . The inverter can produce eight different states depending on the control of the six switches, where two are the zero voltage vector.

#### 2.1.1 PWM

When a TLI is controlled in PWM-mode, three voltage references are created as can be seen in Fig. 2.2. Observe that in Fig. 2.2 the switching frequency is very low, only 1 kHz for illustrative purposes, for a PEV it is typically around 10 kHz. These references are compared to a triangular wave with a frequency equal to the switching frequency. When the reference is higher than the triangular wave, the upper side switch in that leg is activated (turned

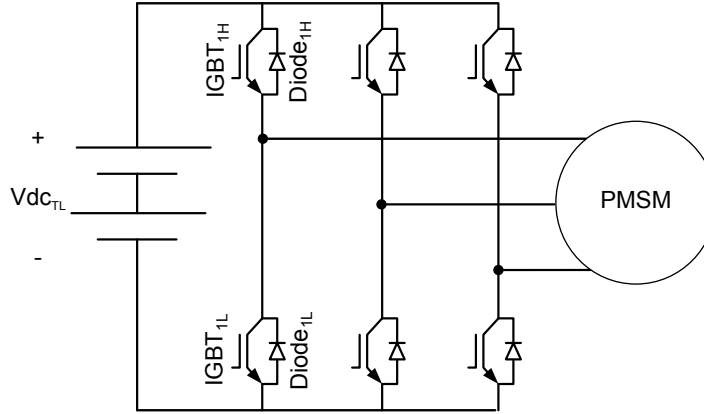


Figure 2.1: Topology of a two-level inverter (TLI).

on), otherwise the lower side switch is activated. It is also possible to use over modulation, which means that the reference wave is above the peak of the triangular wave. This could be for one or several triangle wave periods. During the time the reference wave is above the peak of the triangular wave, no switching instances will occur and low frequency harmonics will be present which is an unwanted feature. However, in a vehicle application it is anyway typically used at the most high-power operating points in order to get some extra power to the wheels. In this thesis, over modulation is not considered for simplicity and noise reasons.

In order to provide a minimum on and off time of the modules, and to account for the blanking time and the losses in the inverter a margin of 10% is set on the output voltage to guarantee controllability of the current. The maximum rms phase motor voltage will then be equal to

$$U_{phase_{RMSMAX}} = 0.9 \frac{V_{DC_{TL}}}{2\sqrt{2}}. \quad (2.1)$$

### 2.1.2 Third harmonic injection(THI)-PWM

When a TLI is controlled in THI-PWM-mode, three voltage references are created and compared to a triangular wave with a frequency equal to the switching frequency in the same way as in the PWM strategy as can be seen in Fig. 2.3. By adding a third harmonic to the voltage references, the neutral point of the machine is altered up and down. The machine will not react to this third harmonic since the neutral point of the machine is not connected to the inverter neutral point, instead it is the line-to-line voltages that the

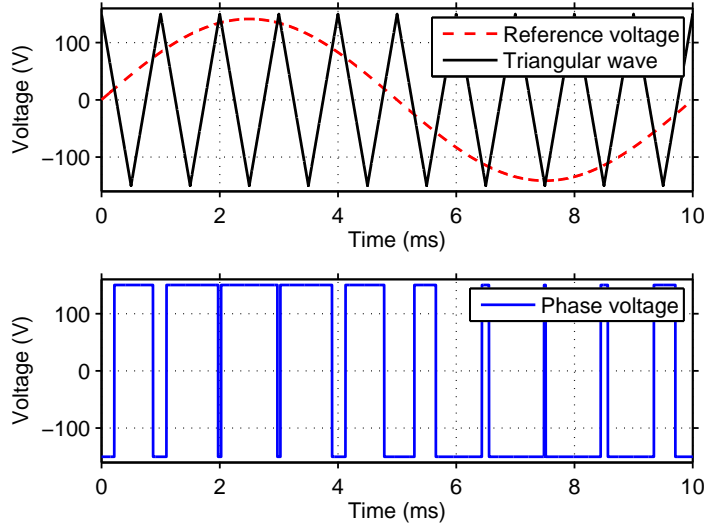


Figure 2.2: Theoretical inverter waveforms when using PWM-control at 1 kHz switching frequency and a 300 V DC-link voltage level.

machine will react to. The advantage is that the DC-bus voltage can be utilized to a higher extent. Also in this case a margin of 10% is used on the output voltage to guarantee controllability of the current. The maximum rms phase motor voltage, with "low-harmonic" free voltages, will then be equal to

$$U_{phaseRMSMAXTHI} = 0.9 \frac{V_{DC_{TL}}}{\sqrt{3}\sqrt{2}} \quad (2.2)$$

which is about 15 % higher than the pure sinusoidal PWM strategy with no drawbacks.

In order to describe the phase voltage used, the modulation index  $m_a$  is typically utilised. For the two-level inverter the modulation index  $m_a$  is in this thesis defined according to

$$U_{phase} = m_a \frac{V_{DC_{TL}}}{\sqrt{3}\sqrt{2}} \quad (2.3)$$

where  $m_a$  can go up to 1.0 without entering over modulation. Observe that there exists other types of definitions in literature on the modulation index,  $m_a = 1.0$  could also correspond to when (2.1) is fulfilled.

Running the inverter with THI-PWM will give a duty cycle  $D$  (the ratio of the active time between the upper and lower transistor in the leg) according

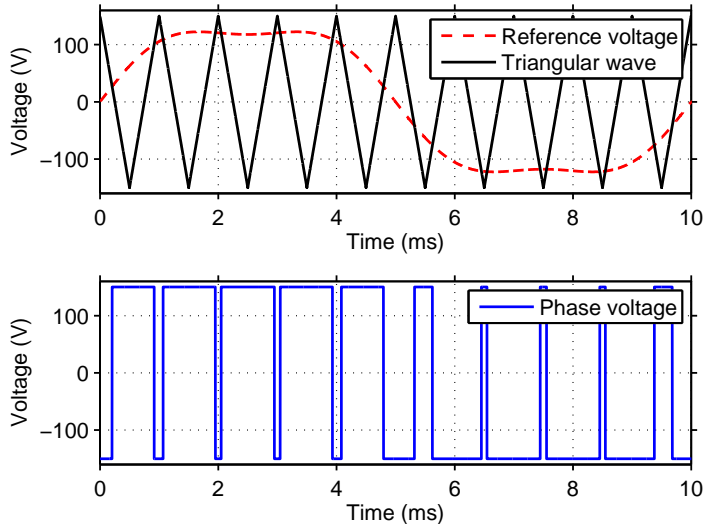


Figure 2.3: Theoretical inverter waveforms when using THI-PWM-control at 1 kHz switching frequency and a 300 V DC-link voltage level.

to

$$D(t) = 0.5 + \frac{U_{out}(t)}{V_{DC_{TL}}} \quad (2.4)$$

where the third harmonic addition is added to the reference wave  $U_{out}(t)$ .

It could be mentioned that there are also other methods to find the switching instances, such as direct torque control. The results will be very much the same in terms of losses so here the THI-PWM modulation strategy described above will be used.

## 2.2 Cascaded full-bridge multilevel inverter

A great benefit with the multilevel inverter is that the switches in each H-bridge only switches zero or four times the fundamental frequency compared to the TLI where all switches switch at least 20 times per fundamental period. This gives much lower switch losses. Moreover, since each switch is subjected to a lower voltage level, the losses are even lower in spite of the larger number of switches in the MLI.

A multilevel inverter can be built up using many different topologies. The one analysed in this thesis is the cascaded multilevel inverter, see Fig. 2.4. It consists of series connected H-bridges which can be controlled independently.

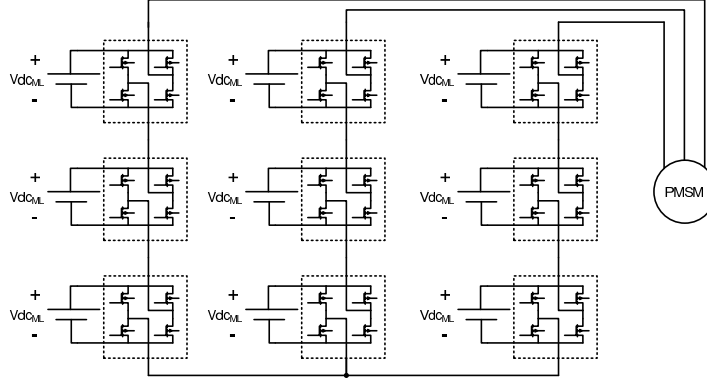


Figure 2.4: Topology of a 7-level multilevel inverter (MLI)

Every H-bridge has a separate energy storage with a voltage of  $V_{DC_{ML}}$  attached to it and by controlling the switches in the H-bridge in different ways, one bridge can create  $V_{DC_{ML}}$ ,  $-V_{DC_{ML}}$ , 0 and open circuit, to its output. Since many H-bridges are connected in series, the total voltage can vary in several steps. If the voltage sources are equal, the number of voltage levels,  $N$ , becomes

$$N = 2n + 1 \quad (2.5)$$

where  $n$  is the number of H-bridges for each phase.

### 2.2.1 Fundamental Selective Harmonic Elimination (FSHE)

The MLI used in this thesis will be controlled with Fundamental Selective Harmonic Elimination (FSHE), see [29], [30]. By choosing when to turn on the different H-bridges in the MLI, the amplitude of the fundamental frequency as well as the harmonics are controlled. For an  $N$ -level inverter the amplitude of the fundamental frequency and  $\frac{N-3}{2}$  number of harmonics can be controlled [29]. Since the motor acts as a phase current low pass filter, it is of importance to minimize the lowest harmonics since these are less effectively filtered by the machine inductances.

The waveform built up by the 7-level MLI analyzed in this thesis can be seen in Fig. 2.5. The angles  $\alpha_1$ ,  $\alpha_2$  and  $\alpha_3$  describe the instances when the H-bridges should be activated.

The fourier series expansion of the signal for the different harmonics,  $h$ , can be written as

$$U_{ML}(h) = \frac{4}{h\pi} [V_{DC_{ML}} \cos(h\alpha_1) + V_{DC_{ML}} \cos(h\alpha_2) + V_{DC_{ML}} \cos(h\alpha_3)] \quad (2.6)$$

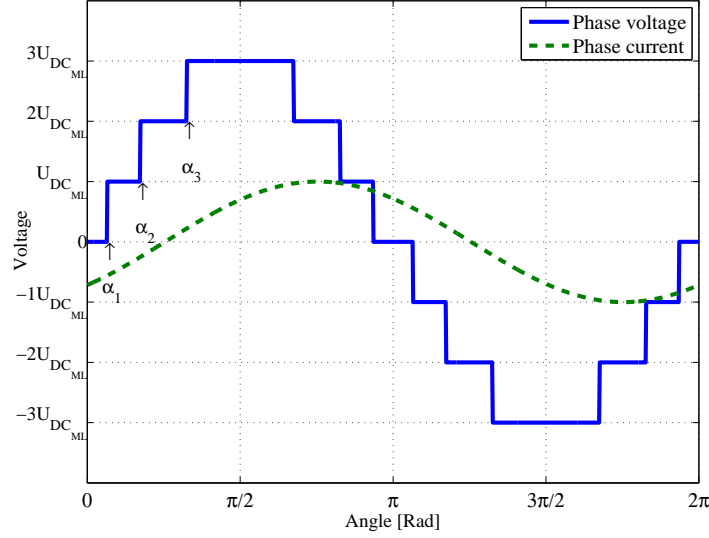


Figure 2.5: Simulated phase voltage from 7-level MLI.

according to [29] when assuming that the DC-voltages are equal for all the H-bridges. Setting the amplitude of harmonic 5 and 7 to zero in the above equation system, the switching angles and resulting harmonic spectrum can be calculated for different amplitudes of the fundamental frequency. For the MLI operated with FSHE, the modulation index  $m_a$  is defined according to

$$U_{phase} = m_a \frac{V_{DC_{ML}} \cdot n}{\sqrt{2}}. \quad (2.7)$$

The resulting angles for this case can be seen in Fig. 2.6. The reason for the discontinuities in the curves are due to that for some operating points more than one solution exist, see [29], and that the solver tracks two different curves during the sweep of  $m_a$  and randomly returns one from each curve. However, it can be seen that the 5th and 7th harmonics are eliminated for all modulation indexes in this range. The modulation index can go up to 1.07 without loosing the control to eliminate the 5th and 7th harmonic. Using a modulation index below 0.5, the control over the harmonics are also lost but are minimized with a prioritization on the 5th harmonic. The maximum voltage the inverter can produce with a margin of 10% can accordingly be expressed as

$$U_{phase_{RMS\ MAX}} = 0.9 \cdot 1.07 \frac{V_{DC_{ML}} \cdot n}{\sqrt{2}}. \quad (2.8)$$

The reason for selecting the 5th and 7th harmonic to be eliminated is



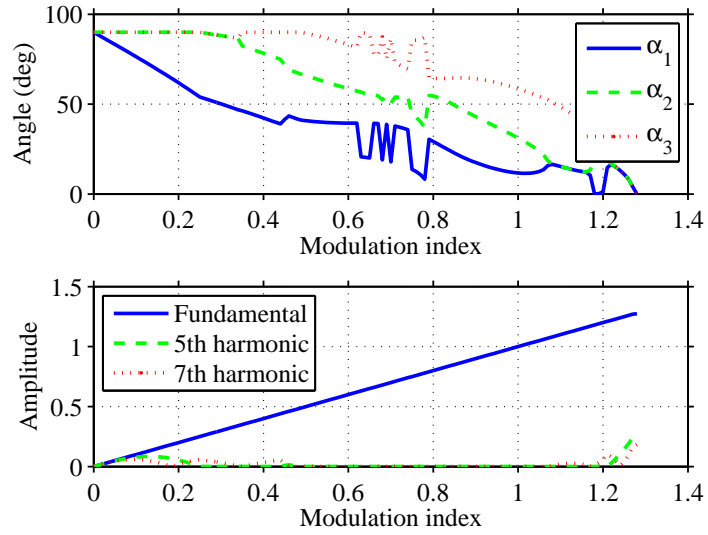


Figure 2.6: Calculated switch angles and harmonics for different modulation indexes.

that these ones has the lowest impedances of the harmonics and are thus most important to keep small in order to have a sinusoidal current that is as free of harmonics as possible.

In Fig. 2.7 to 2.9 typical battery group currents are illustrated to get an understanding of the battery current behaviour when the MLI is controlled with FSHE.

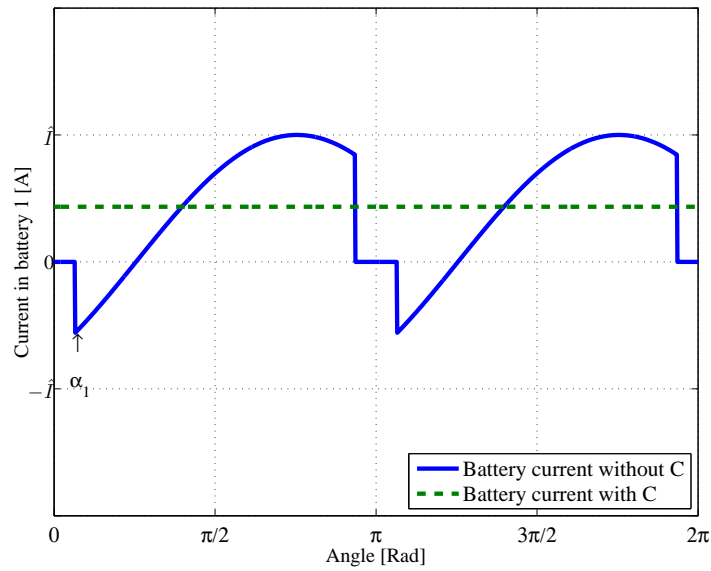


Figure 2.7: Theoretical current waveform through the battery module controlled with  $\alpha_1$ .

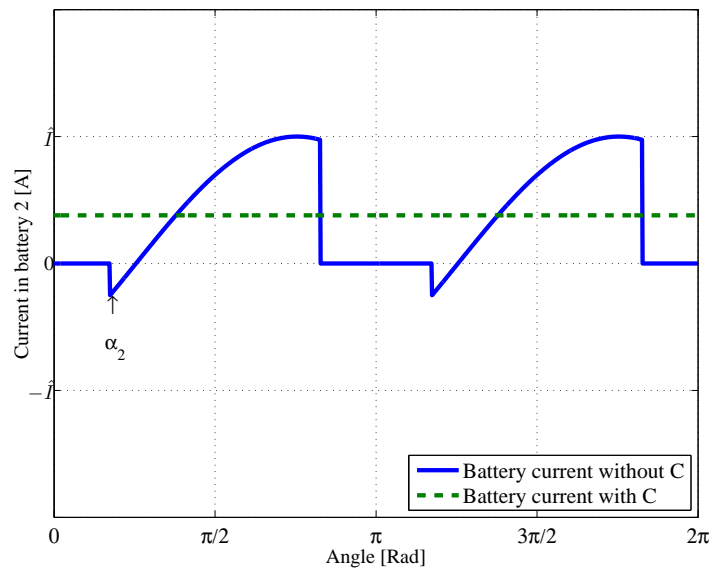


Figure 2.8: Theoretical current waveform through the battery module controlled with  $\alpha_2$ .

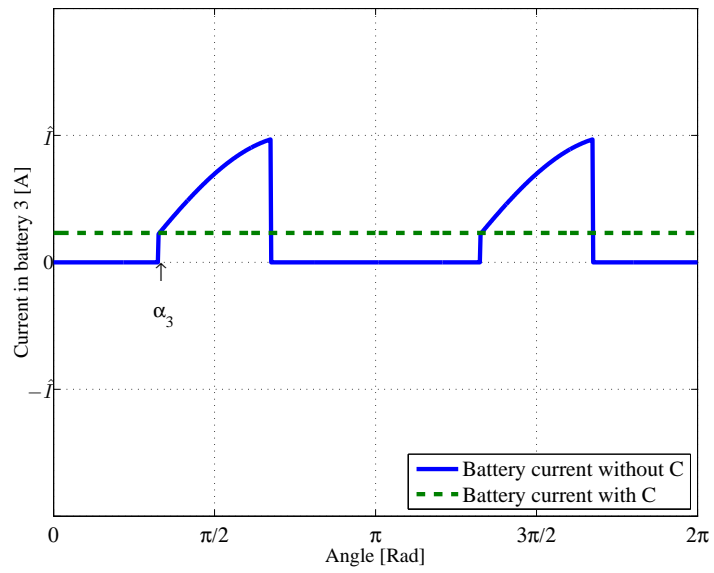


Figure 2.9: Theoretical current waveform through the battery module controlled with  $\alpha_3$ .

### 2.2.2 Balancing strategy for MLI

To ensure that the State of Charge (SOC) is equal among the battery packs, the control system needs to control the use of each H-bridge with respect to the SOC. By programming the controller to use the battery with the highest voltage as the one controlled with  $\alpha_1$  and the one with the lowest voltage with  $\alpha_3$ , the voltage distribution can be kept equal over time.

In the MLI, the balancing between the battery groups comes automatically in the control. A small balancing circuit is needed within each battery group but this only needs to balance the cells within this group. In the TLI, the balancing has to be done within the whole battery pack where a much larger difference in SOC needs to be balanced.

Here a great advantage is that if the cells slowly degrade in a different pace, they can still be utilised in their own best individual performance within each battery group. A TLI on the other hand, must always be operated at the performance level of the most degraded cell.

## 2.3 Electric machine and torque control

Many different electric machine topologies suitable for EVs exist. The switched reluctance machine, SRM, is discussed in [31] where it is stated that it can be a good choice for electrified vehicles, especially for high speeds. However, worries exist that the SRM creates audible noise, so it might not be the best choice for EVs. The Tesla Roadster uses an asynchronous machine, AM [32]. Both the SRM and the AM are very interesting due to high and uncertain magnetic prices. Another magnet-free candidate is the synchronous reluctance machine [33]. The most commonly used machine is anyway the permanent magnet synchronous machine, PMSM. Since it is the most common choice it will be the one analyzed in this thesis. Electric machines used in EVs has to be able to produce enough torque at a large speed range to give a good enough performance to the vehicle. In order to keep the machine size down it is typically used 2-3 times above its continuous operating rating for 5-20 seconds, see [34], [35] and [36].

In order to calculate the losses in the inverter, the waveforms of the currents and voltages to the electric machine need to be known. The electric machine used in this thesis is a permanent magnet synchronous machine, PMSM, with a different inductance in the d and q direction. This gives the possibility to produce a reluctance torque as well as a magnetic torque. The PMSM machine is modeled in steady state with amplitude invariant trans-

formations with the following equations when neglecting the magnetic losses,

$$u_{sd} = R_s i_{sd} - \omega_{el} L_q i_{sq} \quad (2.9)$$

$$u_{sq} = R_s i_{sq} + \omega_{el} L_d i_{sq} + \omega_{el} \psi_m \quad (2.10)$$

$$T_e = \frac{3}{2} p [\psi_m i_{sq} + (L_d - L_q) i_{sq} i_{sd}] \quad (2.11)$$

$$U_{phase_{RMS}} = \sqrt{\frac{u_{sd}^2 + u_{sq}^2}{2}} \quad (2.12)$$

$$I_{phase_{RMS}} = \sqrt{\frac{i_{sd}^2 + i_{sq}^2}{2}} \quad (2.13)$$

$$\varphi = \angle \vec{u}_s - \angle \vec{i}_s \quad (2.14)$$

Neglecting the magnetic losses are considered acceptable since the efficiency of the electric machine will not be dependant on whether the machine is operated with the TLI or the MLI. It will however affect the operating points for the inverters but only to a minor extent and since it affects the analysis of both inverters in the same way, it is also considered to be acceptable.

The machine is controlled with MTPA (Maximum Torque Per Ampere) control and with a phase voltage limitation and a current limitation. When the voltage limit is reached, the machine is controlled with field weakening until the maximum current is reached according to the procedure described in [35]. At the highest speeds the machine might not be able to operate at maximum current depending on the machine parameters, and must then instead be operated along the maximum torque per voltage line (MTPV) [37].

The chosen current vector when using MTPA is presented in Fig. 2.10. It can be seen that the MTPA line is followed for low speeds (up until almost 3000 *rpm*), but at higher speeds, the field weakening region has to be entered. The higher the speed, the earlier the field weakening region has to be entered and at 12000 *rpm* the machine needs to be operated with field weakening even at zero current (zero torque) due to the high back EMF that is present at these high speeds.

## 2.4 Charger

In [24], different topologies for on board chargers are discussed. An advantage with an on-board charger is that the already existing propulsion inverter can be used as a charger. Some topologies even use the inductances in the electric machine as filter components during charging operation. The requirements for a charger for an electric vehicle are widely discussed for instance in [38].

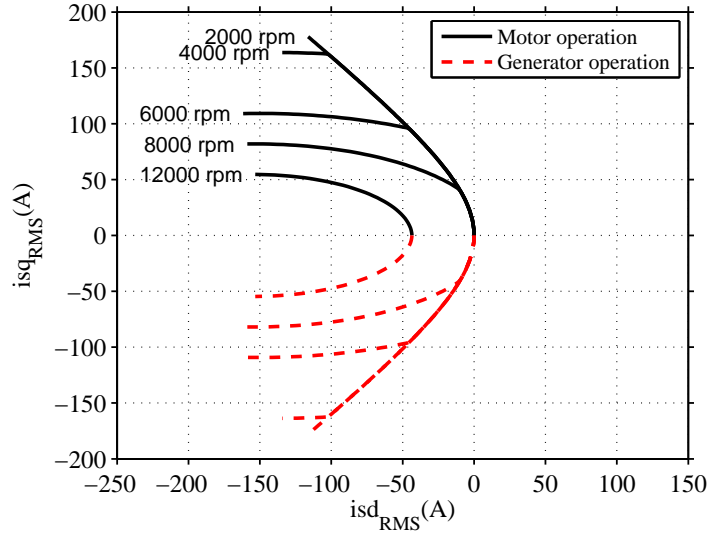


Figure 2.10: Resulting current vector when using MTPA.

It is stated that power factor control is needed, as well as the importance to make sure that the SOC distribution in the battery is constant during charging. In the same way as for the TLI, an advantage with the MLI is that it can be controlled to have a power factor close to unity when rectifying AC to DC during charging operation [39]. In [40] the infrastructure perspective of the charging of EVs are discussed, where a need for bidirectional chargers are stated. This functionality comes from the need of the power system. First, the vehicles can act as energy storages, and then secondly, emergency power can be fed from the vehicles out to the grid if large production units shut down. Both the MLI and the TLI systems have this feature. It is shown that the charger can be built up by already existing components in the EVs with good results, see [41], [42] and [43]. Therefore, using the MLI and the TLI as a charger, as is addressed in this thesis, seems thus to be a beneficial choice from many perspectives.

To be able to have control over the current during charging, the voltage the inverter can produce needs to be higher than the grid voltage. In this thesis, the voltage the inverter can produce is designed to match the selected, rather standard, electric machine and is lower than the grid voltage, hence a transformer is needed for both the TLI and the MLI system. Worth noticing is that this could be redesigned in the future, without any bigger drawback, making it possible to eliminate the transformer. The transformer used in this work is modeled as an ideal transformer without losses, see Fig. 2.11. The

losses in the transformer are neglected since it is assumed that the current waveforms for both the MLI as well as the TLI are almost the same and therefore the transformer losses will be approximately the same for both systems.

For the three phase charging, the transformer is assumed to supply the maximum voltage the inverter can produce, with a margin of 10 %.

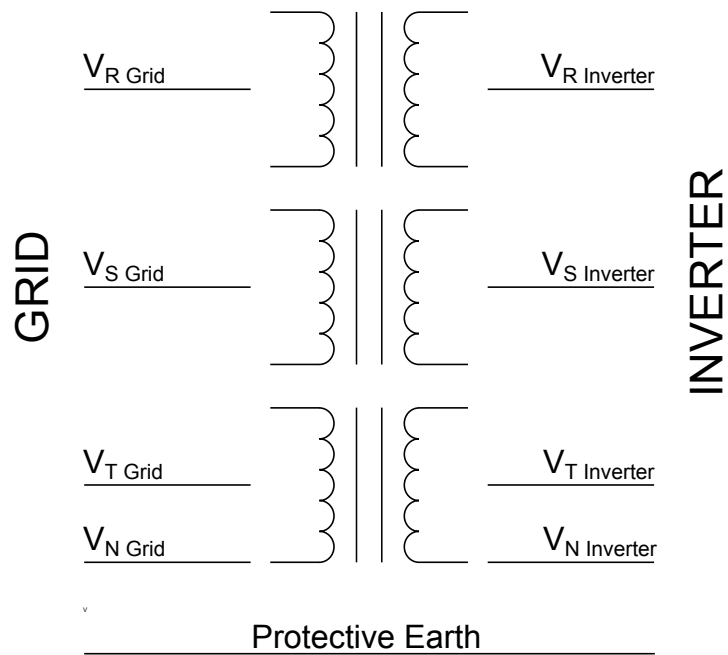


Figure 2.11: Charging transformer.





## Chapter 3

# Inverter loss modeling

In order to evaluate the benefits of using a multilevel inverter (MLI) in electrified vehicles, it is compared to a reference classical two-level inverter (TLI) system in terms of efficiency. To calculate the losses for different operating points, both models of the inverter components as well as the inverter topologies and control strategies are needed.

### 3.1 Power electronic components

To be able to calculate the losses in different inverter topologies, information about the components are needed. In the TLI, IGBTs are used due to their high voltage blocking ability, see Fig. 3.1b, together with diodes, see Fig. 3.1c.

In the MLI, MOSFETs will be used due to the lower blocking voltage requirement for the MLI H-bridge modules, see Fig. 3.1a. This is an important advantage since MOSFETs usually have much lower losses mainly due to that they have a purely resistive voltage drop. Moreover, a benefit of a MOSFET is that it has a built in body diode that sometimes is sufficient as a freewheeling diode. In this thesis, this is the case, so no external diodes will be used in this analysis. In addition, the MOSFETs can conduct in the reverse direction with lower conduction losses than the conduction losses of a good external diode or its internal body diode.

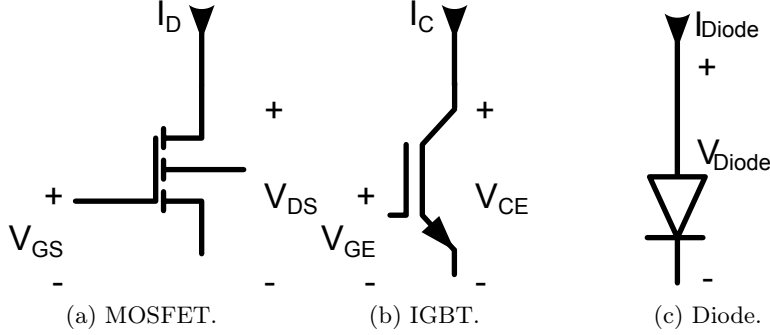


Figure 3.1: Schematic illustrations of different power electronic components.

### 3.1.1 MOSFET losses

The losses of a MOSFET used in a bridge configuration is described in [44]. By supplying a voltage between the gate and the source, the MOSFET transistor turns on. When it has been fully turned on (after some 10-100 ns) it behaves purely resistive. The voltage drop of a turned on MOSFET transistor can therefore be approximated with a linear line as

$$V_{DS}(I_D) = R_{onMOSFET} I_D \quad (3.1)$$

where  $R_{onMOSFET}$  is the resistance in the MOSFET when turned on,  $I_D$  is the current through the MOSFET and  $V_{DS}$  is the voltage over the MOSFET.

When the gate voltage is set to zero, the MOSFET is turned off and the MOSFET then blocks the current very well. Due to the physics of the MOSFET technology there is always an antiparallel diode (body diode) present which will start to conduct when the MOSFET has a negative voltage applied over it. When a negative current flows through the component, the current will go through the "parasitic/inherent body diode" if no gate voltage is supplied. By turning on the MOSFET, a negative current can flow in the MOSFET channel which acts purely resistive. This is an advantage compared to using the a diode of PN-type since it has a constant voltage drop term which would give higher losses.

The switching losses for a MOSFET are due to the rise and fall time of both the current through and the voltage over the component. This loss can (again a bit idealized) be described as seen in Fig. 3.2. The energy loss at turn on is then calculated by

$$E_{on}(V_{DS}, I_D) = \int_0^{T_{on}} I_D(t) V_{DS}(t) dt \approx \frac{V_{DS} I_D T_{on}}{2} \quad (3.2)$$

where  $T_{on}$  is the time to fully turn on the MOSFET.

The energy loss at turn off will in the same way be equal to

$$E_{off}(V_{DS}, I_D) = \int_0^{T_{off}} I_D(t) V_{DS}(t) dt \approx \frac{V_{DS} I_D T_{off}}{2} \quad (3.3)$$

where  $T_{off}$  is the time to fully turn off the MOSFET.

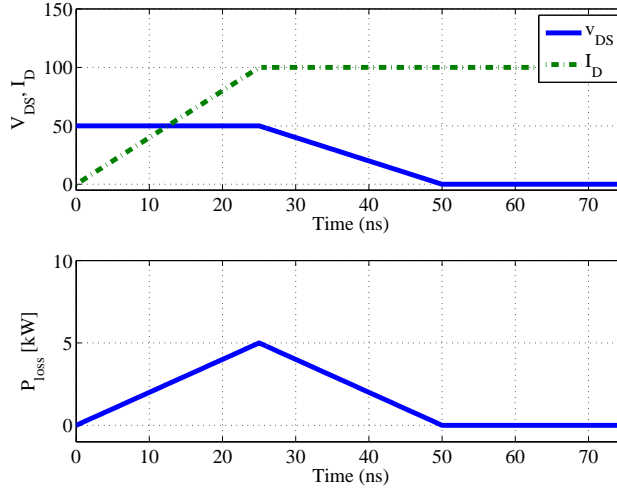


Figure 3.2: Simplified illustration of the turn on losses for MOSFET, switching times approximated for a 100 V MOSFET.

Although the switching waveforms in a MOSFET are simpler to describe than those of the IGBT, they are still very hard to describe, not only due to the mathematical description, but also since circuit and component parasitics strongly influence the behaviour. In this work, this is no problem since the switching frequency is very low, so switching losses give a marginal contribution to the total losses.

### 3.1.2 IGBT losses

The losses in an IGBT are described in [45] when used in a bridge configuration. It is often assumed that the voltage drop of the IGBT is approximated with two straight lines when it is operated in on-state. The two lines are expressed as

$$\begin{aligned} V_{CE}(I_C) &= V_{t_{IGBT}} + R_{on_{IGBT}} I_C & I_C > 0 \\ I_C &= 0 & V_{CE} < V_{t_{IGBT}} \end{aligned} \quad (3.4)$$

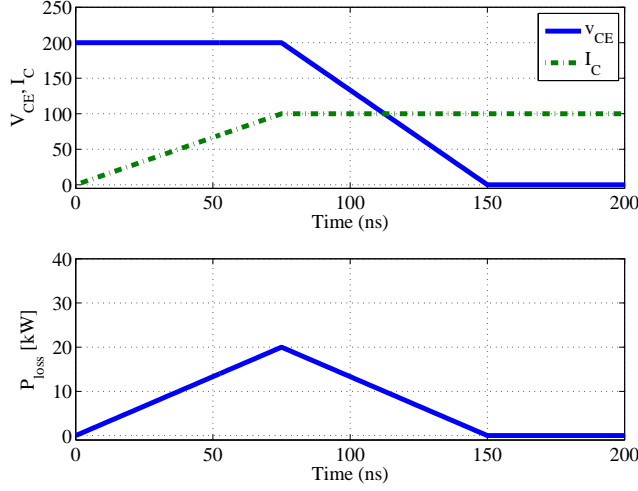


Figure 3.3: Simplified illustration of the turn on loss for an IGBT, switching times approximated for a 600 V IGBT.

where  $R_{on\_IGBT}$  is the resistance when fully turned on,  $V_{l\_IGBT}$  is the constant voltage drop in the IGBT,  $I_C$  is the current through the IGBT and  $V_{CE}$  is the voltage over the IGBT.

When turned off, the IGBT current becomes

$$I_C = 0. \quad (3.5)$$

The switching losses for an IGBT occur when switching from the on state to the off state and vice versa. During the time the IGBT is switching, the occurrence of both voltage and current is present in and over the device which is causing a much higher power loss compared to when the IGBT is in the on state. However, the time when this power loss occurs is very short but since it occurs around 10 000 times every second, it greatly contributes to the inverter losses. This phenomena can (a bit idealized) for a turn on of the IGBT be seen in Fig. 3.3.

The energy loss at turn on is then for this simplified case calculated as

$$E_{on}(V_{CE}, I_C) = \int_0^{T_{on}} I_C(t) V_{CE}(t) dt \approx \frac{V_{CE} I_C T_{on}}{2} \quad (3.6)$$

where  $T_{on}$  is the time to fully turn on the IGBT.

The energy loss at turn off can in the same way be roughly approximated

as

$$E_{off}(V_{CE}, I_C) = \int_0^{T_{off}} I_C(t) V_{CE}(t) dt \approx \frac{V_{CE} I_C T_{off}}{2} \quad (3.7)$$

where  $T_{off}$  is the time to fully turn off the IGBT.

However, in reality the switching losses can not be accurately predicted using algebraic expressions, not even sufficiently using even more complexity. Therefore, if more accurate results are needed, tables from the data sheets are commonly used. In the data sheet, the switching loss is usually plotted as a function of current at a certain blocking voltage. When linearising this loss it can be written as

$$E_{on}(V_{CE}, I_C) = K_{on} V_{CE} I_C \quad (3.8)$$

and

$$E_{off}(V_{CE}, I_C) = K_{off} V_{CE} I_C \quad (3.9)$$

where  $K_{on}$  and  $K_{off}$  are the parameters that describe the linearisation of the data sheet.

If (3.6) and (3.8) are compared and (3.7) and (3.9) are compared, it can be noticed that the parameters  $T_{on}$  and  $T_{off}$  can be calculated from the data sheets according to

$$T_{on} = 2K_{on} \quad (3.10)$$

and

$$T_{off} = 2K_{off}. \quad (3.11)$$

In this work the dc-link voltage is always constant, if the dc-link voltage varies, it is a good idea to modify (3.6) and (3.7) with a non-linear voltage term, since the switching losses rise more than linearly as a function of dc-link voltage level.

### 3.1.3 Diode losses

The losses of a diode used in a bridge configuration is discussed in both [45] and in [44]. The voltage drop of the diode is approximated with two straight lines as

$$\begin{aligned} V_{Diode}(I_{Diode}) &= V_{t_{Diode}} + R_{Diode} I_{Diode} & I_{Diode} > 0 \\ I_{Diode} &= 0 & V_{Diode} < V_{t_{Diode}} \end{aligned} \quad (3.12)$$

where  $R_{Diode}$  is the resistance in the diode,  $V_{t_{Diode}}$  is the constant voltage drop in the diode (typically around 1 V),  $I_{Diode}$  is the current through the

diode and  $V_{Diode}$  is the voltage over the diode between the anode and the cathode.

The switching loss of a diode is assumed to be zero at turn on since it is very low [45], but at turn off the diode has to deplete the charges that are stored in the junction from when it was forward biased. This will create a current in the reverse direction for a short period of time and the energy that is released becomes a loss in both the diode and the opposing switch when connected in a leg configuration. The charge that has to be depleted is current dependent and is for simplicity assumed to be proportional to the current that flew in the diode at the instant right before turn off. The total energy loss can according to [45] be written as

$$E_{RR} = \frac{Q_{rr}V_{drr}}{4} = \frac{Q_{rr}(-V_{Diode})}{4} \quad (3.13)$$

where  $Q_{rr}$  is the charge stored in the diode at the time of the reverse recovery.

If the charge that is stored in the diode can be considered to be proportional to the current, the reverse recovery energy loss can be rewritten as

$$E_{RR} = K_{rr}(-V_{Diode})I_{Diode} \quad (3.14)$$

where  $K_{rr}$  is the loss factor. The loss factor  $K_{rr}$  is taken from the data sheet where the reverse recovery loss is often specified at a certain blocking voltage and current. Sometimes, they are also specified for a certain current derivative.

Again, in reality,  $E_{RR}$  is a complicated parameter to determine and data sheets values with non-linear relations are typically used. However, for the loss calculations made in this thesis, (3.14) is used.

### 3.1.4 Miscellaneous power electronic components

Other components in the inverter also affect the losses in the power train. Here, they are assumed ideal but for example a bad PCB design can have an influence on the losses. To switch the transistors, a driver circuit is needed. In the following work the driver circuit for the transistors is assumed to be lossless. Also, the losses in the dc-link capacitors are ignored, except for Chapter 7.

## 3.2 Two level inverter (TLI)

To be able to calculate the losses in the TLI, information about the operating points used and the control strategy used is needed. The TLI will in this

analysis be controlled with THI-PWM. The reference output voltage for the first phase is described as

$$V_{out}(t) = \hat{U}[\sin(\omega t + \varphi) + a \sin(3\omega t + 3\varphi)] \quad (3.15)$$

and the current as

$$I_{out}(t) = \hat{I} \sin(\omega t) \quad (3.16)$$

where  $\hat{U}$  is the amplitude of the phase voltage,  $\omega$  is the electric frequency,  $\varphi$  is the phase difference between voltage and current and  $\hat{I}$  is the amplitude of the phase current. The amplitude of the third harmonic component  $a$  should be selected to 0.19 for maximum utilization of the DC-voltage, [46]. Although a slightly higher modulation can be reached by using more harmonic components on the reference wave, (3.15) is the wave-shape used for the loss determination in this thesis.

### 3.2.1 Conduction losses

The losses are calculated for one phase of the inverter and are then scaled to be valid for three phases. During the time when the current is positive, the current will go through  $IGBT_{1H}$  and  $Diode_{1L}$ , see Fig. 2.1. The losses in the other pair,  $IGBT_{1L}$  and  $Diode_{1H}$ , will be equal to the loss in the first pair when the current is negative. If the frequency of the sine wave is assumed to be much smaller than the switching frequency, the current and the reference voltage can be assumed to be constant during one switching period. The average conduction loss for one switching event in  $IGBT_{1H}$  and  $Diode_{1L}$  can then be expressed as

$$P_{cond_{IGBT_{1H}}}(I_{out}, D) = \frac{1}{T_{sw}} \int_0^{T_{sw}} V_{DS}(I_D) I_D dt = DI_{out} V_{t_{IGBT}} + DR_{on_{IGBT}} I_{out}^2 \quad (3.17)$$

and

$$P_{cond_{Diode_{1L}}}(I_{out}, D) = \frac{1}{T_{sw}} \int_0^{T_{sw}} V_{Diode}(I_{Diode}) I_{Diode} dt = (1 - D) I_{out} V_{t_{Diode}} + (1 - D) R_{on_{Diode}} I_{out}^2 \quad (3.18)$$

using (3.4) and (3.12).

To calculate the average conduction losses for one phase, one can choose to study the positive part of the current, knowing that the current only goes through  $IGBT_{1H}$  and  $Diode_{1L}$ . Knowing that the same losses will be generated in  $IGBT_{1L}$  and  $Diode_{1H}$  during the negative part of the current,

the average losses of one leg can then, by combining (3.17) and (2.4), be written as

$$\begin{aligned}
P_{conductionIGBTs_1} &= \\
& \frac{\int_0^{T_f} P_{condIGBT_{1H}}(t) + P_{condIGBT_{1L}}(t) dt}{T_f} = \\
& \frac{\int_0^{T_f/2} P_{condIGBT_{1H}}(t) dt}{T_f/2} = \\
\hat{I}V_{tIGBT} \left( \frac{1}{\pi} + \frac{\hat{U} \cos \varphi}{2V_{DC_{TL}}} \right) + R_{onIGBT} \hat{I}^2 \left( \frac{1}{4} + \frac{4\hat{U} \cos \varphi}{3\pi V_{DC_{TL}}} - \frac{2a \cdot \cos(3\varphi)}{15\pi} \right). \quad (3.19)
\end{aligned}$$

The losses in the diode can be calculated in the same way using (3.18) and (2.4) which gives

$$\begin{aligned}
P_{conductionDiodes_1} &= \\
& \frac{\int_0^{T_f} P_{condDiode_{1H}}(t) + P_{condDiode_{1L}}(t) dt}{T_f} = \\
& \frac{\int_0^{T_f/2} P_{condDiode_{1L}}(t) dt}{T_f/2} = \\
\hat{I}V_{tDiode} \left( \frac{1}{\pi} - \frac{\hat{U} \cos \varphi}{2V_{DC_{TL}}} \right) + R_{onDiode} \hat{I}^2 \left( \frac{1}{4} - \frac{4\hat{U} \cos \varphi}{3\pi V_{DC_{TL}}} + \frac{2a \cdot \cos(3\varphi)}{15\pi} \right). \quad (3.20)
\end{aligned}$$

### 3.2.2 Switching losses

The switching losses for the IGBTs can be calculated with the assumption that the fundamental frequency is much lower than the switching frequency. If the leg would operate in DC-mode, the average switching loss for  $IGBT_{1H}$  can be described as

$$\begin{aligned}
P_{switchIGBT_{1H}}(I_{out}) &= [E_{on}(I_{out}) + E_{off}(I_{out})]f_{sw} = \\
& \frac{(T_{on} + T_{off})V_{DC_{TL}}I_{out}f_{sw}}{2}. \quad (3.21)
\end{aligned}$$

For the diodes, the turn on losses are neglected but the reverse recovery can have a significant contribution to the losses. It can be written as

$$P_{rrDiode_{1L}}(I_{out}) = E_{rr}(I_{out})f_{sw} = K_{rr}V_{DC_{TL}}I_{out}f_{sw} \quad (3.22)$$

using (3.14).



Operating the converter in AC mode, the switch losses for the IGBTs in one leg can then be calculated as

$$P_{switch_{IGBTs_1}} = \frac{\int_0^{T_f/2} 2 \frac{(T_{on} + T_{off}) V_{DC_{TL}} I_{out}(t) f_{sw}}{2} dt}{T_f} = \frac{2(T_{on} + T_{off}) V_{DC_{TL}} f_{sw} \hat{I}_{out}}{\pi} \quad (3.23)$$

and the diode losses as

$$P_{rr_{Diodes_1}} = \frac{\int_0^{T_f/2} 2 K_{rr} V_{DC_{TL}} I_{out}(t) f_{sw} dt}{T_f} = \frac{2 K_{rr} V_{DC_{TL}} \hat{I}_{out} f_{sw}}{\pi}. \quad (3.24)$$

### 3.2.3 Total losses

The total losses for a TLI running in AC-mode will therefore be the sum of the losses in one leg multiplied with the number of legs which gives

$$P_{Loss_{TLI}} = 3(P_{conduction_{IGBTs_1}} + P_{conduction_{Diodes_1}} + P_{switch_{IGBTs_1}} + P_{rr_{Diodes_1}}) \quad (3.25)$$

using (3.19), (3.20), (3.23) and (3.24).

## 3.3 Multilevel inverter (MLI)

To be able to calculate the losses in the MLI, information about the operating point is needed as well as the control strategy. In this analysis, it will be controlled with Fundamental Selective Harmonic Elimination, FSHE. The MLI is assumed to be operating at an output voltage expressed as

$$V_{out}(t) = \hat{U}(\sin(\omega t + \varphi)) \quad (3.26)$$

and the current as

$$I_{out}(t) = \hat{I} \sin(\omega t). \quad (3.27)$$

### 3.3.1 Conduction losses

The current will always flow through two transistors for each H-bridge. The voltage drop for one MOSFET can be written according to (3.1). The total voltage drop will therefore be equal to

$$V_{drop} = 2n I_{out}(t) R_{on_{MOSFET}} \quad (3.28)$$

independently of the current direction assuming that the MOSFET is turned on when conducting in the reverse direction.

The conduction power loss for all three phases of the MLI can therefore be calculated as

$$P_{conduction_{MLI}} = 6nI_{out_{RMS}}^2 R_{on_{MOSFET}} = 3n\hat{I}^2 R_{on_{MOSFET}}. \quad (3.29)$$

### 3.3.2 Switching losses

The switching losses can be described as a sum of the energy losses during one cycle. When controlled with FSHE, the switching occurs very seldom, see Fig. 2.5. During the first three switching instances, the inverter switches the H-bridges to create a positive voltage. Depending on the current direction this will result in either a turn on or a turn off loss. The loss for the MOSFET and diode can therefore at the first three switching instances be written as

$$\begin{aligned} E_{on_{\alpha_{1,2,3}}} &= \frac{V_{dc_{ML}} I(\alpha_{1,2,3}) T_{on}}{2} & I(\alpha_{1,2,3}) \geq 0 \\ E_{on_{\alpha_{1,2,3}}} &= 0 & I(\alpha_{1,2,3}) < 0 \end{aligned} \quad (3.30)$$

$$\begin{aligned} E_{off_{\alpha_{1,2,3}}} &= 0 & I(\alpha_{1,2,3}) \geq 0 \\ E_{off_{\alpha_{1,2,3}}} &= \frac{V_{dc_{ML}} I(\alpha_{1,2,3}) T_{off}}{2} & I(\alpha_{1,2,3}) < 0 \end{aligned} \quad (3.31)$$

$$\begin{aligned} E_{rr_{\alpha_{1,2,3}}} &= V_{dc_{ML}} I(\alpha_{1,2,3}) K_{rr} & I(\alpha_{1,2,3}) \geq 0 \\ E_{rr_{\alpha_{1,2,3}}} &= 0 & I(\alpha_{1,2,3}) < 0. \end{aligned} \quad (3.32)$$

For the fourth, fifth and sixth switching instances the inverter switches to create zero volts for the inverters. This gives a loss according to

$$\begin{aligned} E_{on_{\alpha_{4,5,6}}} &= 0 & I(\alpha_{4,5,6}) \geq 0 \\ E_{on_{\alpha_{4,5,6}}} &= \frac{V_{dc_{ML}} I(\alpha_{4,5,6}) T_{on}}{2} & I(\alpha_{4,5,6}) < 0 \end{aligned} \quad (3.33)$$

$$\begin{aligned} E_{off_{\alpha_{4,5,6}}} &= \frac{V_{dc_{ML}} I(\alpha_{4,5,6}) T_{off}}{2} & I(\alpha_{4,5,6}) \geq 0 \\ E_{off_{\alpha_{4,5,6}}} &= 0 & I(\alpha_{4,5,6}) < 0 \end{aligned} \quad (3.34)$$

$$\begin{aligned} E_{rr_{\alpha_{4,5,6}}} &= 0 & I(\alpha_{4,5,6}) \geq 0 \\ E_{rr_{\alpha_{4,5,6}}} &= V_{dc_{ML}} I(\alpha_{4,5,6}) K_{rr} & I(\alpha_{4,5,6}) < 0. \end{aligned} \quad (3.35)$$

During switching occasion 7 to 12 the losses will be equal to the loss during switch 1 to 6. Therefore the losses can be calculated as

$$P_{switch_{MLI}} = 3 \cdot 2 \cdot f_{fund} \sum_{n=1}^6 (E_{on_{\alpha_n}} + E_{off_{\alpha_n}} + E_{rr_{\alpha_n}}). \quad (3.36)$$

### 3.3.3 Total losses

The total losses for the multilevel inverter can be written as

$$P_{Loss_{ML}} = P_{conduction_{MLI}} + P_{switch_{MLI}} \quad (3.37)$$

using (3.29) and (3.36).



## Chapter 4

# Case setup & inverter waveform verification

To make a comparison between the TLI and the MLI, some boundary conditions has to be established. This chapter presents the chosen components necessary to build up the drive system as well as defining appropriate operating conditions for performing energy consequence studies. For the further analysis, a 25 °C temperature is assumed unless otherwise stated.

First, the system used for the main analysis is presented Section 4.1. Then the experimental small scale system is described in Section 4.2 and used in Section 4.3 for a verification of the theory from Chapter 2.

### 4.1 Small PEV reference vehicle

The vehicle analyzed is a small compact PEV with the data given in Table 4.1. It is made small to match the rating of the electric machine so that all operating points for the analysed drive cycles can be achieved. It has an electric driving range of around 50 km, but some analysis is later made with the same vehicle but a four times bigger battery size. In this thesis, the vehicle does not incorporate regenerative braking. However, since all the analysis is done in the same way the differences between various results are considered to be valid.

Table 4.1: Car parameters.

Parameter	Value	Unit
Weight	1100	$kg$
$A \cdot C_d$	0.45	$Nv^{-2}$
Friction coefficient	0.01	$N$
Wheel radius	0.33	$m$
Gearbox ratio	11.5	
Gearbox efficiency	90	$\%$
Top speed	130	$kmh^{-1}$

#### 4.1.1 Electric machine

The electric machine used for the analysis in this thesis is a PMSM machine with parameters according to Table 4.2. The magnetic losses have been ignored.

Table 4.2: Parameters of the electric machine.

Parameter	Value	Unit
$L_d$	150	$\mu H$
$L_q$	300	$\mu H$
$R_s$	20	$m\Omega$
Pole pairs	5	
$\psi_m$	33	$mWb$
Maximum transient phase voltage	106	$V_{RMS}$
Maximum transient phase current	212	$A_{RMS}$
Maximum transient torque	109	$Nm$
Maximum transient power	49	$kW$

Operating the electric machine at different torques and speeds gives the operation points according to Fig. 4.1 to 4.3 using (2.9) to (2.14) when using a DC-voltage of 260 V to account for control margin and battery voltage drop. In the figures, the operation points of the NEDC drive cycle (which will be presented in section 4.1.5) is also given as a reference of where the electric machine is typically used. In Fig. 4.2 it can be seen that the voltage increases with speed up to the field weakening region. When the maximum voltage governed by the battery is reached, the machine can continue to increase its

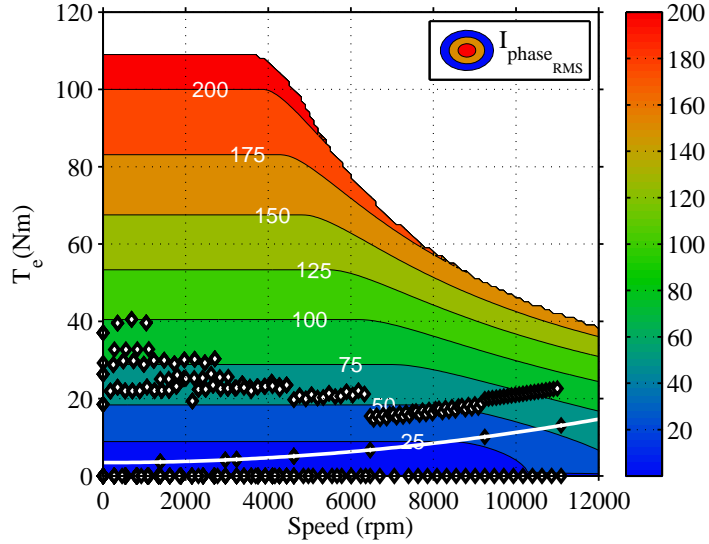


Figure 4.1: Calculated RMS-value of the phase currents for different operating points. The NEDC driving cycle is marked for reference. The white line shows the torque needed to propel the vehicle at constant speed.

speed by demagnetising the machine. This is done by increasing the current in the negative d-direction giving room for increasing the q-direction current. When the current limit is reached, it is however not possible to increase the torque further. This can be seen in Fig. 4.1 where the straight current lines bends down when entering the field weakening region. It is also observable in Fig. 4.3 that the current leads the voltage in the field weakening region due to that we need to use a current to demagnetize the machine. It is very clear that during the NEDC drive cycle, only a fraction of the machine capacity is used.

#### 4.1.2 Test vehicle battery

The analysed and used battery cell is the ANR26650M1A from A123 systems [47]. It has a rated capacity of  $2.3 \text{ Ah}$  and a nominal voltage of  $3.3 \text{ V}$ . According to the data sheet, the cell should have a typical DC-resistance of  $10 \text{ m}\Omega$ . However, Measurements performed in Chapter 6 show that the cells have a DC-resistance of  $15 \text{ m}\Omega$  at  $25 \text{ }^\circ\text{C}$  and therefore this value will be used in the further analysis.

For the MLI system, 9 battery groups consisting of 15 series connected stacks of 10 parallel cells are forming the total energy storage. Each battery

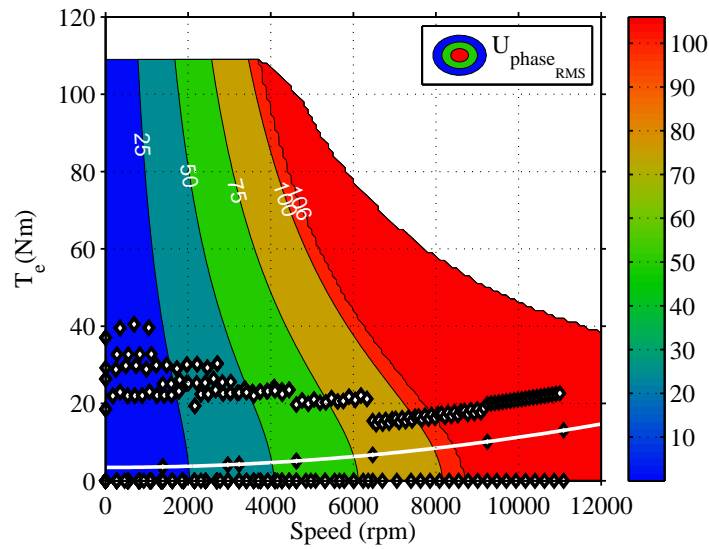


Figure 4.2: Calculated RMS-value of phase voltages for different operating points. Description as in Fig. 4.1.

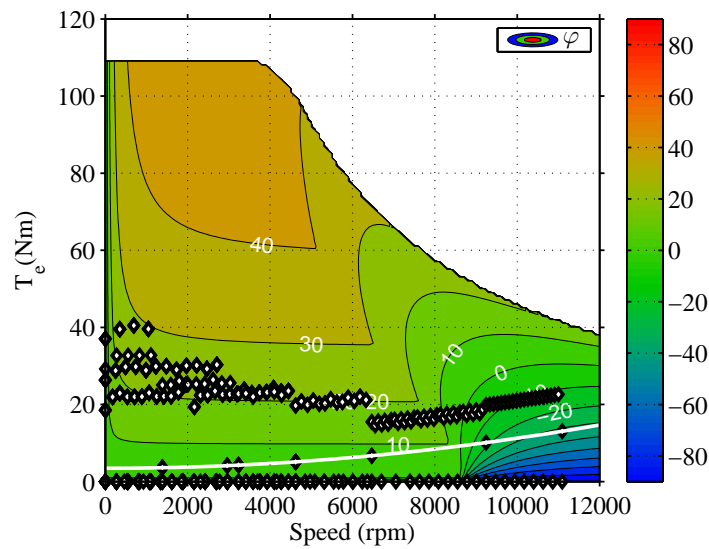


Figure 4.3: Calculated phase difference between voltage and current for different operating points. Description as in Fig. 4.1.



group will have a nominal voltage of  $49.5\text{ V}$ . The nominal energy content of all 9 groups sums up to a total capacity of  $10.25\text{ kWh}$ .

For the TLI system, one big battery pack is formed consisting of 90 series connected stacks of 15 parallel connected cells, building up a total capacity of  $10.25\text{ kWh}$  at a nominal voltage of  $297\text{ V}$ .

### 4.1.3 Filter capacitors for the MLI system

Since the battery currents are far from DC, capacitors can be placed over the inputs of the H-bridges in order to smoothen the battery current. This is illustrated very simplified in Fig. 4.4.

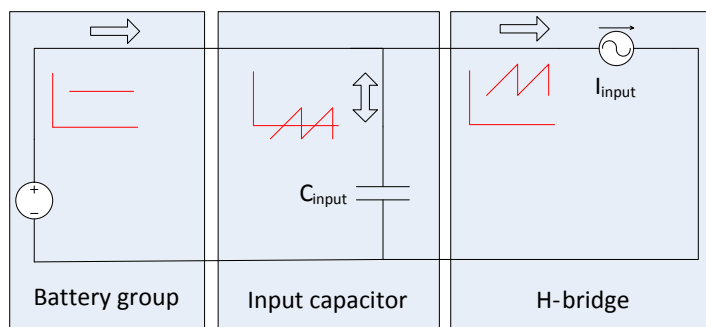


Figure 4.4: Illustration of filter capacitor influence.

In Chapter 5, a simulation case where an infinitely large capacitor placed over the input to the H-bridges will be used. The capacitors are here assumed to filter the battery currents to DC. This is done in order to show the extreme case of the filter capacitor influence but to make the analysis more accurate, a more thorough analysis of the capacitor influence is performed in Chapter 7 with capacitors presented below.

#### Electrolytic capacitor

In Chapter 7, one of the analysed chemistries is the electrolytic capacitor PEH169GD5220Q from RIFA/KEMET [48] with a capacitance of  $22\text{ mF}$ , a voltage capability of  $16\text{ V}$  and an equivalent series resistance (ESR) of  $14\text{ m}\Omega$ . It is built up in various combinations presented in that chapter to verify the amount needed.

## Super capacitor

The second chemistry analysed in Chapter 7 is the super capacitor. It is in that analysis built up by different combinations of the super capacitor RSC2R7107SR from Ioxus [49] with a capacitance of 100  $F$ , a voltage capability of 2.7  $V$  and an ESR of 4.6  $m\Omega$ . In the same way as for the electrolytic capacitor, the capacitor is scaled to various amounts to look at the capacitor influence.

### 4.1.4 Test vehicle power electronic components

The selected IGBT and diode combination for the TLI is chosen to FS800R07A2E3 from Infineon [50] and the MOSFET and diode combination for the MLI is chosen to IPB025N10N3 [51], see Table 4.3 where the parameters are presented per discrete transistor. They are chosen to make the comparison fair since they have about the same relative margin to the breakdown voltage. To make the current rating equal, the MOSFETs will be placed with 5 in parallel.

Table 4.3: Parameters of the power electronic components. Parameters are presented per discrete transistor.

Parameter	FS800R07A2E3	IPB025N10N3	Unit
No in parallel	1	5	$Pcs$
Rated voltage	600	100	$V$
Rated current	800	180	$A$
$V_{ttransistor}$	0.7	0	$V$
$R_{ontransistor}$	2.1	2.0	$m\Omega$
$T_{on}$	N/A	58	$ns$
$T_{off}$	N/A	28	$ns$
$K_{on}$	83	N/A	$nJ V^{-1}A^{-1}$
$K_{off}$	150	N/A	$nJ V^{-1}A^{-1}$
$V_{tDiode}$	0.9	Not in use	$V$
$R_{onDiode}$	1.0	Not in use	$m\Omega$
$K_{rr}$	67	43	$nJ V^{-1}A^{-1}$

### 4.1.5 Drive cycle presentation

When analyzing energy consumption of vehicles in various driving situations, different drive cycles are used in order to perform comparisons. In this thesis, four different drive cycles are used, see Fig. 4.5 and Table 4.4. The drive cycles are used to determine the losses in both the battery and in the inverter, in order to evaluate the performance over a range of operating points.

The first is the New European Driving Cycle, NEDC. The NEDC is designed to represent the way vehicles are used in Europe and was introduced 1990. It is made up from four repetitions of the city drive cycle ECE15, and one high speed drive cycle, EUDC. The average speed of the vehicle is 33 km/h and the maximum speed is 120 km/h. This drive cycle is typically used to classify the fuel consumption in Europe, however, the drive cycle has received much criticism lately since it does not represent the way cars are used. Modern vehicles have much more power than 20 years ago and are driven with steeper accelerations.

The second drive cycle is the EPA Federal Test Procedure, FTP75. This drive cycle is used in the United States to specify the fuel consumption of a vehicle. It has the same average speed as NEDC but the top speed is much lower, only 91 km/h. This drive cycle has also gotten criticism for not being aggressive enough and is therefore complemented with the US06, described more below.

The third drive cycle analyzed is the EPA Highway Fuel Economy Cycle, HWFET. This drive cycle aims at light duty trucks and is included in this thesis to show the behavior of the multilevel inverter for small trucks. The HWFET is a much less dynamic drive cycle than the other.

The last drive cycle is the US06 Supplemental Federal Test Procedure, US06. It is a very aggressive drive cycle compared to the others; the accelerations are harder and the top speed goes up to 129 km/h. It is used as a complement to the FTP75 to show a more realistic way of the usage of the vehicle.

## 4.2 Experimental system

To verify the waveforms created by the MLI an experimental setup is designed. The inverter will be used to verify the wave shapes used in the analytical analysis. The experimental MLI can be seen in Fig. 4.6. In the experimental MLI, the MOSFET IRF1324S-7PPbF from Infineon is used [52]. The on resistance ( $R_{onMOSFET}$ ) of this MOSFET is only maximum 1 m $\Omega$ .

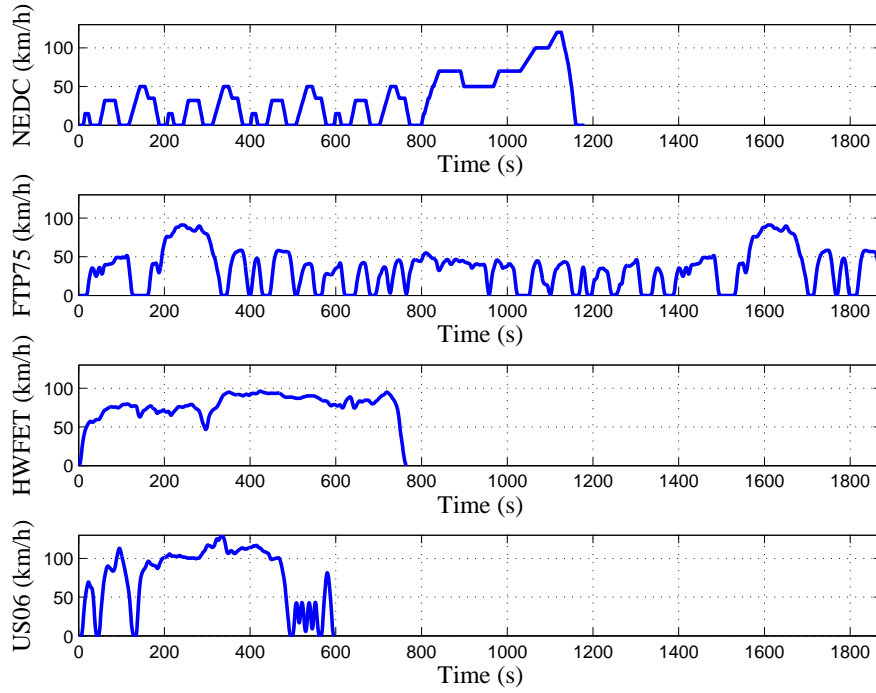


Figure 4.5: Speed profiles of the drive cycles.

Table 4.4: Drive cycle parameters

Drive cycle	Speed avg [km/h]	Speed max [km/h]	Time [s]	Distance [km]	Energy regen [Wh/km]	Energy no regen [Wh/km]
NEDC	33	120	1180	10.9	54	82
FTP75	34	91	1874	17.8	44	80
HWFET	78	96	766	16.5	68	76
US06	78	129	596	12.9	83	117

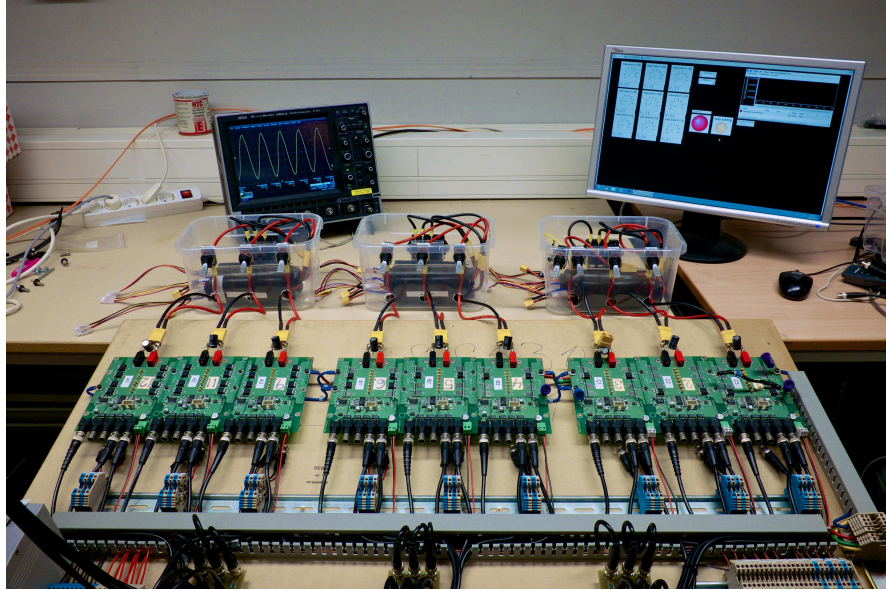


Figure 4.6: Laboratory setup of the 7-level multilevel inverter. The 3 phases consist of 3 H-bridges each. The battery inputs are shown in the upper part of the picture, the outputs are on the right side of the groups and the common Y-connection point is shown on the left side of each phase leg.

To each input the same battery cell as for the test vehicle presented in Section 4.1.2 is used, but here only 4 cells are connected in series and 1 in parallel.

As an inverter load, both a small asynchronous machine as well as a controllable RL-load is used.

## 4.3 Experimental base verification

### 4.3.1 Output waveforms and harmonics

Figs. 4.7 to 4.9 show the output voltage from the MLI at  $m_a = 0.5$ ,  $m_a = 1.0$  and  $m_a = 1.2$ . It can be seen that the first harmonic in the line to line voltage is number 11 for  $m_a = 0.5$  and  $m_a = 1.0$ . Accordingly the harmonic elimination strategy is fully successful for the first to cases. When operating at  $m_a = 1.2$  the possibility to eliminate harmonic 5 and 7 is no longer present. The result is clearly visible in the measured curves where a set of low-frequency harmonic now have emerged, as can be noted in Fig. 4.9.

In Fig. 4.10 and 4.11 the 5th and the 7th harmonic are plotted for different  $m_a$ . It shows a good match with the analytical calculations presented in Fig. 2.6.

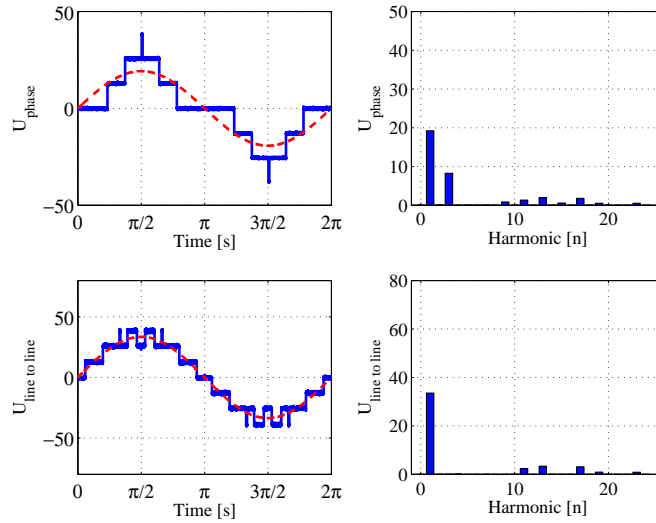


Figure 4.7: Measured voltage output and harmonic content at  $m_a = 0.5$ . Dashed lines show the fundamental components. The load is a resistor with a resistance of  $1\text{ k}\Omega$ .

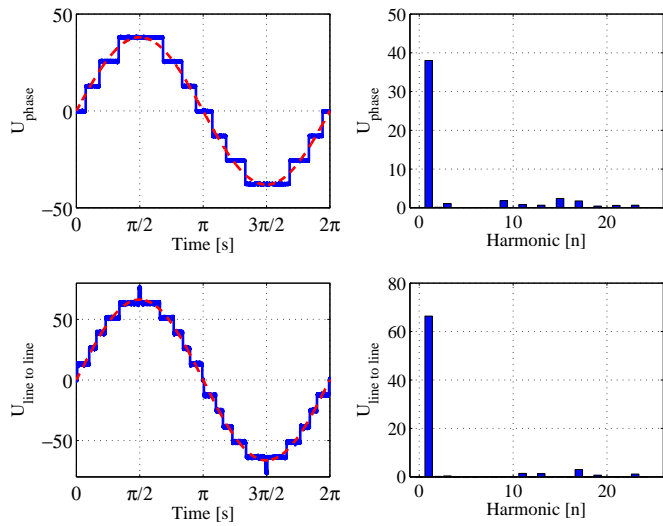


Figure 4.8: Measured voltage output and harmonic content at  $m_a = 1.0$ . Dashed lines show the fundamental components. The load is a resistor with a resistance of  $1\text{ k}\Omega$ .

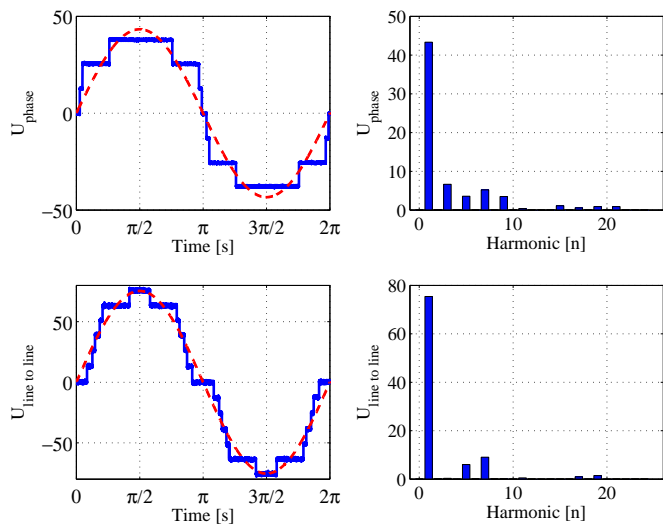


Figure 4.9: Measured voltage output and harmonic content at  $m_a = 1.2$ . Dashed lines show the fundamental components. The load is a resistor with a resistance of  $1\text{ k}\Omega$ .

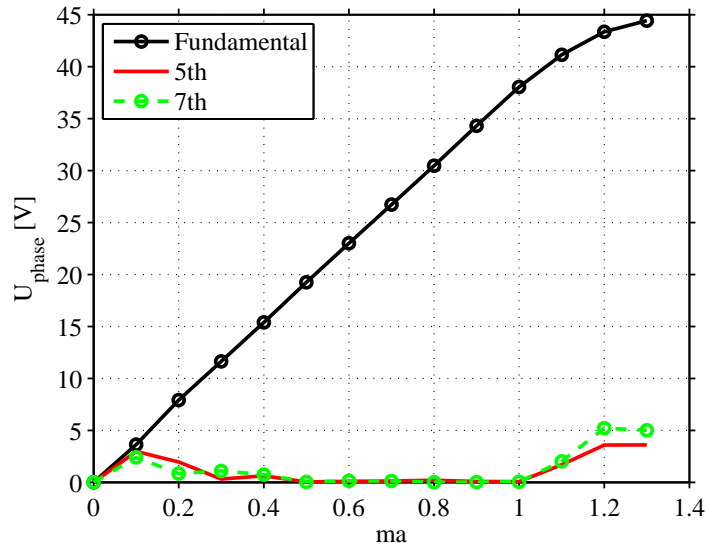


Figure 4.10: Measured fundamental, 5th and 7th harmonic in the phase voltage.

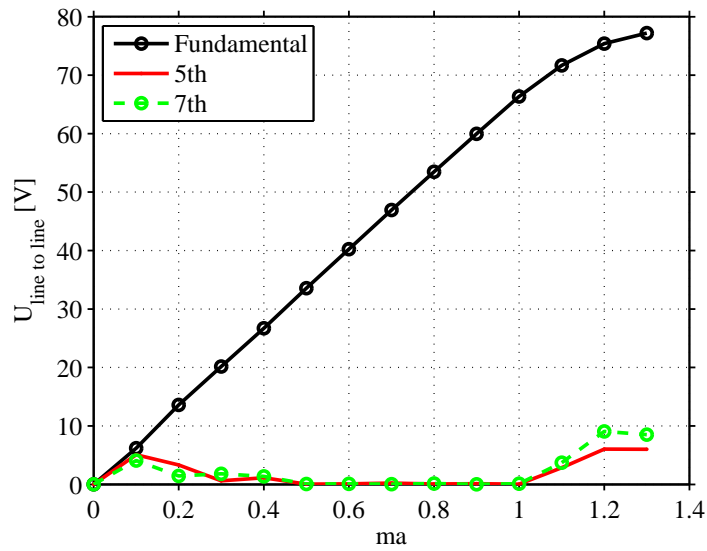


Figure 4.11: Measured fundamental, 5th and 7th harmonic in the line to line voltage.



### 4.3.2 Total Harmonic Distortion

The total harmonic distortion, THD, for the output voltage is both simulated and measured for different magnitudes of the output voltage. The voltage THD is calculated with help of the RMS value and its definition range is therefore very high. The simulations and the measurements can be seen in Fig. 4.12 and show a good match.

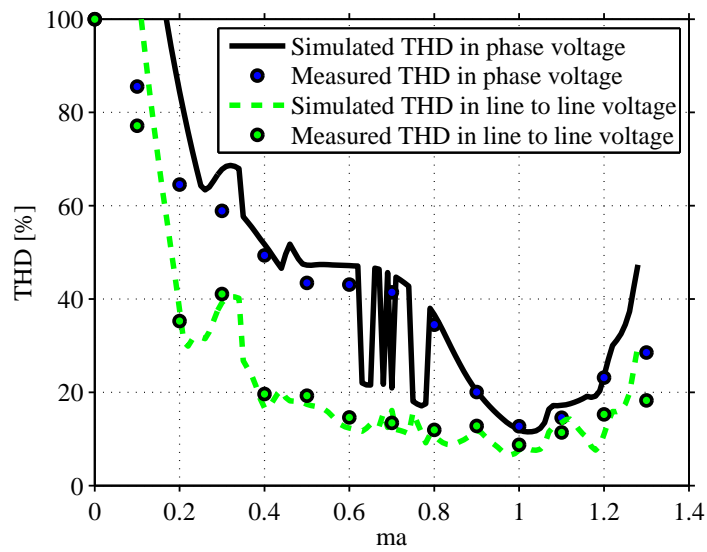


Figure 4.12: Simulated and measured voltage THD for the MLI.

It can be seen that the THD is as lowest at  $m_a = 1$ , then the THD is down to under 10 % for the line to line voltage.

### 4.3.3 Balancing using the experimental setup

The possibility to balance the battery cells is evaluated with the MLI experimental setup. For this test, the energy sources is chosen to small super capacitors with a capacitance of  $10 F$  each in order to quickly see the balancing behaviour. The three capacitors in one leg are charged to  $1.6 V$ ,  $1.8 V$  and  $2.3 V$ . The inverter is then operated at  $m_a = 1$  to a resistive load to verify that the inverter will balance the cells during sine wave operation. It is operated at  $m_a = 1$  since this case uses all cells most equal amount and is therefor the most demanding case. The control strategy is to use the inverter with the highest voltage as the inverter controlled with  $\alpha_1$ , and the inverter with the lowest voltage as the one controlled with  $\alpha_3$ .

In Fig. 4.13 the super capacitor voltages are plotted over time, it can be seen that the capacitors will have about the same voltage after around  $90 s$ . It can also be noted that the voltages never get exactly the same. The reason for this is that the resolution of the A/D-converters are very poor. For this specific test, when the control system measures that the cells are equal (balanced), it always uses the first H-bridge (green curve) which is the one that is controlled with  $\alpha_1$  (since this H-bridge has to output power the longest time), the second (red curve) with  $\alpha_2$  and the third (blue curve) with  $\alpha_3$ .

This unfortunately causes the cells to never be totally balanced in this setup, they will stay unbalanced to a level matching the resolution of the A/D-converter. Anyway, up until the A/D-conversion limit, the balancing works very well.

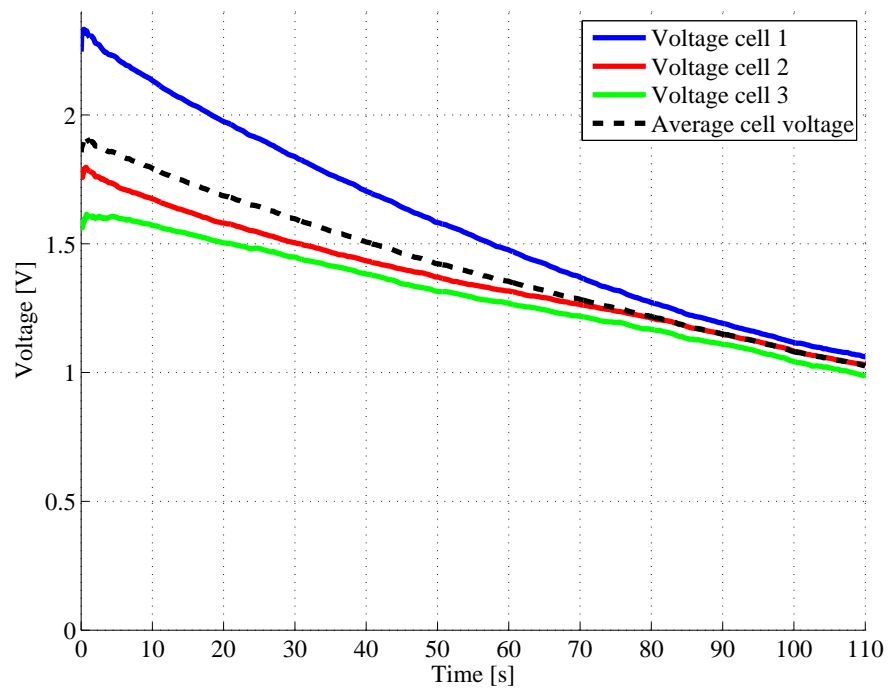


Figure 4.13: Measured balancing performance. The three cell voltages in one leg converges to the same voltage level over time when operating the MLI as a propulsion inverter or a charger.

### 4.3.4 Battery current verification with the experimental setup

In Fig. 4.14 the inverter is operated at  $m_a = 1$  and  $f_{fundamental} = 50 \text{ Hz}$ . The load consists of an RL load with  $R = 11 \Omega$  and  $L = 36 \text{ mH}$ . The current in the battery groups can be seen in Fig. 4.15 to 4.17. These waveforms can be compared with the theoretical ones presented in Fig. 2.7 to 2.9. By performing this comparison, it can be noted that the agreement is very good.

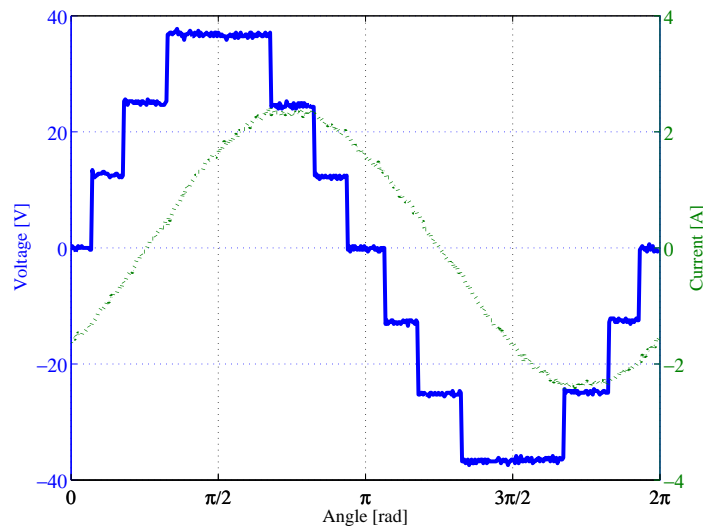


Figure 4.14: Measured output phase voltage and current. Solid blue curve shows the voltage and the green dashed curve shows the current.

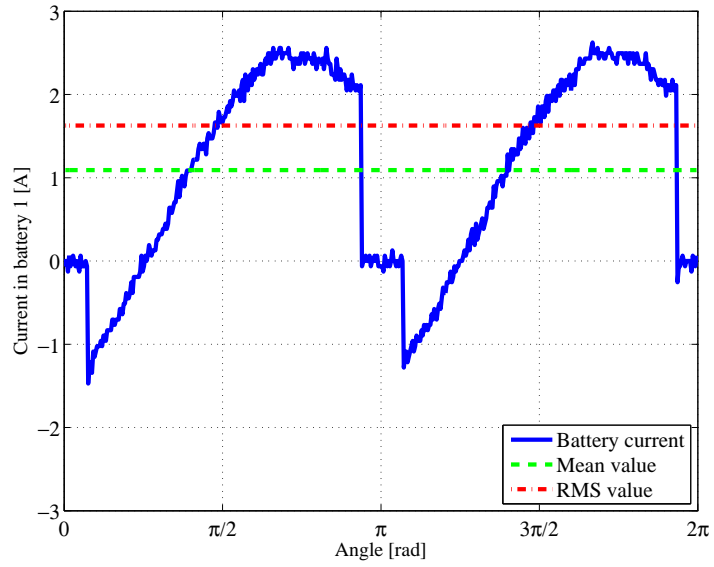


Figure 4.15: Measured current in battery group 1.

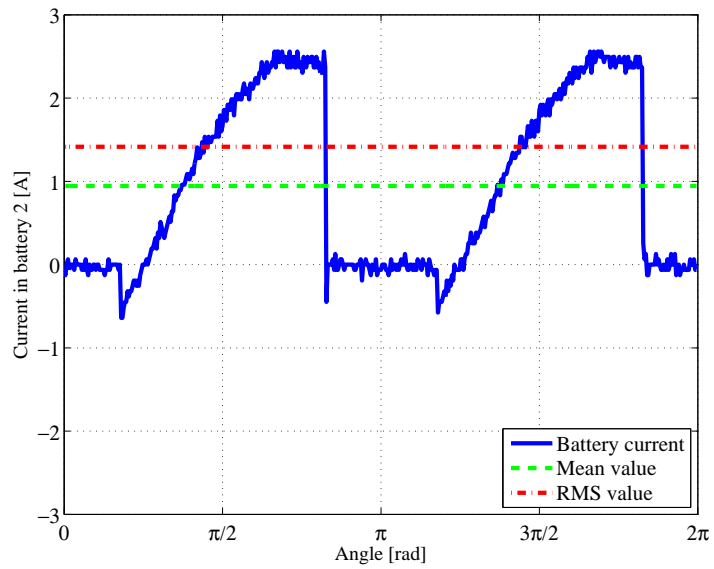


Figure 4.16: Measured current in battery group 2.

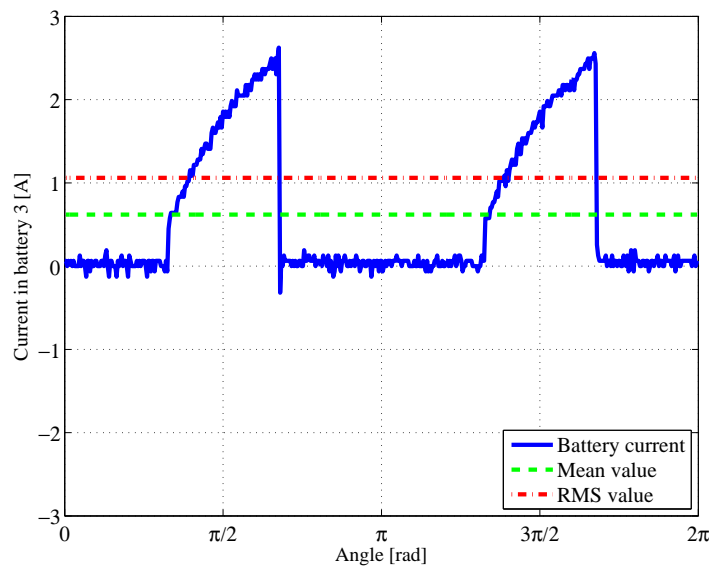


Figure 4.17: Measured current in battery group 3.

## Chapter 5

# Small PEV power train loss evaluation

### 5.1 Efficiency calculations

When an inverter is used to supply the electric machine in an electric vehicle, the losses of the inverter are dependant on the operating points of the car. Based on the operating points given in Fig. 4.1 to 4.3, the losses in the inverter and in the battery are calculated according to Chapter 3 for the respective systems.

The analysis will mainly be done using the 50 km PEV while at end, results for a 200 km EV will also be presented.

#### 5.1.1 Inverter

The losses in the two different inverters are calculated assuming that the current to the electrical machine is equal for the two cases and that the harmonic levels are low and can accordingly be ignored in the loss calculations for the inverters.

##### Two level inverter

The power loss for the TLI using IGBTs is calculated for different torques and speeds and is shown in Fig. 5.1 for a switching frequency of 10  $kHz$  using (3.25). It can be seen that the losses increase quite proportionally to the current and so does also the torque. The losses are not speed dependent since the magnetic losses in the the machine are neglected. However, when

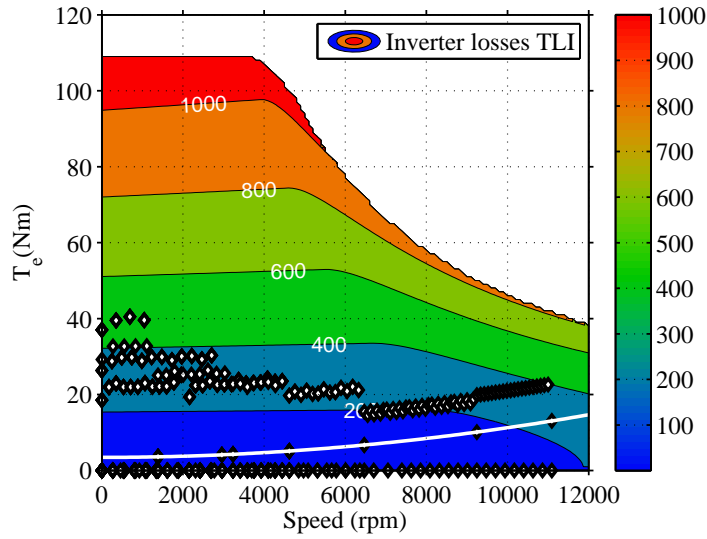


Figure 5.1: Calculated inverter power loss for the TLI. Description as in Fig. 4.1.

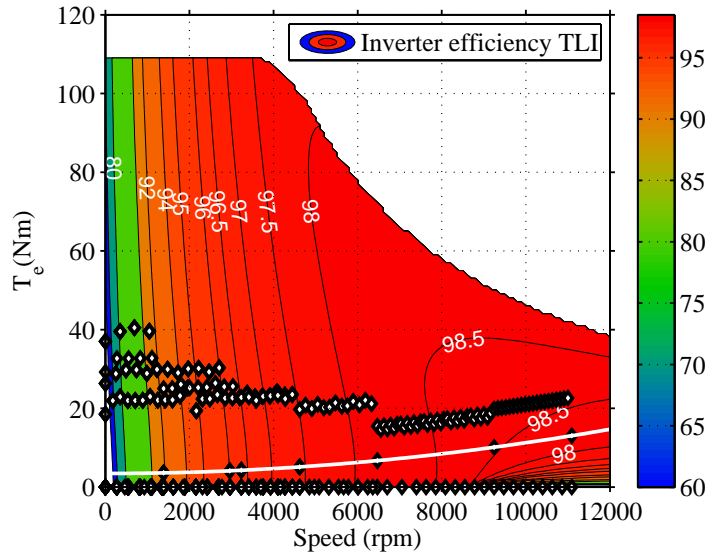


Figure 5.2: Calculated inverter efficiency for the TLI. Description as in Fig. 4.1.



the field weakening region is entered, a current to demagnetize the machine is needed which increases the losses at higher speeds.

The efficiency of the inverter is shown in Fig. 5.2. Since the losses and the output power both increase proportionally to the torque, the efficiency of the inverter is not particularly dependant of the torque. Since the losses are not dependant on the speed but the output power is, it can be seen that the efficiency increases with speed. At high speeds and low torques the output power is low but the inverter has relatively high losses. These losses are due to that the inverter needs to supply a current to demagnetise the machine in the field weakening region (i.e. reactive current), and the inverter efficiency therefore drops at high speeds.

### **Multilevel inverter**

The inverter losses with the MLI at different speeds and torques produced by the electrical machine can be seen in Fig. 5.5 for the MLI presented in Table 4.3. The conductive loss, using (3.19) and (3.20), and the switch loss, using (3.23) and (3.24), can be seen in Fig. 5.3 and Fig. 5.4. It can be noted that the conductive loss in the MOSFETs totally dominates the losses since the inverter is only switched at the fundamental frequency. Even at the maximum speed, the switching losses never exceeds 15 W for the inverter. Since the conductive loss in a MOSFET is proportional to the square of the current, the loss increases with the square of the torque in the region without field weakening. In the field weakening region the losses increase for a certain torque as the speed increases, since extra current is needed to demagnetize the machine.

The efficiency of the MLI can be seen in Fig. 5.6. Since the power loss is proportional to the square of the torque and the output power is proportional to the torque, this means that at a certain speed the efficiency drops for higher torques. When increasing the speed, the output power increases and the loss remains fairly constant for a certain torque. This causes the efficiency to increase at higher speeds. When entering the field weakening region, the efficiency drops since more current is needed to demagnetize the machine.

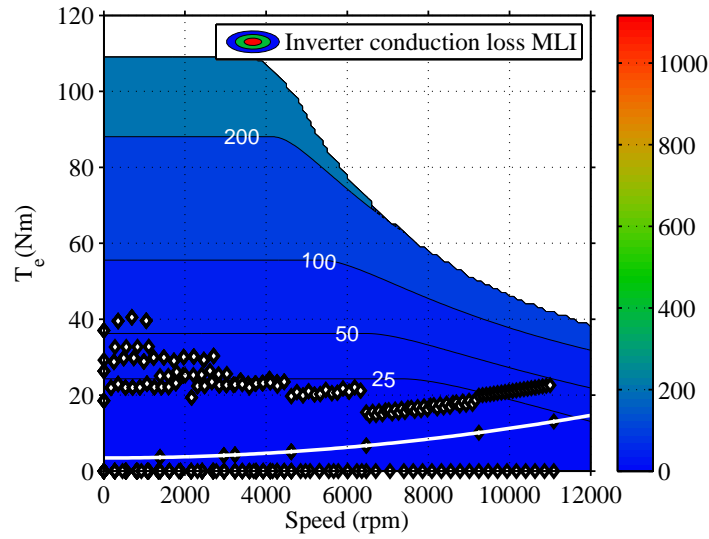


Figure 5.3: Calculated inverter conduction loss for the MLI. Description as in Fig. 4.1.

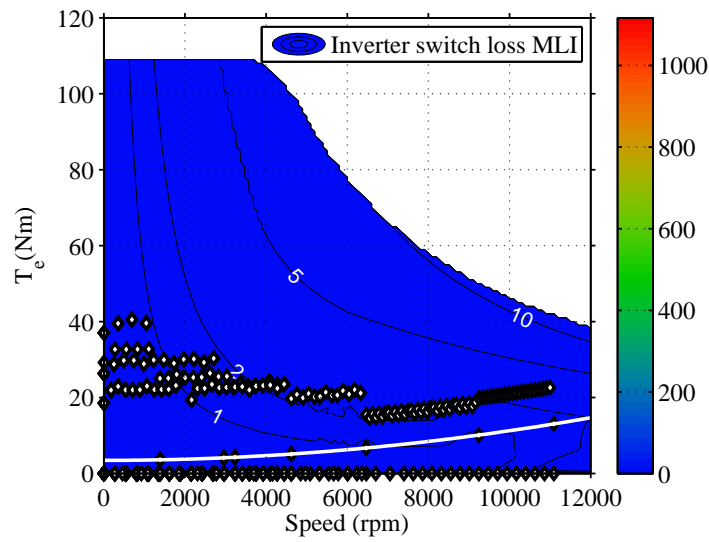


Figure 5.4: Calculated inverter switch loss for the MLI. Description as in Fig. 4.1.

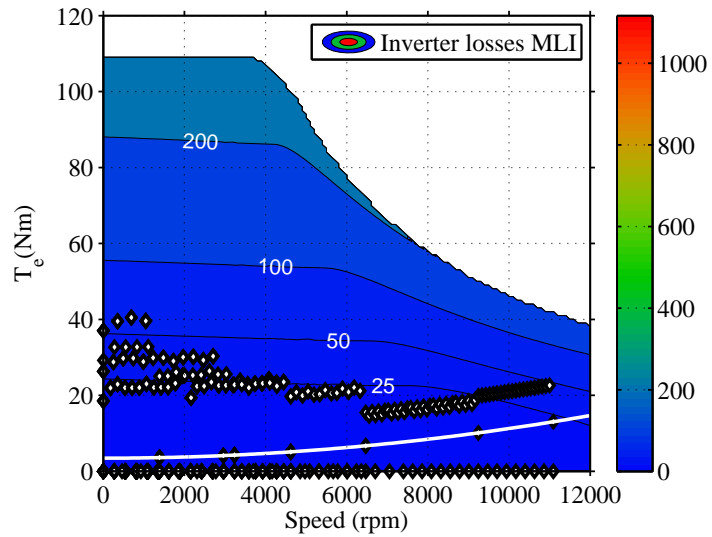


Figure 5.5: Calculated inverter power loss for the MLI. Description as in Fig. 4.1.

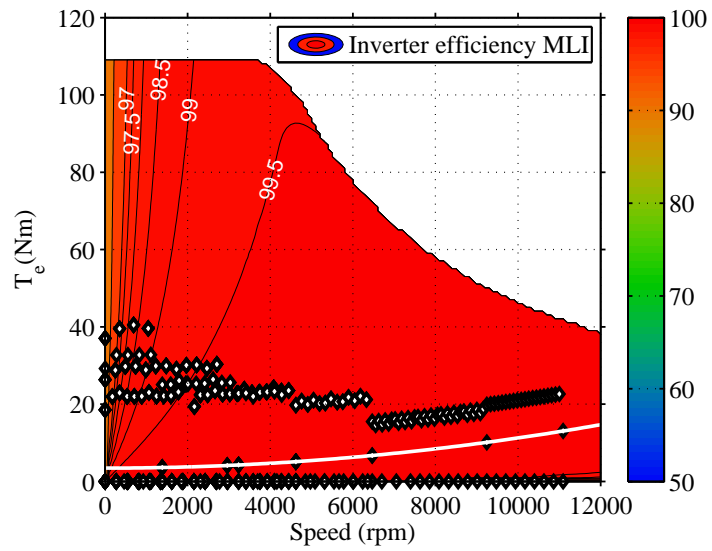


Figure 5.6: Calculated inverter efficiency for the MLI. Description as in Fig. 4.1.

### 5.1.2 Battery

The battery loss for the car when using a TLI is shown in Fig. 5.7 for the battery presented in Section 4.1.2. Since the whole battery supplies the power to the electric machine and the voltage in the battery is assumed to be constant, the battery current becomes proportional to the active power supplied to the machine. The losses in the battery then become proportional to the square of the electric machine power. This can be seen in Fig. 5.7 for all operation points. Due to that the TLI balances the reactive power in the separate phases already in the inverter and also smoothens a very high frequency ripple with its DC-link capacitor, the battery utilization becomes as good as it can be with the TLI. When switching to a MLI the question is, how much extra losses will be added.

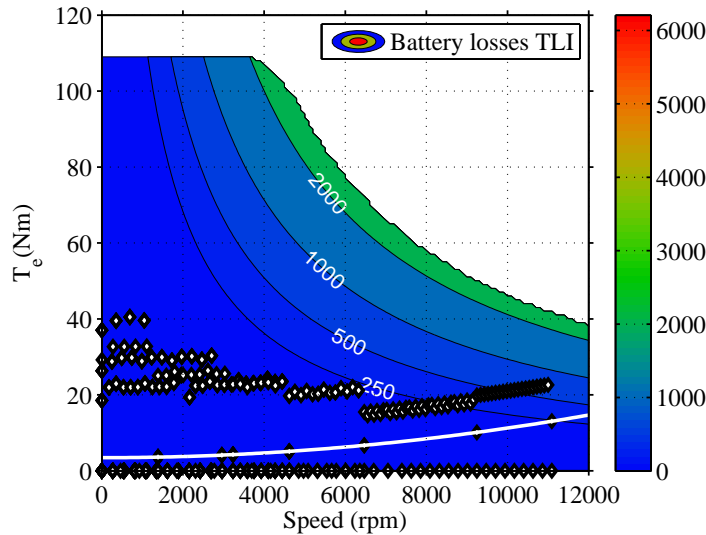


Figure 5.7: Calculated losses in the battery when using a TLI. Description as in Fig. 4.1.

In this chapter, two battery loss investigation will be performed. One with no filter capacitors over the battery groups and on with an extremely large capacitor. This is done in order to provide the complete loss range that the battery in the MLI can be exposed to. In Chapter 7 a more through investigation of the capacitor influence will be performed where a variation of capacitor sizes and chemistries will be used.

The battery losses when operating the vehicle with infinity large capacitors to the input of a MLI can be seen in Fig. 5.8. The battery loss will be

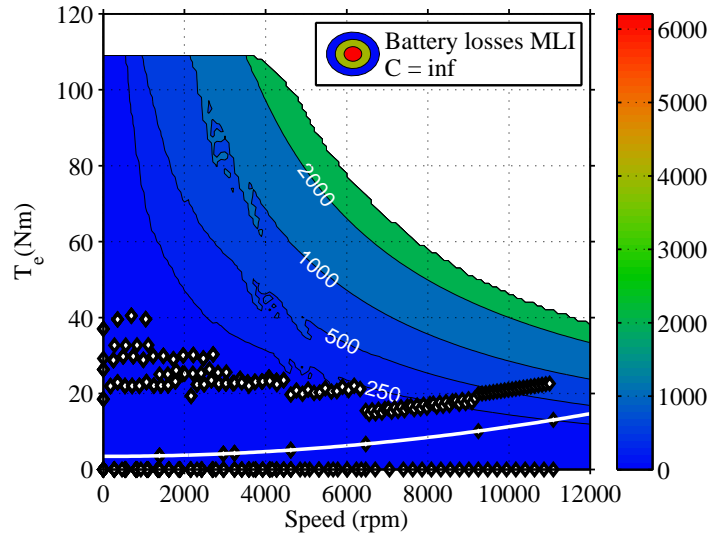


Figure 5.8: Calculated losses in the battery when using a MLI with infinity large filter capacitances. Description as in Fig. 4.1.

higher when using a MLI drive system compared to a TLI, even with these capacitors. This is due to that the current in the different groups will not be equal when operating the inverter with FSHE, even though the current is assumed to be pure DC.

The battery loss when operating the vehicle with a MLI without filter capacitors on the input of the H-bridges can be seen in Fig. 5.9. One can see that the losses are much higher now. The battery now needs to supply the reactive power, higher current, but also take care of that the battery power is not taken out as a smooth current.

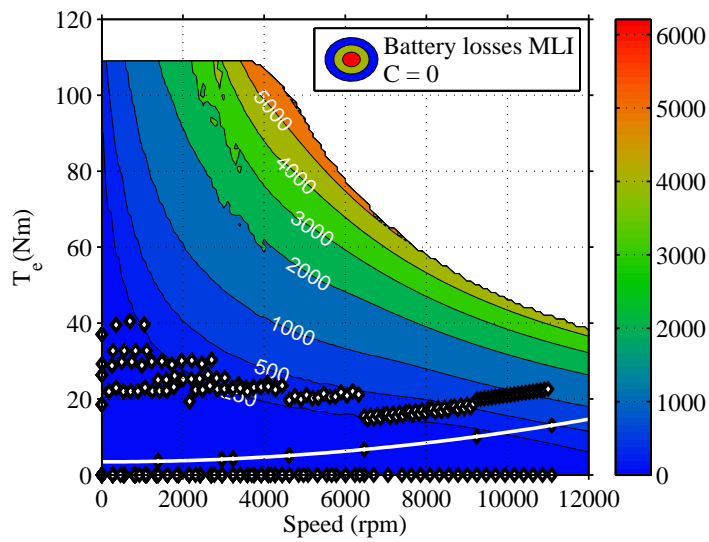


Figure 5.9: Calculated losses in the battery when using a MLI without filter capacitances. Description as in Fig. 4.1.

### 5.1.3 Combined inverter and battery losses

The total inverter-battery losses that are analysed and presented below, consist of the inverter losses and the battery losses. The machine losses are assumed to be equal for the two inverters and are therefore excluded in this analysis.

For the TLI, the total losses of the battery and the inverter are shown in Fig. 5.10.

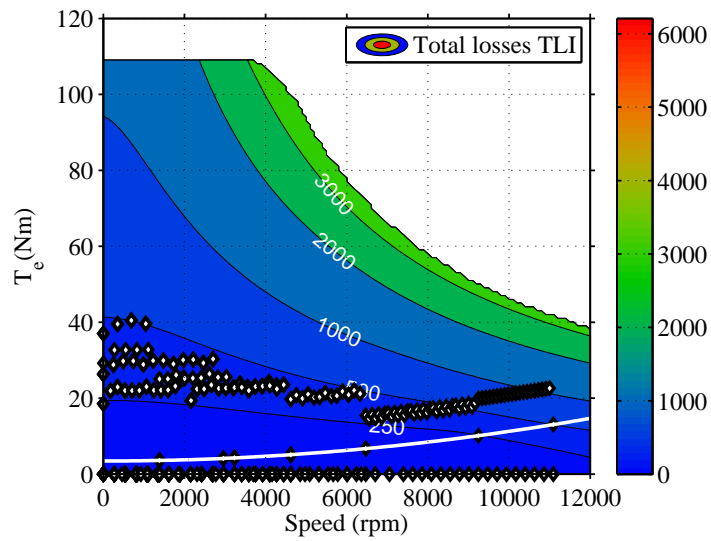


Figure 5.10: Calculated inverter and battery losses for the TLI. Description as in Fig. 4.1.

For the MLI with large capacitors in parallel to the input of the H-bridges, the losses are shown in Fig. 5.11, and for the MLI without input capacitors the losses are shown in Fig. 5.12. The drive system with the MLI with large capacitors shows an advantage over the TLI drive system at all operating points. For the MLI system without capacitors, as expected, the losses become larger than for the TLI systems at high speeds and high output power. Only at the lowest speed range there is a benefit for the MLI system also for high torques. In order to evaluate the accumulated loss picture, drive cycle analysis must be performed. The result of such a study is presented in Section 5.2.

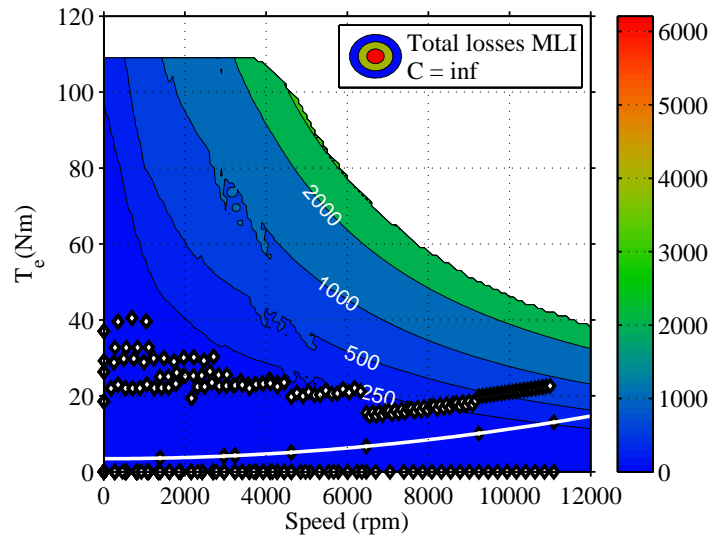


Figure 5.11: Calculated inverter and battery losses for the MLI with capacitors. Description as in Fig. 4.1.

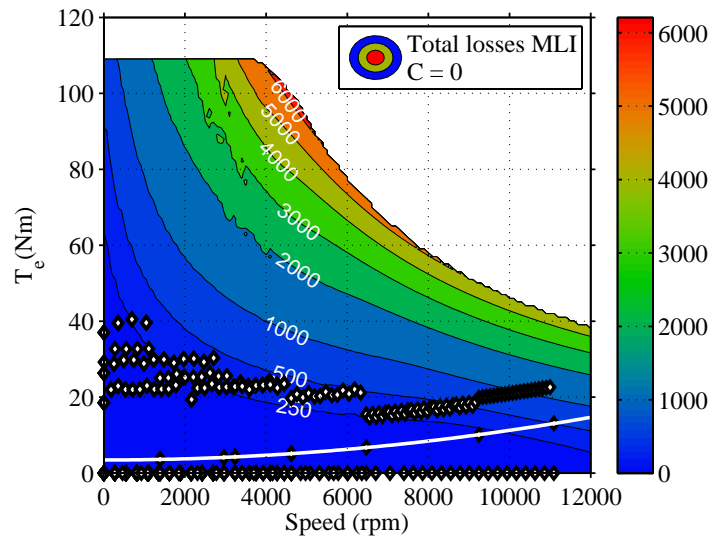


Figure 5.12: Calculated inverter and battery losses for the MLI without capacitors. Description as in Fig. 4.1.



#### 5.1.4 Loss comparison

In the 2D-contours in the previous section, it was not easy to make a comparison between the loss maps. Therefore the loss comparison will be performed using graphs for fixed torques instead.

The losses in the inverters for different speeds and a fixed torque of  $10 Nm$  are shown in Fig. 5.13, and for a torque of  $60 Nm$  in Fig. 5.14. It can be seen that the MLI has lower inverter losses for all operating points. It can also be noticed that the inverter losses for both the MLI and the TLI increase a lot when entering the field weakening region.

The losses in the battery for different speeds and a fixed torque of  $10 Nm$  are shown in Fig. 5.15, and for a torque of  $60 Nm$  in Fig. 5.16. The losses in the battery for the TLI are lowest for all speeds. This is due to that the current out from the battery is a pure DC. The battery losses for the MLI with infinitely large capacitors to the inputs of the H-bridges are a bit higher. The batteries do not supply the uneven current from the reactive power demand of the electric machine, but some of the battery modules have a higher current than other ones, even though they have a pure DC current. The losses for the MLI without capacitors are higher for all speeds, especially when entering the field weakening region. The batteries must then supply the waveforms to form the increased reactive power needed by the electric machine at this region and this increases the losses due to a higher battery current.

The total losses for the drive systems for different speeds and a fixed torque of  $10 Nm$  is shown in 5.17, and in Fig. 5.18 the total losses are shown for a torque of  $60 Nm$ . When operating the machine at low torques, the losses for the MLI drive system are lower for low speeds. When entering the field weakening region the battery losses increase drastically for the MLI drive system since the uneven waveforms needed to form the reactive power needed by the electric machine can not be supplied from the capacitors and instead must come from the battery. For higher torques the TLI drive system shows lower losses for almost all speeds, if one does not have the possibility to filter out the reactive power and the harmonic content from the battery in the MLI drive system. As mentioned before, the electric machine will on the other hand not operate at this high torque very often which makes the energy efficiency to be potentially higher for the MLI system. This calls for a complete drive cycle analysis.

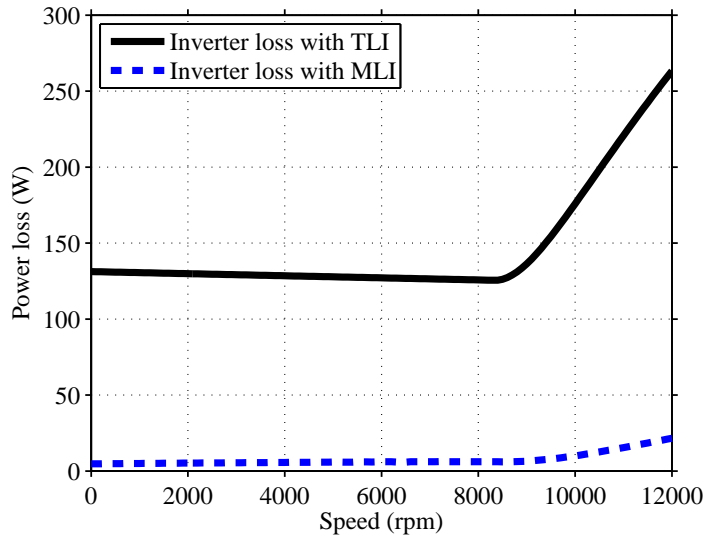


Figure 5.13: Calculated inverter power loss for T=10 Nm.

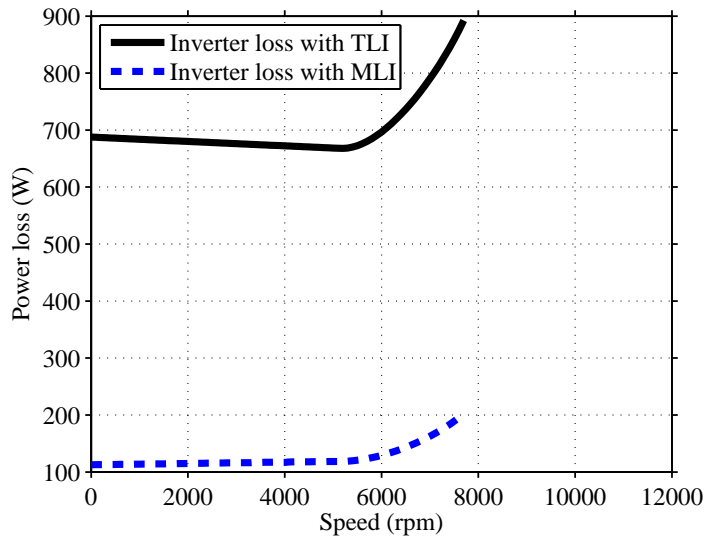


Figure 5.14: Calculated inverter power loss for T=60 Nm.

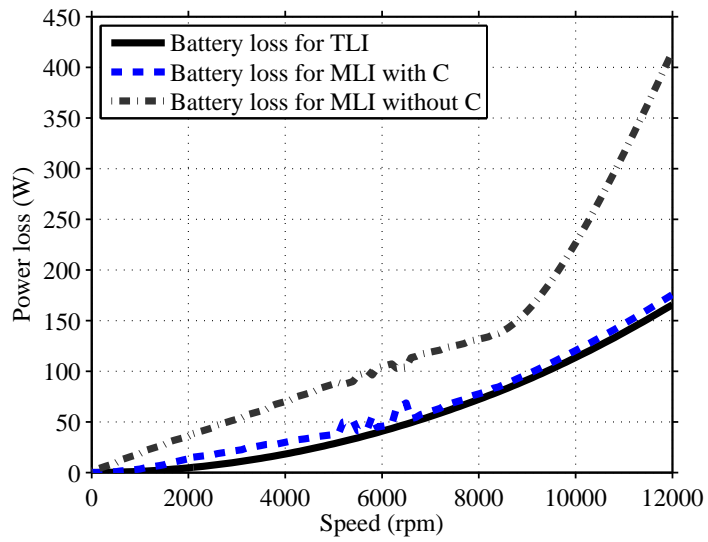


Figure 5.15: Calculated battery power loss for  $T=10$  Nm.

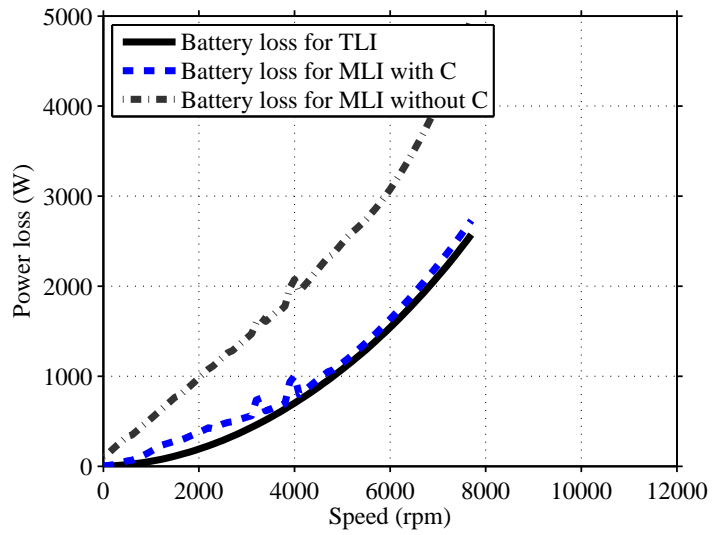


Figure 5.16: Calculated battery power loss for  $T=60$  Nm.

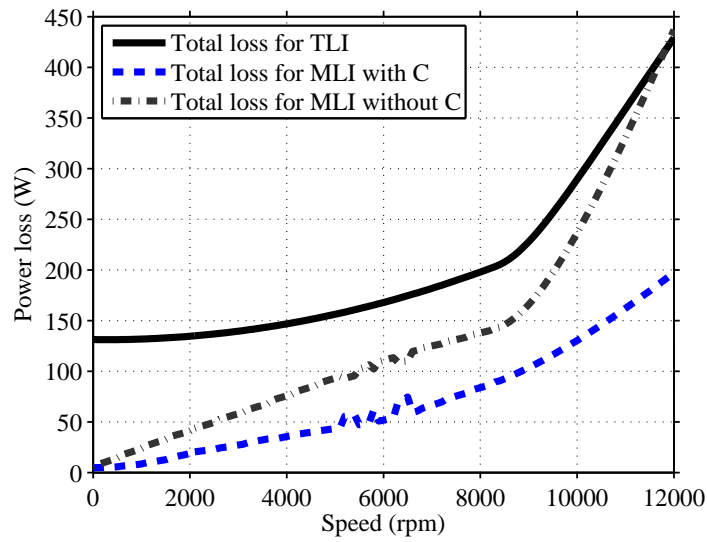


Figure 5.17: Calculated total loss for  $T=10$  Nm.

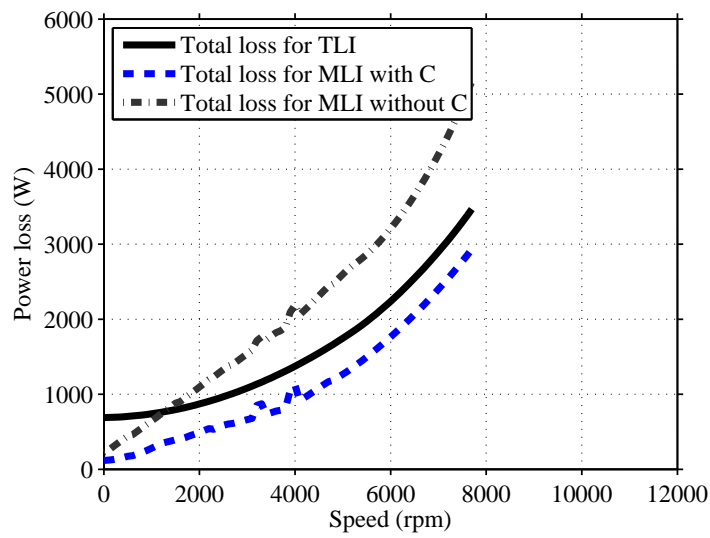


Figure 5.18: Calculated total loss for  $T=60$  Nm.

### 5.1.5 Charging

The losses when using the inverter as a charger can be seen in Fig 5.19 and in Table 5.1. For the two lower power alternatives the MLI shows a benefit in efficiency, for higher power the battery losses increase compared to the TLI case if the battery current is not filtered. The efficiency is shown in Fig. 5.20. It is seen that the efficiency is higher at the lower input current and that the MLI is the most attractive alternative except for the highest power level where the losses are very similar between the unfiltered MLI case and the TLI case. If the possibility to filter the battery current exists, the MLI case shows a large reduction of the losses. The efficiency during charging might on the other hand not be such an important design criteria, it is more important to be able to control where the losses occur.

Table 5.1: Total losses for different charging power

Charging	Input Power	TLI	MLI	
			$C = \infty$	$C = 0 \text{ mF}$
3 Phase 10 A	6900 W	154 W	54 W	86 W
3 Phase 16 A	11040 W	294 W	139 W	220 W
3 Phase 32 A	22080 W	844 W	556 W	878 W

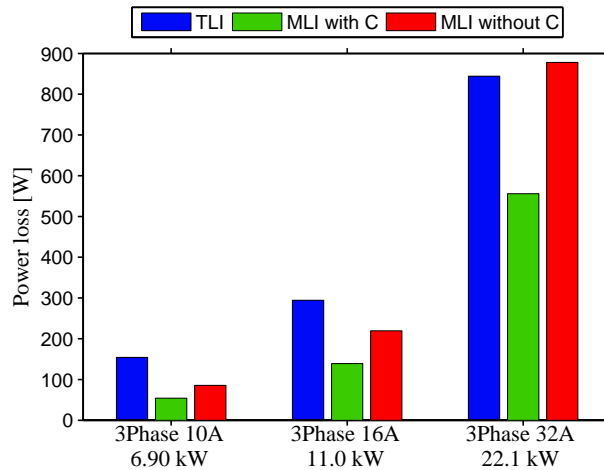


Figure 5.19: Calculated inverter-battery losses for different charging powers.

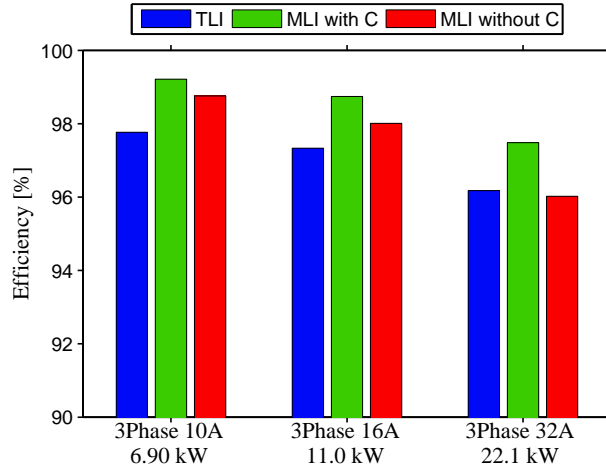


Figure 5.20: Calculated inverter-battery efficiency for different charging power

## 5.2 Drive cycle evaluation

The accumulated energy loss for the battery and the inverter are now analyzed using the NEDC, the FTP75, the HWFET and the US06 drive cycles for the vehicle presented in Table 4.1.

### 5.2.1 NEDC

The torque and speed profile for the NEDC drive cycle are shown in Fig. 5.21 and in Fig. 4.5.

The battery and inverter accumulated losses for the three different setups are shown in Fig. 5.22. One can see that the accumulated losses for the TLI drive system becomes the worst ending up at  $43 Wh$ . The MLI that does not have capacitors to filter out the reactive power and harmonic content uses  $30 Wh$ . This is an improvement over the TLI and as can be seen in Fig. 5.29, the inverter losses have been reduced substantially. The battery losses are increased but the sum is reduced. When having a large enough capacitor to the input of the H-bridges the reactive power supply is assumed to be taken from these capacitors instead of the battery. The losses in the battery are then reduced to only  $13 Wh$  instead of  $27 Wh$ . The total losses are then reduced to  $16 Wh$ .

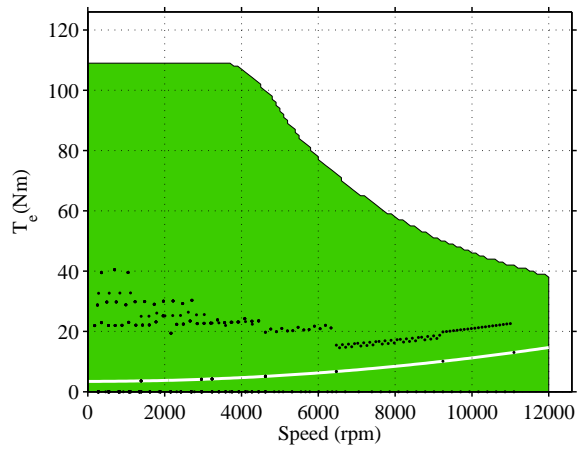


Figure 5.21: Operation points of the electric machine during NEDC

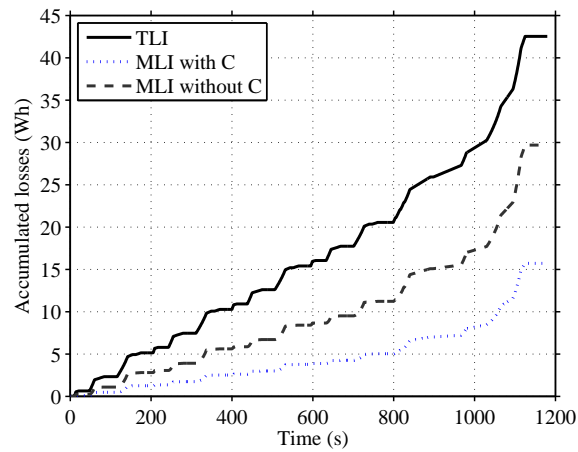


Figure 5.22: Losses during the NEDC drive cycle

## 5.2.2 FTP75

The torque and speed profile for the FTP75 drive cycle are shown in Fig. 5.23 and in Fig. 4.5.

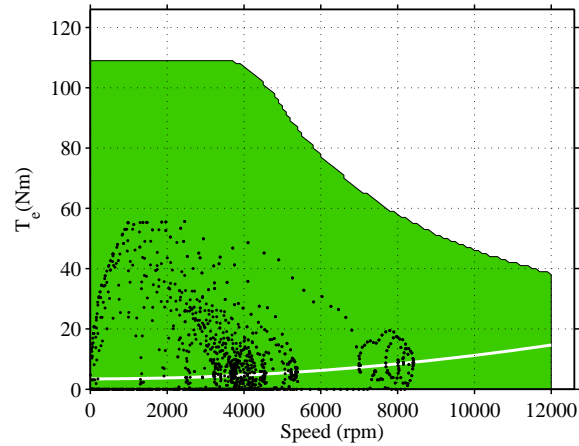


Figure 5.23: Operation points of the electric machine during the FTP75 drive cycle

The accumulated losses for the three different setups are shown in Fig. 5.24.

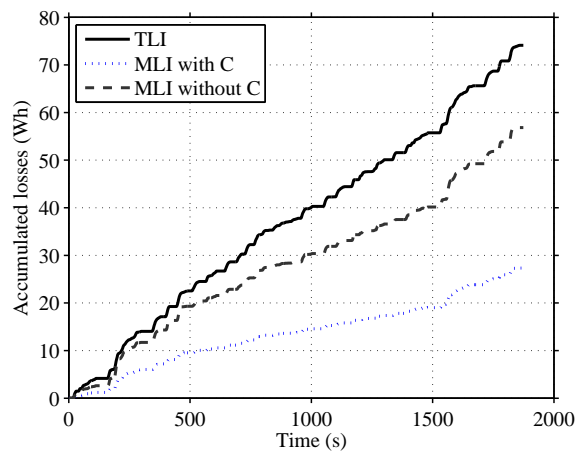


Figure 5.24: Losses during the FTP75 drive cycle



### 5.2.3 HWFET

The torque and speed profile for the HWFET drive cycle are shown in Fig. 5.25 and in Fig. 4.5.

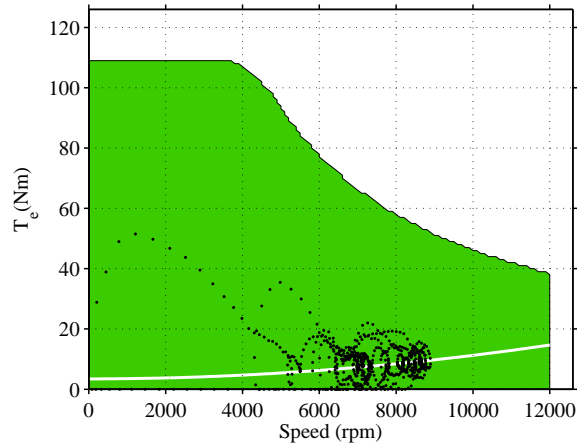


Figure 5.25: Operation points of the electric machine during the HWFET drive cycle

The accumulated losses for the three different setups are shown in Fig. 5.26.

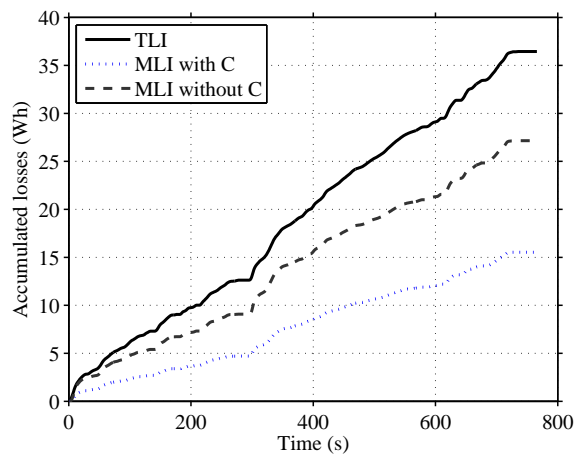


Figure 5.26: Losses during the HWFET drive cycle

### 5.2.4 US06

The torque and speed profile for the US06 drive cycle are shown in Fig. 5.27 and in Fig. 4.5.

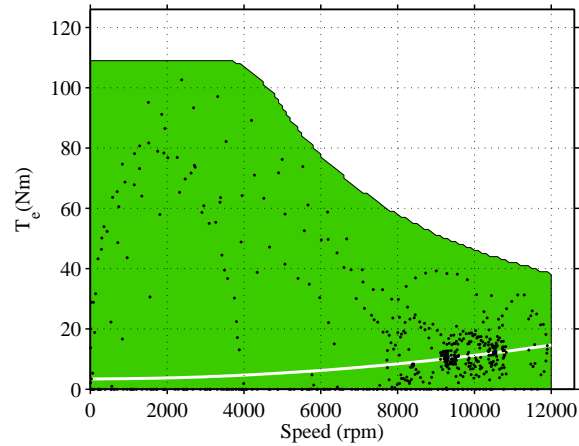


Figure 5.27: Operation points of the electric machine during the US06 drive cycle

The accumulated losses for the three different setups are shown in Fig. 5.28.

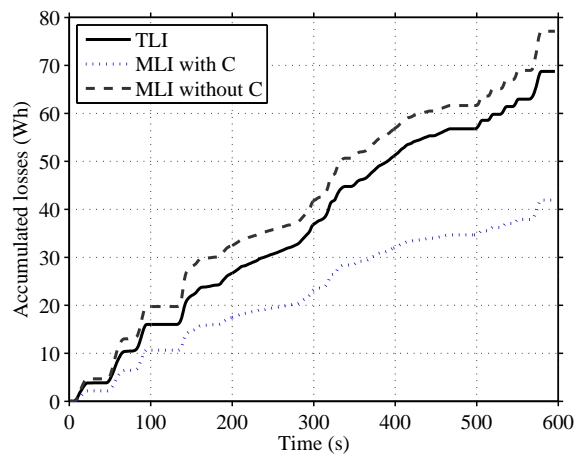


Figure 5.28: Losses during the US06 drive cycle

### 5.2.5 Comparison between proposed topology and classical inverter

The accumulated battery and inverter losses for the four drive cycles and the three systems are presented in Table 5.2 and Fig. 5.29. It can be seen that the MLI is a beneficial choice compared to the TLI for all drive cycles except the high speed US06. When using infinitely big capacitors to filter the battery current to DC for the MLI system, the MLI system shows much lower losses compared to the TLI system.

Table 5.2: Calculated accumulated energy loss for the inverter and battery

Drive cycle	TLI	MLI	
		$C = \infty$	$C = 0 \text{ mF}$
NEDC	43 Wh	16 Wh	30 Wh
FTP75	74 Wh	27 Wh	57 Wh
HWFET	36 Wh	16 Wh	27 Wh
US06	69 Wh	42 Wh	77 Wh

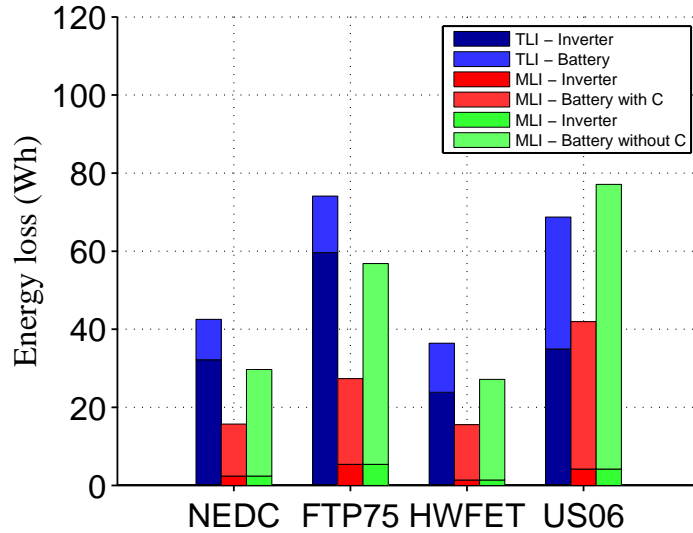


Figure 5.29: Calculated accumulated drive cycle loss

### 5.3 40 kWh battery

A 40 kWh battery gives an approximate driving of 200 km, a suitable choice for a pure electric vehicle. When increasing the battery size for the vehicle, the battery resistance is lowered. Therefore the battery losses compared to a smaller battery is lowered. In Fig. 5.30, the battery loss when using a 40 kWh battery is shown. It can be noticed that the battery loss for all operating points are lowered by a factor of 4 compared to the previously used 10 kWh battery shown in Fig. 5.7.

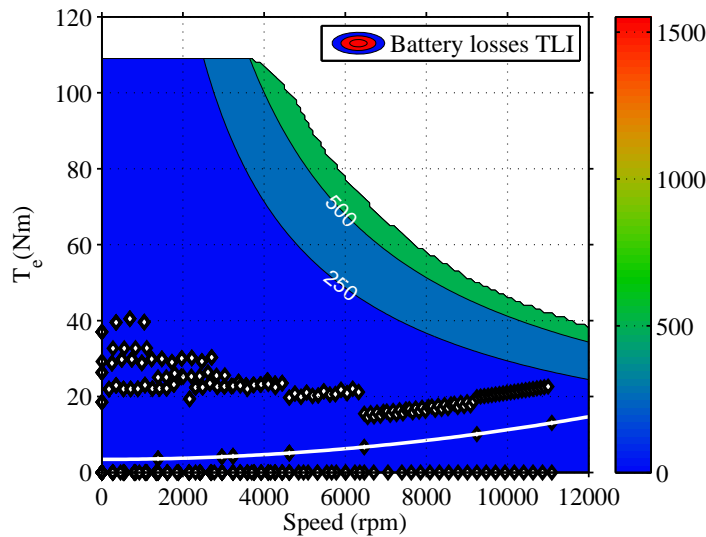


Figure 5.30: Calculated losses in the 40 kWh battery when using a TLI. Description as in Fig. 4.1.

The same energy content is also placed in the MLI setup giving a resulting loss map shown in Fig. 5.31. The losses for this setup is also lowered with a factor of 4 compared to the 10 kWh system shown in Fig. 5.9.

When operating the vehicle with the 40 kWh batteries in drive cycles, the battery loss part of the accumulated loss is lowered by a factor of 4, see Fig. 5.32. For the TLI system, this has a minor influence since the inverter loss was dominant already in the 10 kWh case. For the MLI case, the situation is the opposite. In the 10 kWh case the battery loss was the dominant part of the accumulated loss during the drive cycles. By increasing the battery pack to 40 kWh, the battery loss is lowered and thereby the accumulated drive cycles loss is very much reduced. It can be noted that the MLI setup is now beneficial from a loss perspective for all the analysed drive cycles.

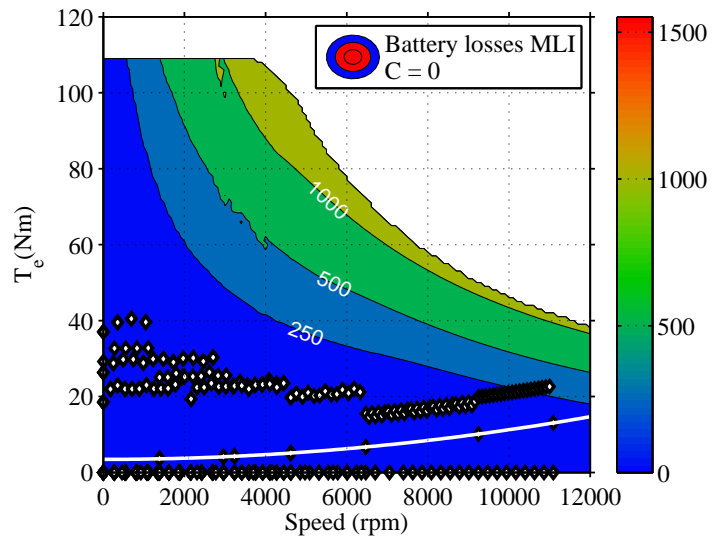


Figure 5.31: Calculated losses in the 40 kWh battery when using a MLI without filter capacitances. Description as in Fig. 4.1.

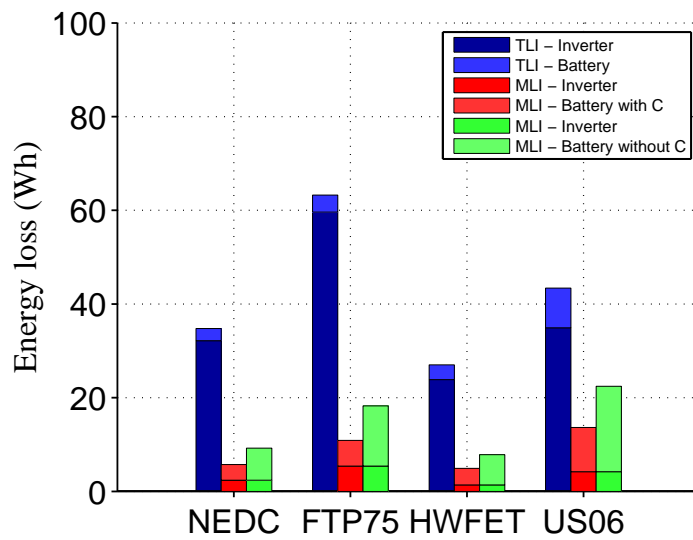


Figure 5.32: Calculated accumulated drive cycle loss for 40 kWh battery.

## 5.4 Slim sizing of the inverter semiconductors

The selected IGBT for the previous analysis is the FS800 from Infineon. It has a maximum current of 800 A meaning about 400 A rms current as maximum value. If instead the FS400 module is selected, the losses are not increased much, see Fig. 5.33 compared to Fig. 5.1. The fixed voltage drop still exists, the resistance is increased, but the switching losses are decreased a bit. If the FS400 is used instead of the FS800 the losses in the TLI therefore remains quite constant, however, this module can not dissipate the same amount of power loss so a degradation of the performance might be needed during specific conditions.

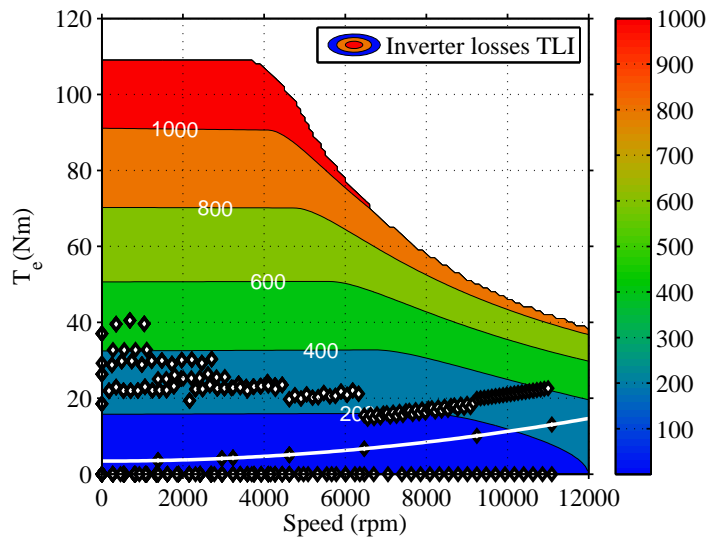


Figure 5.33: Calculated inverter power loss for the slim sized TLI. Description as in Fig. 4.1.

The current rating of the IGBT module for the TLI system in Fig. 5.33 is reduced to half. To make a fair comparison the amount of semiconductors in the MLI system is decreased to half, putting an equivalent of 2.5 MOSFETs in parallel for each switch position in the H-bridge. The equivalent resistance for the MOSFETs are thereby doubled and since the switching losses for the MLI system are almost neglectable, the losses are quite simply doubled, see Fig. 5.34 compared to Fig. 5.5.

Operating the vehicle with the slim sized inverter in drive cycles, the accumulated loss for the TLI system is marginally changed. For the MLI system, the inverter loss is about doubled but since the battery loss for this

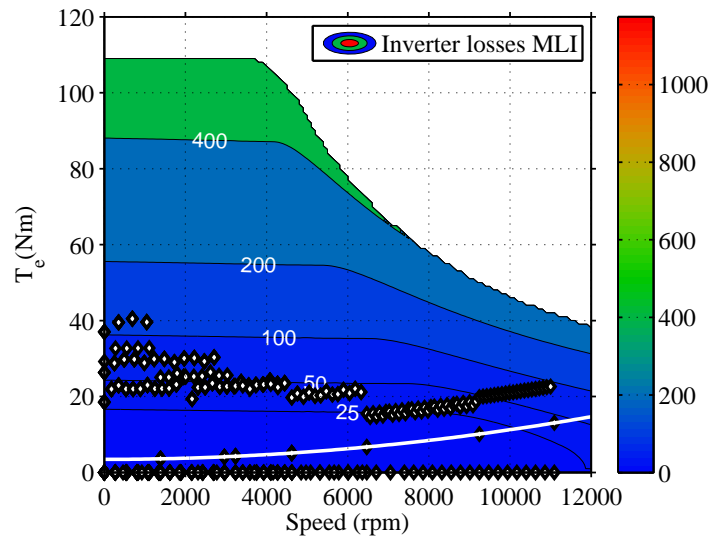


Figure 5.34: Calculated inverter power loss for the slim sized MLI. Description as in Fig. 4.1.

system is dominant, it does not influence the accumulated loss very much. The MLI system is still the beneficial choice compared to the TLI system for all analysed drive cycles except the US06 drive cycle.

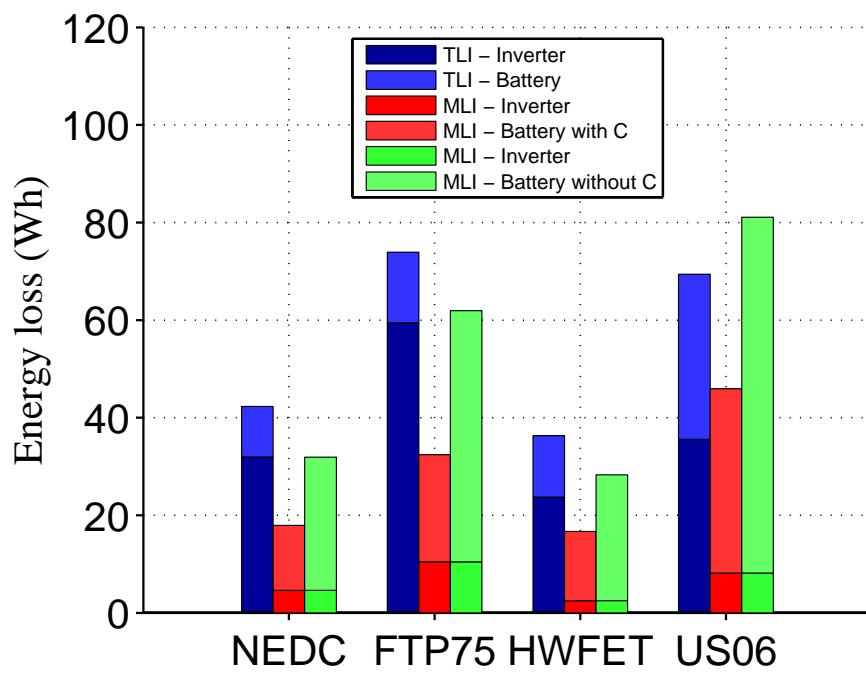


Figure 5.35: Calculated accumulated drive cycle loss for the slim sized systems.



## Chapter 6

# Battery loss modeling

To be able to calculate the battery loss and performance, a suitable model of the battery is needed. Since the multilevel inverter stresses the battery with a pulsed current which has a frequency of twice the fundamental electric machine frequency, the models and parameters commonly used for simulations of hybrid electric vehicles might not be suitable. In particular the method of using a pure resistance, which might be a function of SOC and temperature, as well as current direction. The battery cell is here modelled using the Randles model, see [19], with three time constants and can be seen in Fig. 6.1. The model is chosen to include three time-constants to be able to cover all the frequency domains that the battery is operated at.  $R_0$  to  $R_3$  and  $C_1$  to  $C_3$  describe the dynamic performance, and  $V_{OCV}$  is the open circuit voltage which is dependant on the SOC. Since the frequency range is below a couple of kHz, the battery inductance is assumed to be neglectable in the further analysis.

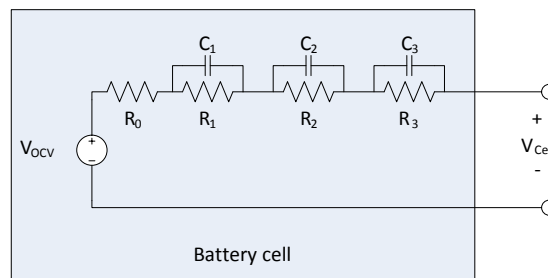


Figure 6.1: The three time constants Randles model of the battery cell

## 6.1 Parameter extraction

Cell measurements are done on a ANR26650M1A cell from A123 systems for different SOCs at a temperature of 25 °C. A resistive load is connected to the output of one H-bridge and one cell is used as input. The cell voltage and current is measured with an oscilloscope. The H-bridge is then controlled to stress the battery cell with a pulsed current of different magnitudes (28 A and 49 A) and various frequencies (1-100 Hz).

The three time constants Randles model shown in Fig. 6.1 has an impedance that is mathematically described as

$$Z_{cell}(s) = \frac{b_3 s^3 + b_2 s^2 + b_1 s + b_0}{s^3 + a_2 s^2 + a_1 s + a_0} \quad (6.1)$$

or with its corresponding poles,  $p_3$ ,  $p_2$  and  $p_1$ , and zeros,  $z_3$ ,  $z_2$  and  $z_1$  as

$$Z_{cell}(s) = b_3 \frac{(s - z_3)(s - z_2)(s - z_1)}{(s - p_3)(s - p_2)(s - p_1)}. \quad (6.2)$$

The corresponding electrical parameters can be calculated from the least-square fit impedance model knowing the transfer function and its corresponding poles. From the poles, the system time constants are calculated according to

$$\begin{bmatrix} \tau_3 \\ \tau_2 \\ \tau_1 \end{bmatrix} = - \begin{bmatrix} 1/p_3 \\ 1/p_2 \\ 1/p_1 \end{bmatrix}. \quad (6.3)$$

Knowing the time constants, a matrix A is created according to

$$A = \frac{1}{\tau_1 \tau_2 \tau_3} \cdot \begin{bmatrix} \tau_1 \tau_2 \tau_3 & 0 & 0 & 0 \\ \tau_1 \tau_2 + \tau_1 \tau_3 + \tau_2 \tau_3 & \tau_2 \tau_3 & \tau_1 \tau_3 & \tau_1 \tau_2 \\ \tau_1 + \tau_2 + \tau_3 & \tau_2 + \tau_3 & \tau_1 + \tau_3 & \tau_1 + \tau_2 \\ 1 & 1 & 1 & 1 \end{bmatrix} \quad (6.4)$$

which can be used to calculate the resistances as

$$\begin{bmatrix} R_3 \\ R_2 \\ R_1 \\ R_0 \end{bmatrix} = A^{-1} \begin{bmatrix} b_3 \\ b_2 \\ b_1 \\ b_0 \end{bmatrix}. \quad (6.5)$$

The capacitances can now be calculated as

$$\begin{bmatrix} C_3 \\ C_2 \\ C_1 \end{bmatrix} = \begin{bmatrix} \tau_3 & 0 & 0 \\ 0 & \tau_2 & 0 \\ 0 & 0 & \tau_1 \end{bmatrix} \begin{bmatrix} 1/R_3 \\ 1/R_2 \\ 1/R_1 \end{bmatrix}. \quad (6.6)$$

If the Randles system instead is a two or one time-constant system, the least-square system is calculated in a corresponding way.

The impedance is determined using a least-square fit on the measured data and a part of one measurement can be seen in Fig. 6.2. Apart from the 3p3z model, a 2p2z and a 1p1z as well as a resistive model is parameterised. It can be noted that the 2p2z, 1p1z and resistive model does not fit the high frequency behaviour very well, but show a great match for lower frequencies where the pulsed waveform goes towards steady state. However, the 3p3z fit shows a great fit for the whole curve with a normalized root mean square deviation of 99.49 %.

The resulting Bode plot for the least-square curve fits for the 3p3z model for different measurements are shown in Fig. 6.3. First, it can be noted that the magnitude fit is excellent when using the model with three poles and three zeros. Moreover it can be observed that the impedance becomes a bit higher at higher currents when comparing the four measurements in Fig. 6.3. An EIS sweep has also been performed in the frequency range of 10 *mHz* to 10 *kHz* using the network analyser "Gamry reference 3000".

The resulting parameters and normalized root mean square deviation of the curve fits can be seen in Table 6.1. For the further analysis the data set 'meas 3.23V 1Hz 28A' is chosen due to that it matches the measurements at both low and high frequencies, see Fig. 6.2.

Moreover, it can be noted that a DC resistance of 15 *mΩ* much better represents the battery cell compared to the 10 *mΩ* specified in the data sheet.

## 6.2 Verification in experimental system

To verify the theory assumptions and to demonstrate the concept correctness, the small scale experimental system seen in Fig. 4.6 is utilised. The battery pack consists of 4 cells in series, connected to each H-bridge, which gives a nominal voltage of 13.2 *V* for each H-bridge, and a total inverter capacity of 270 *Wh*. This gives a scale in voltage as

$$V_{LargeScale} = 3.8 \cdot V_{SmallScale} \quad (6.7)$$

and a scale in current as

$$I_{LargeScale} = 9.7 \cdot I_{SmallScale}. \quad (6.8)$$

When four cells are connected into a battery pack, busbars and/or cables are needed to connect the battery to the inverter. In order to account for this additional resistance, a resistance  $R_{cable}$  is modeled in series with the

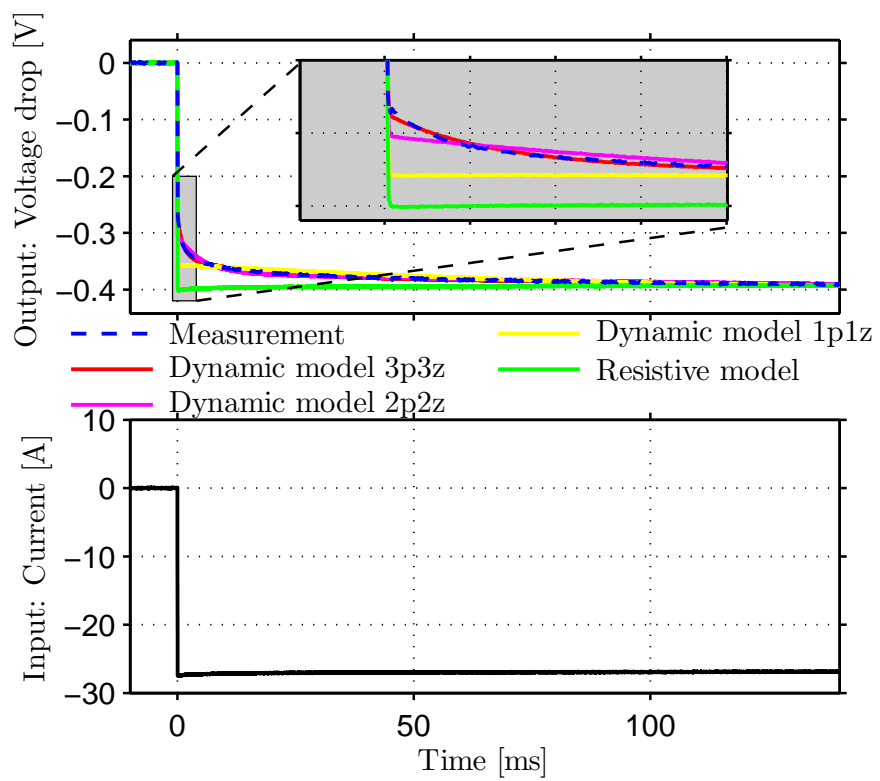


Figure 6.2: Operating point at 1 Hz, 28 A (12.2 C) and 3.23 V. The voltage drops of the models and the measurements are a result of the current step.

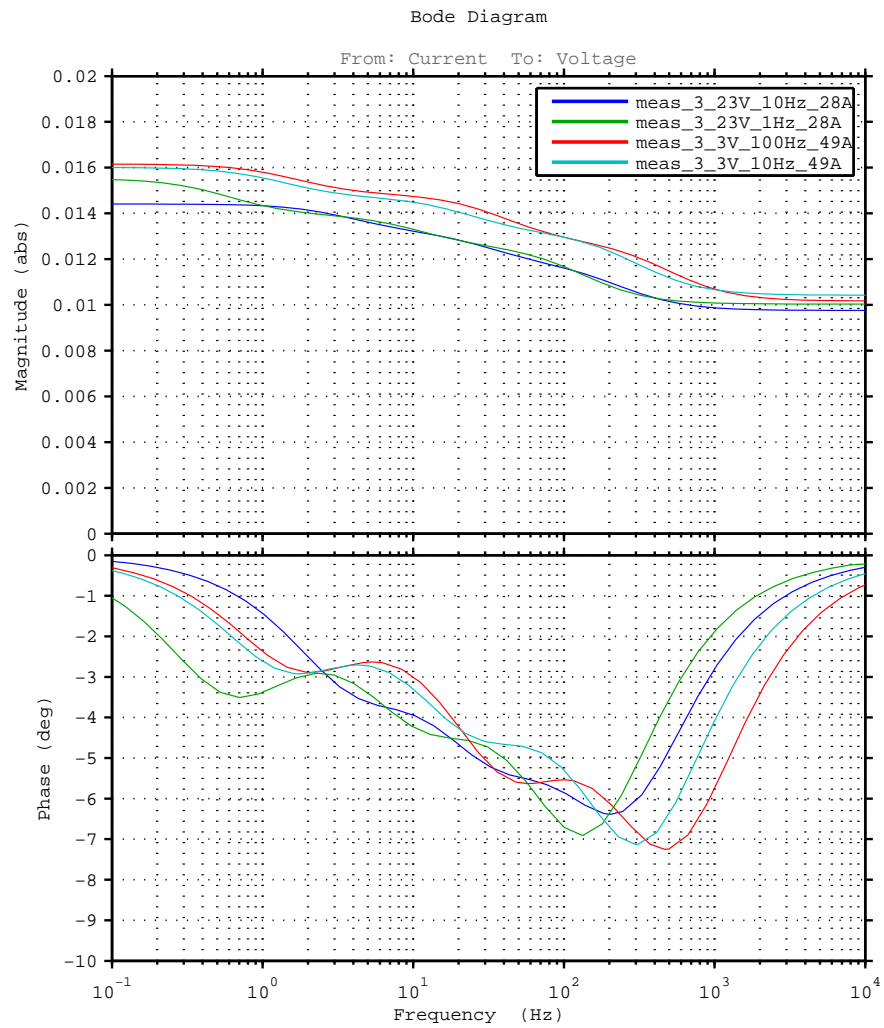


Figure 6.3: Bode plot for the extracted parameters.

Table 6.1: Cell parameters.

Measurement:	R0 [ $m\Omega$ ]	R1 [ $m\Omega$ ]	R2 [ $m\Omega$ ]	R3 [ $m\Omega$ ]	C1 [F]	C2 [F]	C3 [F]	Fit [%]
meas 3.3V 100Hz 49A 3p3z	10.16	2.55	2.05	1.26	0.13	1.92	65.31	98.63
meas 3.3V 10Hz 49A 3p3z	10.41	2.67	1.58	1.21	0.20	4.11	84.65	99.40
meas 3.23V 10Hz 28A 3p3z	9.76	1.96	1.43	1.21	0.35	3.43	33.06	99.42
meas 3.23V 1Hz 28A 3p3z	10.02	2.47	1.41	1.37	0.49	9.93	168.94	99.49
meas 3.23V 1Hz 28A 2p2z	11.07	2.60	1.45	-	1.98	110.98	-	99.23
meas 3.23V 1Hz 28A 1p1z	13.04	1.90	-	-	41.61	-	-	97.92
meas 3.23V 1Hz 28A Resistive	14.61	-	-	-	-	-	-	93.99

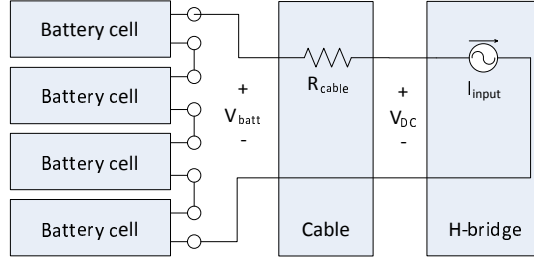


Figure 6.4: Model of a battery pack, the cable and the optional input filter for the small scale system.

battery pack and was measured to  $9.17\text{ m}\Omega$ . The system, when connected to the multilevel inverter, can be seen in Fig. 6.4.

It should be noted that the battery cable resistance is unreasonable high in the small scale system. In the full scale system it is scaled according to the battery cells and becomes lower, unfortunately not as low as a commercial vehicle would have.

### 6.2.1 Representative operating points for the full scale system

A vehicle operates in a wide range of speeds and torques, resulting in a wide speed-torque region for the electric drive system [53]. In order to cover the representative operating range of an electrified vehicle, detailed analysis of the battery performance was performed at six representative points taken from Fig. 4.1. The corresponding 6 inverter operating points for the small personal vehicle presented in Table 4.1 with the PMSM machine presented in Table 4.2 are shown in Table 6.2.

Table 6.2: Analysed operating points for the test vehicle system.

Case nr:	n	T	$I_{rms}$	$U_{phase}$	$\varphi$	f
1	1000 RPM	30 Nm	$78 A_{rms}$	$17 V_{rms}$	25 deg	83 Hz
2	1000 RPM	60 Nm	$137 A_{rms}$	$22 V_{rms}$	36 deg	83 Hz
3	1000 RPM	90 Nm	$185 A_{rms}$	$28 V_{rms}$	42 deg	83 Hz
4	5000 RPM	30 Nm	$78 A_{rms}$	$77 V_{rms}$	27 deg	417 Hz
5	5000 RPM	60 Nm	$137 A_{rms}$	$103 V_{rms}$	40 deg	417 Hz
6	10000 RPM	30 Nm	$101 A_{rms}$	$106 V_{rms}$	1 deg	833 Hz

To get the same operating points for the small scale system the operating points are translated according to (6.7) and (6.8) and these are shown in Table 6.3.

Table 6.3: Analysed operating points for the experimental lab setup.

Case nr:	n	T	$I_{rms}$	$U_{phase}$	$\varphi$	f
1	1000 RPM	30 Nm	8 $A_{rms}$	4 $V_{rms}$	25 deg	83 Hz
2	1000 RPM	60 Nm	14 $A_{rms}$	6 $V_{rms}$	36 deg	83 Hz
3	1000 RPM	90 Nm	19 $A_{rms}$	7 $V_{rms}$	42 deg	83 Hz
4	5000 RPM	30 Nm	8 $A_{rms}$	20 $V_{rms}$	27 deg	417 Hz
5	5000 RPM	60 Nm	14 $A_{rms}$	27 $V_{rms}$	40 deg	417 Hz
6	10000 RPM	30 Nm	10 $A_{rms}$	28 $V_{rms}$	1 deg	833 Hz

### 6.2.2 Battery model performance in the MLI

The same measurement procedure is now made with the experimental inverter-battery MLI system for the six different operating points. The desired output voltage from Table 6.3 is recalculated to switching instances and an RL-load is controlled to achieve the desired current and fundamental phase lag. In Fig. 6.5, the battery current and voltage for case no 5 are shown for a small period of time where both the measurement, the dynamic models and the resistive model are shown. It can thus be seen that the 3p3z dynamic model follows the measurement very well both for higher frequencies but also for the lower ones. The 2p2z model agrees quite well with the measurement as well, and only overestimates the voltage drop with a few percents. The 1p1z and the resistive model do however not agree well with the measurements and overestimate the voltage drop when a current is flowing in the cell (higher losses) and underestimates the voltage drop when no current is flowing through the cell. The resistive model is therefore only valid when a pure DC-current is flowing in the cells. However, this never occurs in a multilevel inverter drive system. Interesting to notice is that the EIS model underestimates the voltage drop and therefore the losses. The reason for this is that the parameters are subtracted at a very low magnitude of current, and the battery impedance is in this case slightly lower at these low current levels.

The resulting losses for case no 5, as was displayed in Fig. 6.5, as well as the other five cases are shown in Fig. 6.6 and the relative maximum voltage drop compared to the measurements can be seen in Table 6.4. It can be noted that the dynamic model and the measurements agree very well and



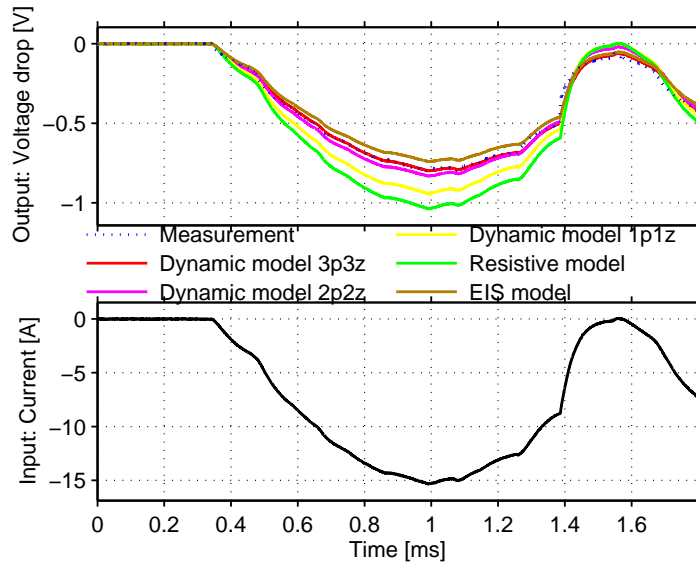


Figure 6.5: Battery current for operation point five when no input capacitor is used.

that the resistive model always overestimates the losses and the EIS model underestimates the losses. It can also be noted that the resistive model shows somewhat better agreement at lower frequencies (operating point one, two and three) compared to higher frequencies (operating point six).

Table 6.4: Maximum voltage drop for the six operating points relative to the measurement.

Case nr:	1	2	3	4	5	6
Measurement	100 %	100 %	100 %	100 %	100 %	100 %
3p3z	98 %	101 %	98 %	101 %	100 %	102 %
2p2z	98 %	101 %	101 %	105 %	104 %	108 %
1p1z	107 %	111 %	112 %	119 %	118 %	123 %
Resistive	118 %	122 %	124 %	131 %	130 %	136 %
EIS	91 %	94 %	91 %	94 %	93 %	95 %

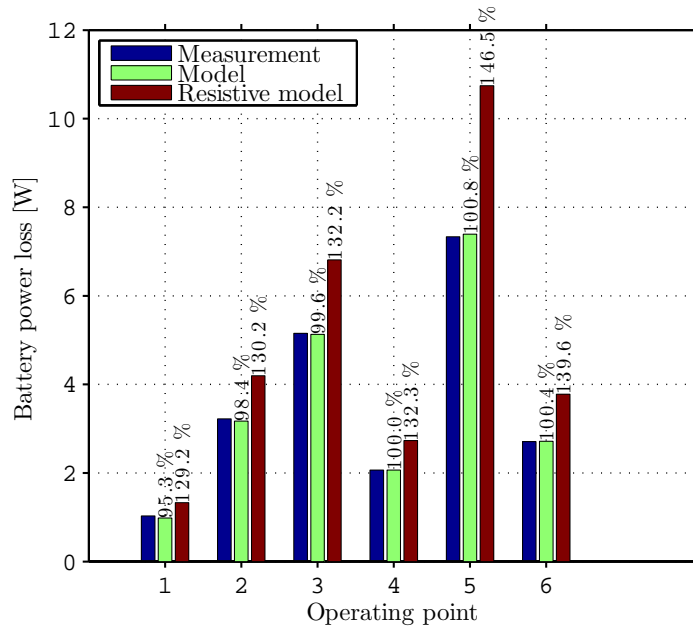


Figure 6.6: Calculated loss comparison between measurements, the dynamic model and a purely resistive model.

### 6.3 Drive cycle evaluation for battery losses

The five different battery models are now used in a drive cycle evaluation. The reference vehicle is used to calculate the operating points for the inverter for the NEDC cycle. The resulting total battery loss can be seen in Fig. 6.7

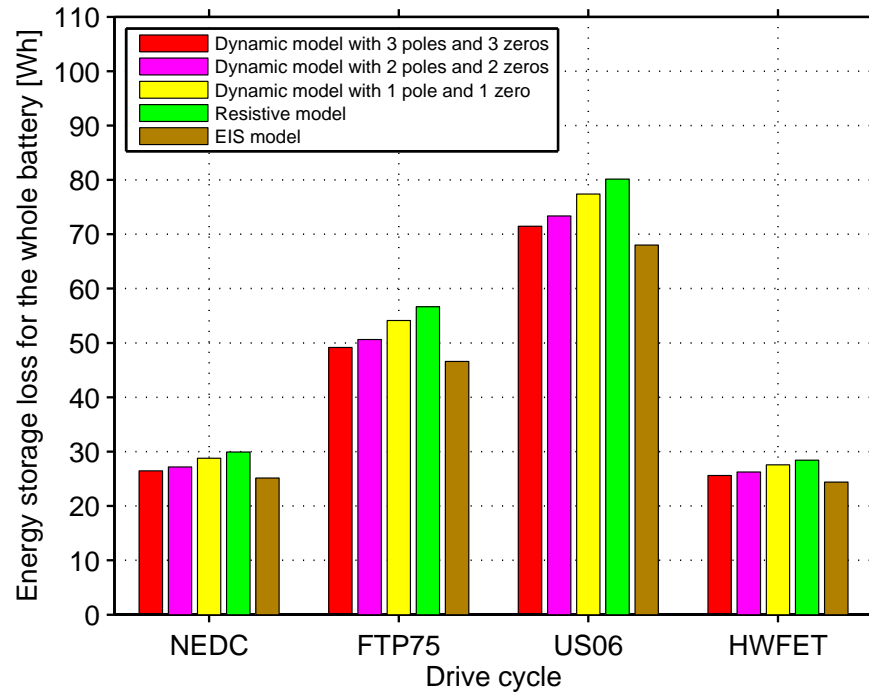


Figure 6.7: Calculated loss comparison between the models for different drive cycles.

together with the three other investigated drive cycles. It can be noted that the same behaviour is shown for all the drive cycles even though the car operates at very different speeds and accelerations in the four drive cycles. In the same way as for the single operating point verification, the resistive model shows a higher loss compared to the 3p3z dynamic model and the EIS model provides a lower loss prediction.



## Chapter 7

# Filter capacitor influence

As described in Section 4.1.3, capacitors can be put over the battery groups in order to alleviate the battery cells to some extent from ripple currents. In Chapter 5 two "end-point options" were tested but here a more through analysis of the capacitor influence is performed where various amounts are analysed. The impact will also be analysed for two different capacitor chemistries and the loss effect will be quantified.

### 7.1 System overview

To be able to analyse the impact of capacitors connected to the input of the H-bridges in a multilevel inverter, the experimental system is utilised where it is possible to connect various combinations of capacitors to the inputs. It should be mentioned that there are always capacitors located over the H-bridges in the experimental system to supply and absorb energy during the switching instances in order to avoid voltage spikes on the transistors. However, here the amount is increased above what is needed for the circuit to operate properly. Actually, since the switching instances occur very seldom, it is possible to switch more slowly and then these small capacitors are not needed. The further analysis is performed at 25 °C.

#### 7.1.1 Battery cell

The battery cell is modeled with the three time-constant Randles model presented in Fig. 6.1. The parameters used are derived through measurements and are presented under model "meas 3.23V 1Hz 28A 3p3z" in Table 6.1 but can also be seen below in Table 7.1.

For the full scale system the battery is described in Table 7.2 for each H-bridge to get an understanding of the physical dimensions of the system.

Table 7.1: Cell parameters.

Measurement:	R0 [ $m\Omega$ ]	R1 [ $m\Omega$ ]	R2 [ $m\Omega$ ]	R3 [ $m\Omega$ ]	C1 [F]	C2 [F]	C3 [F]	Fit [%]
3.23V 1Hz 28A	10.02	2.47	1.41	1.37	0.49	9.93	168.94	99.49

Table 7.2: Battery configuration. Values per H-bridge.













Nr of cells in series	Nr of cells in parallel	DC-resistance [ $m\Omega$ ]	Weight [kg]	Volume [L]
15	10	22.9	12.5	5.28

## 7.2 Capacitor configurations

Eight configurations of capacitances are selected together with one configuration without any input capacitances. Four of the configurations are based on a super capacitor chemistry and four configurations are based on an electrolytic chemistry. The parameters for configuration 1-8 and the case without any capacitances (configuration 0), are shown in Table 7.3. For verification purposes, configuration 0, configuration 4 and configuration 8 are scaled down to fit the experimental system. It should be noted that the electrolytic configuration (configuration 1-4) has about the same mass and volume as the super capacitance configuration (configuration 5-8). Accordingly, the capacitance is a consequence of this selection.



Table 7.3: Capacitor configurations, values per H-bridge.

Configuration:	Color:	Sort:	Capacitance [mF]	Resistance [mΩ]	Weight [kg]	Volume [L]
0		N/A	-	-	-	-
1		Electrolytic capacitor	5.87	52.5	0.55	0.37
2		Electrolytic capacitor	23.5	13.1	2.2	1.5
3		Electrolytic capacitor	41.1	7.5	3.9	2.6
4		Electrolytic capacitor	58.7	5.25	5.5	3.7
5		Super capacitor	4440	104	0.46	0.36
6		Super capacitor	17800	25.9	1.8	1.4
7		Super capacitor	31100	14.8	3.2	2.5
8		Super capacitor	44400	10.4	4.6	3.6
0 <sub>SS</sub> (Small Scale)		N/A	-	-	-	-
4 <sub>SS</sub> (Small Scale)		Electrolytic capacitor	22	14	0.14	0.098
8 <sub>SS</sub> (Small Scale)		Super capacitor	16700	27.6	0.12	0.094

### 7.3 Model verification

As in the previous chapter, the six operating points presented in Table 6.3 are used to perform measurements in the small scale system and the configurations 0, 4 and 8 are scaled down and called configuration  $0_{SS}$ ,  $4_{SS}$  and  $8_{SS}$ , see Table 7.3 (SS stands for small scale). The voltage drop and current are sampled to be able to calculate the losses. The current is also used as input to the models to calculate a simulated loss. These waveforms are presented for operating point 1 in Fig. 7.1.

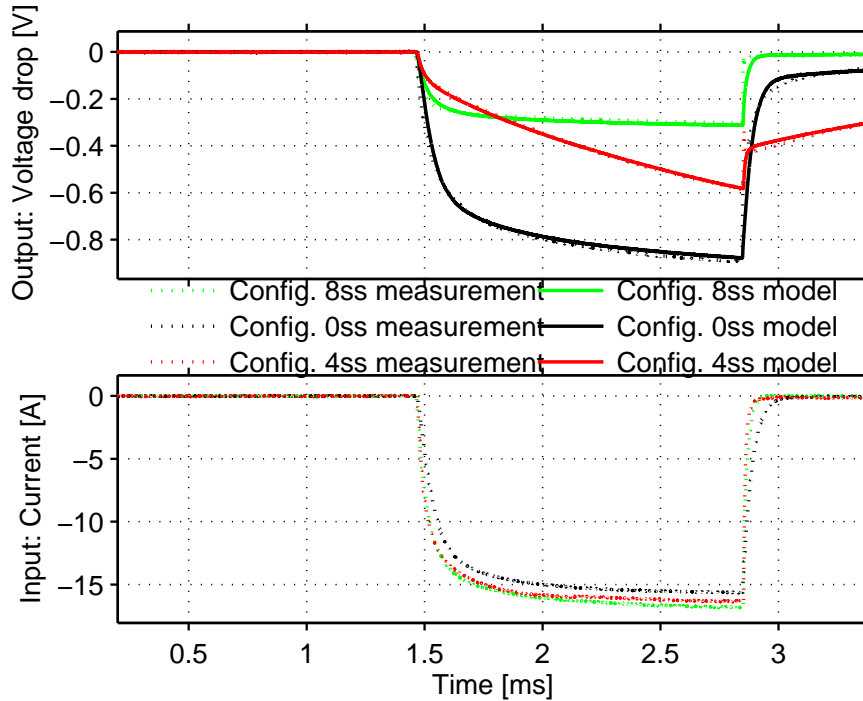


Figure 7.1: Simulations and measurements of the models in the small scale system for operating point 1.

It can be noted that the waveforms agree very well between the simulations and the measurements for each configuration. Almost the same current was used for the three measurements but as can be noticed in Fig. 7.1, there are some small variations so a loss comparison between the setups could not be specifically obtained by studying the figure even though the behaviour of the setups are very clearly illustrated. However, from the voltage-current relations the models could be verified individually.

The highest voltage drop is observed without the capacitances (configuration  $0_{SS}$ ) while the electrolytic capacitance (configuration  $4_{SS}$ ) holds the voltage very good in the beginning of the pulse due to their low resistance. Since the electrolytic capacitor does not have a very high capacitance, the voltage drop starts to increase quite quickly at the low frequency that operating point 1 has. The super capacitor configuration ( $8_{SS}$ ) shows a bit different behaviour since it has higher resistance but more capacitance. It shows a higher voltage drop in the beginning of the pulse compared to the electrolytic configuration but holds this voltage drop since the capacitance is very high.

The losses are calculated for all six operating points with all three configurations and compared with its measurements and presented in Table 7.4. Since the calculated losses agree within a few percents of the measurements, the models are concluded to be valid. Therefore the models will be used in further calculations of the losses during different drive cycles.

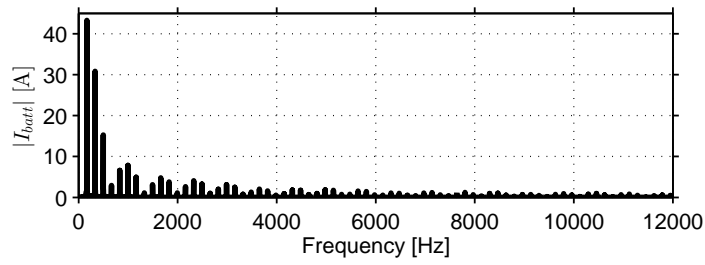
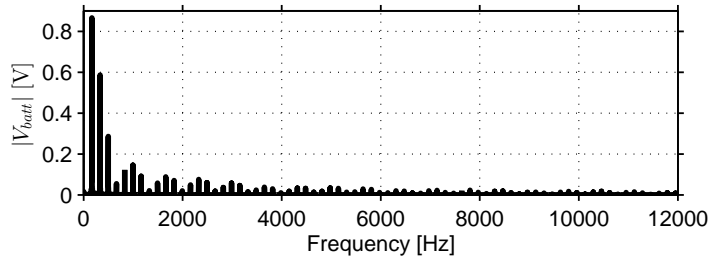
Table 7.4: Loss comparison between models and measurements for six operating points.

Configuration	Op1	Op2	Op3	Op4	Op5	Op6
$0_{SS}$	98.9 %	100.8 %	100.2 %	102.4 %	102.0 %	103.8 %
$4_{SS}$	100.4 %	99.4 %	99.7 %	101.5 %	102.2 %	102.8 %
$8_{SS}$	102.5 %	99.6 %	99.9 %	100.5 %	99.7 %	100.2 %

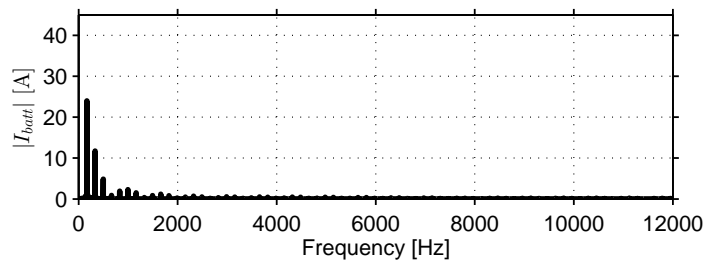
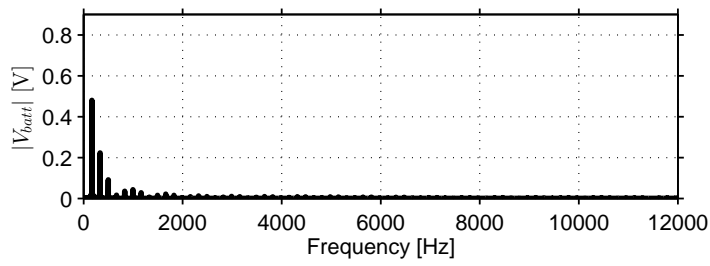
## 7.4 Frequency analysis

Operating point 1 and 6 are now selected for a more detailed harmonic analysis and simulations are performed for several configurations. In Fig. 7.2 the harmonic spectrum of the battery pack voltage and current are shown for configuration 0 (pure battery) and configuration 4 (big electrolytic capacitor) at operating point 1. It should be noted that the capacitors suppress the harmonic content in the battery to a very large extent, lowering the second harmonic with a factor of around 4 for both the voltage and current.

In Table 7.5, the harmonic content of the second, fourth and highest harmonic above 9 kHz are shown. The 9 kHz frequency is chosen as the lower limit due to that some EMI requirement reach down to this frequency [54]. For operating point 1 the super capacitors show the biggest improvement of the harmonic content due to the low frequency at operating point 1. At



(a) Configuration 0



(b) Configuration 4

Figure 7.2: Harmonic spectrum of the battery waveforms for operating point 1. Units in amplitude

operating point 6 the frequency is much higher, therefore the electrolytic capacitors show the best performance at operating point 6.

From an EMI perspective, it is important to minimize the voltage swings/ripple in the DC cables and all 'conducting surfaces', since these are the sources for radiated emissions. The maximum amplitude at frequencies above 9 kHz is reduced significantly for both chemistries of capacitors at operating point 1, leading to an improved EMI situation. For operating point 6, the electrolytic capacitors show the best improvement.

Table 7.5: Calculated harmonic content of the battery pack voltage for various filter capacitor configurations.

OP	Config.	2nd harmonic	4th harmonic	Highest above 9 kHz
OP1	0	866 mV	586 mV	17 mV
	1	827 mV	529 mV	13 mV
	4	480 mV	223 mV	4 mV
	5	729 mV	505 mV	15 mV
	8	297 mV	211 mV	6 mV
	Mix 1 and 5	776 mV	518 mV	14 mV
	Mix 4 and 8	389 mV	229 mV	5 mV
OP6	0	1179 mV	274 mV	30 mV
	1	634 mV	209 mV	23 mV
	4	194 mV	63 mV	7 mV
	5	714 mV	238 mV	27 mV
	8	302 mV	101 mV	11 mV
	Mix 1 and 5	672 mV	222 mV	25 mV
	Mix 4 and 8	238 mV	78 mV	9 mV

In Table 7.6, the second, fourth and sixth harmonic for the battery current are shown. Here it can be noted that there is a clear reduction of the current pulses stressing the battery with configuration 1-8 compared to configuration 0. For the low speed operating point 1, the second harmonic is filtered best with the super capacitors due to its low frequency. The fourth and sixth harmonic are lowered with around the same amount for the two capacitor chemistries. At operating point 6, the electrolytic capacitors show a much better improvement for all harmonics due to the higher frequency at this operating point.

Table 7.6: Calculated harmonic content of the battery pack current for various filter capacitor combinations.

OP	Config.	2nd harmonic	4th harmonic	6th harmonic
OP1	0	43 A	31 A	16 A
	1	41 A	28 A	13 A
	4	24 A	12 A	5 A
	5	36 A	27 A	13 A
	8	15 A	11 A	6 A
	Mix 1 and 5	39 A	27 A	13 A
	Mix 4 and 8	19 A	12 A	5 A
OP6	0	45 A	15 A	6 A
	1	34 A	11 A	4 A
	4	10 A	3 A	1 A
	5	39 A	13 A	5 A
	8	16 A	5 A	2 A
	Mix 1 and 5	36 A	12 A	5 A
	Mix 4 and 8	13 A	4 A	2 A

## 7.5 Drive cycle analysis

Configurations 1-8 from Table 7.3 and a mix between the chemistries are now used in simulations of the four drive cycles NEDC, FTP75, US06 and HWFET to be able to compare the performance. The battery current, capacitor current and voltage drop are shown in Fig. 7.3 to 7.5 for a small part of the drive cycle HWFET at  $t = 260$  s for configuration 0, 4, 8 and a mix between 4 & 8. The weight and volume of configuration 4 and 8 are very similar (a bit more for the electrolytic case) but the relation between the resistance and the capacitance are very different between the two chemistries. From the figures it can be seen that the electrolytic capacitor (configuration 4) has less resistance than the super capacitor (configuration 8) and holds the voltage well in the first period of time after the current is applied. However the capacitance is much smaller in configuration 4 compared to configuration 8 and after some hundreds of microseconds the voltage has dropped to a level lower than the super capacitor. Depending on the operating speed (frequency) of the car, the two chemistries have different advantages.

The total loss accumulation for the drive cycles are presented in Fig. 7.6. It can be noted that a substantial decrease of the accumulated battery loss occurs when placing capacitors to the input of the H-bridges of a multilevel

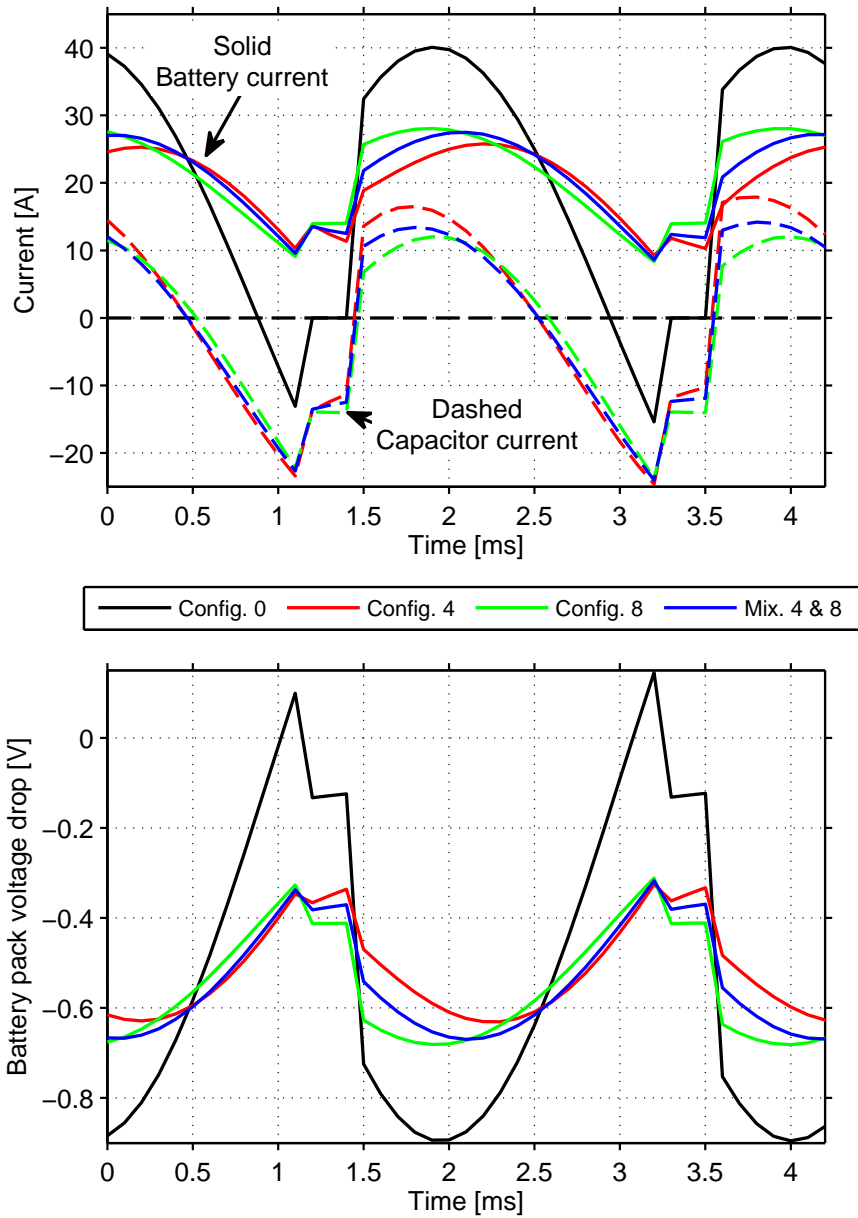


Figure 7.3: Simulations of the performance of the battery pack controlled with  $\alpha_1$ .

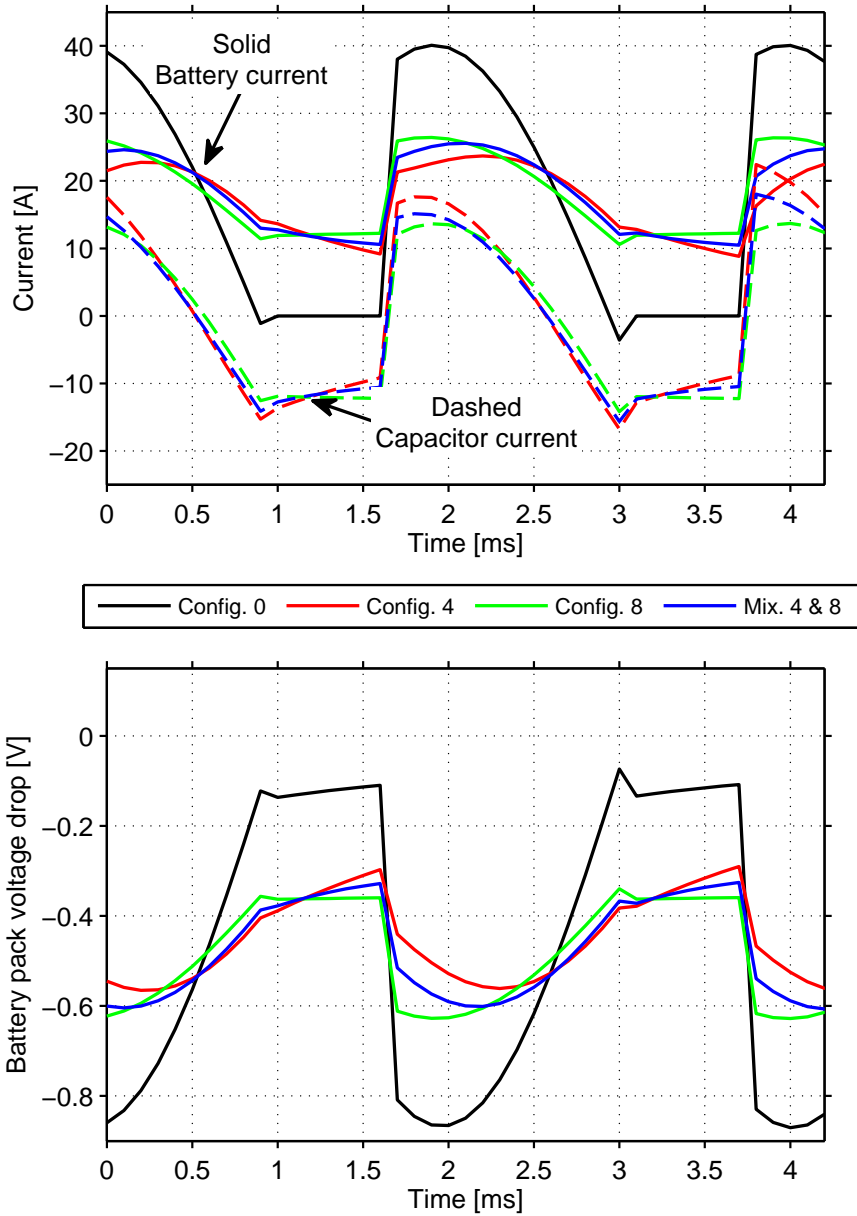


Figure 7.4: Simulations of the performance of the battery pack controlled with  $\alpha_2$ .



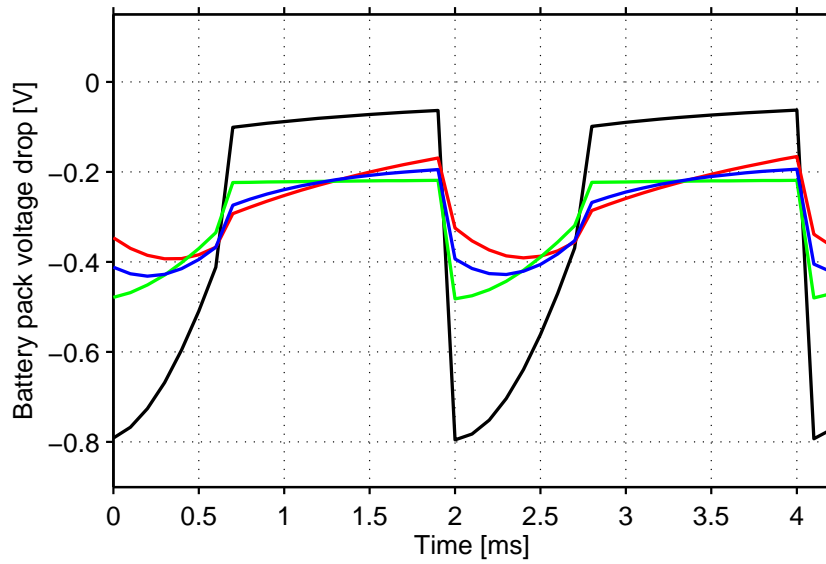
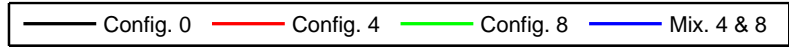
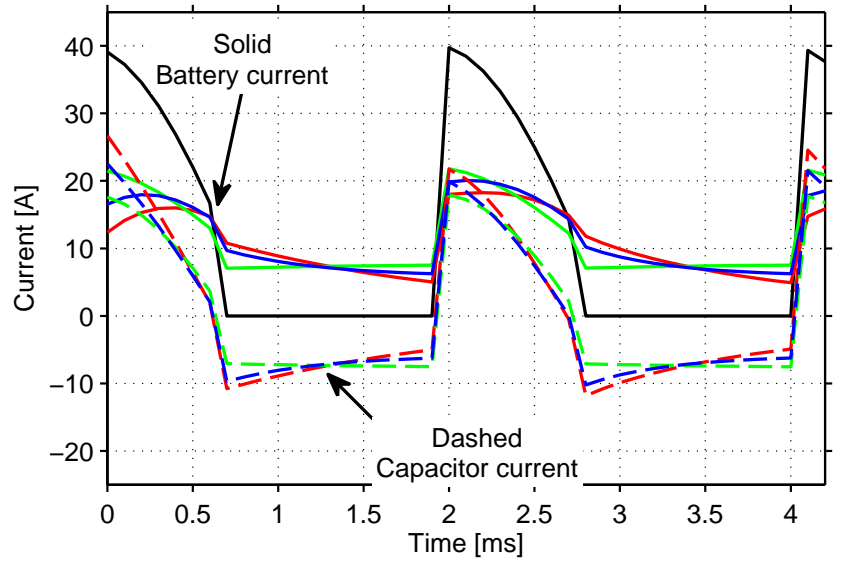


Figure 7.5: Simulations of the performance of the battery pack controlled with  $\alpha_3$ .

inverter used in electrified vehicles. The configurations with electrolytic capacitors (configuration 1-4) show slightly lower accumulated loss compared to the configurations with super capacitors (configurations 5-8) but they also have a bit higher mass.

With configurations 4 and 8 a reduction of the battery losses with around 30 % is achieved. However, we have now added a mass of around 5 kg per H-bridge to a battery pack weighing 12.5 kg per H-bridge. In Fig. 7.7 the loss reduction as a function of added weight is plotted. It can be noted that adding capacitors is always an advantage compared to adding more batteries for the four drive cycles unless a large increase of the energy storage is conducted. For all of the four drive cycles it is an advantage from a loss perspective to add a certain mass of electrolytic capacitors instead of adding super capacitors. Adding a mix of the two chemistries show a similar effect where the losses are at a level in between the super capacitor cases and the electrolytic cases.

If the mass of the capacitors were instead replaced with more battery cells, the losses in the battery would also be lowered, however, to a lower extent unless a large increase is conducted.

To sum up, the most realistic case is with the lowest amount of capacitors. Since lifetime issues are not analysed and the EMI performance is only briefly examined, maybe even less capacitors than configuration 1 and 5 could be the best choice.

## 7.6 Cold climate performance

For a cold battery it is of utmost important to avoid cyclings since the life time loss is substantial when the temperature goes to 0 deg C and below according to [55]. At cold temperatures the battery increases its resistance very much, an increase of approximately 400 % if the temperature drops from 25°C to 0°C. The here used capacitors does not increase their resistance in the same amount, roughly 20 % for the same temperature drop.

Operating point 1-6 are now simulated where the battery resistance is increased 400 % and the capacitor resistance is increased 20%. The resulting losses for configuration 0 (pure battery), 1 (small electrolytic capacitors) and 5 (small super capacitors) can be seen in Table 7.7. The loss reduction is significantly improved even for these small capacitors, about 2.5 times greater reduction for 0 deg C compared to 25 deg C. It can also be observed that the harmonic content is significantly reduced when adding these small capacitors.

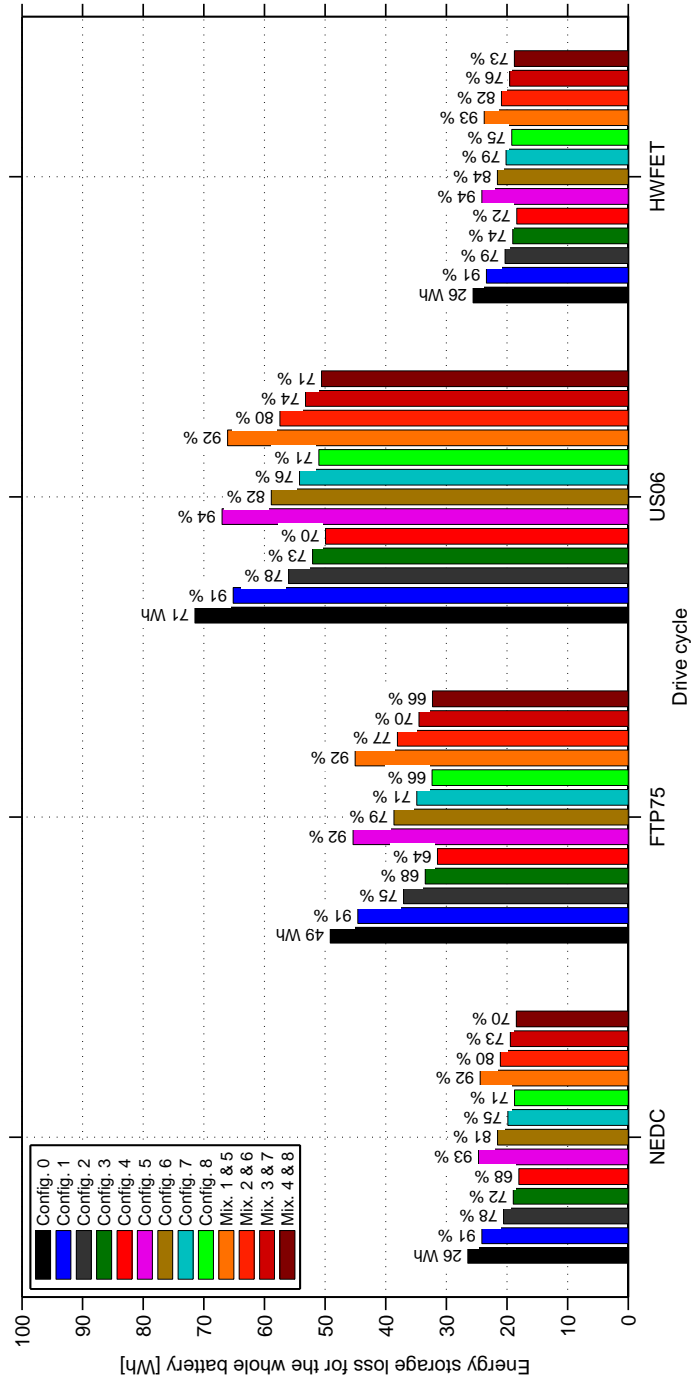


Figure 7.6: Battery loss for different drive cycles.

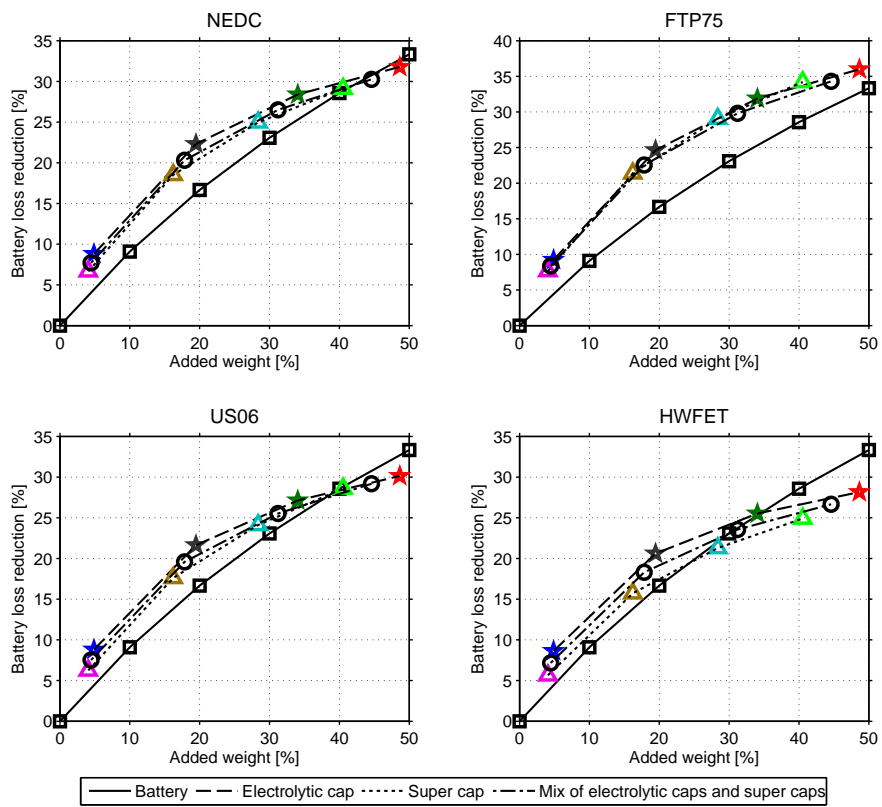


Figure 7.7: Calculated battery loss reduction for different mass of added filter components.

Table 7.7: Calculated battery performance in cold climate.

OP	Config.	Losses	Relative losses	Harmonics		
				2nd	4th	6th
OP1	0	750 W	100 %	43 A	31 A	16 A
	1	528 W	70 %	32 A	18 A	8 A
	5	522 W	70 %	24 A	18 A	9 A
OP2	0	2491 W	100 %	83 A	47 A	13 A
	1	1862 W	75 %	61 A	27 A	7 A
	5	1810 W	73 %	46 A	27 A	8 A
OP3	0	5158 W	100 %	117 A	51 A	24 A
	1	3968 W	77 %	87 A	29 A	12 A
	5	3859 W	75 %	65 A	29 A	13 A
OP4	0	3327 W	100 %	56 A	8 A	12 A
	1	2377 W	71 %	25 A	3 A	5 A
	5	2626 W	79 %	32 A	4 A	7 A
OP5	0	11987 W	100 %	108 A	22 A	10 A
	1	8871 W	74 %	48 A	9 A	4 A
	5	9680 W	81 %	62 A	13 A	6 A
OP6	0	9159 W	100 %	45 A	15 A	6 A
	1	7534 W	82 %	19 A	6 A	2 A
	5	7983 W	87 %	26 A	9 A	3 A



## Chapter 8

# Proposal for packaging of the inverter-battery unit and its cooling circuit

Traditionally, the inverter and battery are placed separately in the vehicle. Two separate cooling circuits are often used to cool the inverter and the battery since the battery should be operated at a cooler temperature. When using a multilevel inverter, a suggestion here is to place the inverter inside the battery and incorporate it into the already existing CVMM (Cell Voltage Monitoring Module), which are already in place in an electrified vehicle to monitor and balance the battery cells but also to measure the temperature.

The thermal impedance of the battery pack has a very long time constant, therefore it is not the peak battery loss that is of interest but the several minute average loss. Here, an average of one minute is used to find the maximum battery cooling need. This time constant is on the shorter side, so the analysis is made to be on the safe side. When designing the system, to ensure that the drive system does not get over heated, the vehicle should not be operated at high loads for a too long time period, see Fig. 8.1. If this occurs, then either the requirements of the vehicle must be reduced or the electrical components must be enlarged. To determine the maximum average battery loss, the US06 drive cycle is used since it is the most demanding among the four drive cycles analysed. The one minute base average battery loss during this drive cycle can be seen in Fig. 8.2.

As expected from Chapter 5, it can be noted that the MLI has substantially higher battery losses compared to the TLI for the 50 km driving range test vehicle.

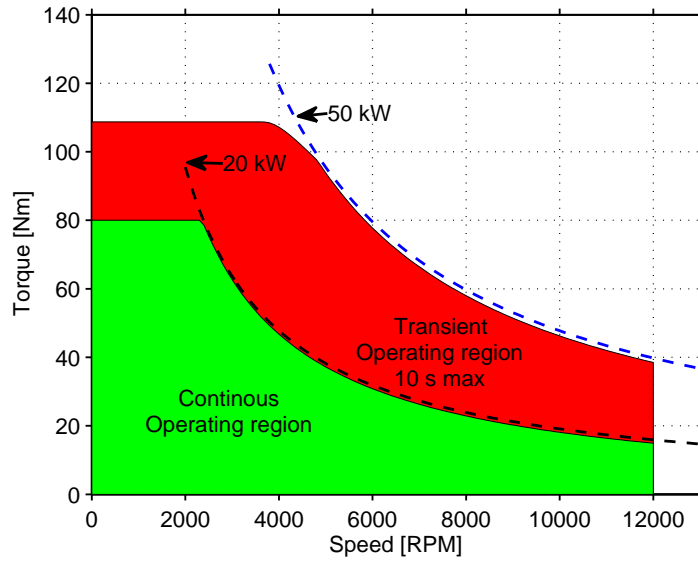


Figure 8.1: Transient limit of the drive system

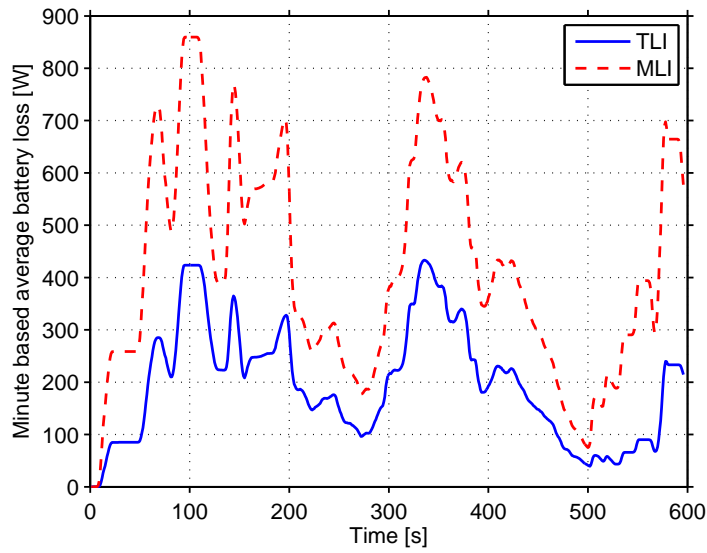


Figure 8.2: Calculated minute based average of the battery loss for the US06 drive cycle.



In order to calculate the temperature rise in the power electronics and the cooling circuit, a simple thermal network is used, see Fig. 8.3. The temperature rise between two nodes (node 1 and node 2) is calculated according to

$$\Delta T_{1-2} = R_{th_{1-2}} \cdot P_{1-2} \quad (8.1)$$

where  $\Delta T_{1-2}$  is the temperature difference between the two nodes,  $R_{th_{1-2}}$  is the thermal resistance between the two nodes and  $P_{1-2}$  is the heat transfer between the nodes. In steady state, which occurs very fast for a system with low thermal resistance and a low mass, the heat transfer is equal to the power dissipated in node 1,  $P_1$ , assuming that the heat transfer only occurs towards node 2.



Figure 8.3: Illustration of the simple thermal model used for steady state evaluation of the temperature rise of the drive train components.

The dynamics have been ignored in this expression. In order to take one important dynamic into account, the battery heat capacity, a one minute average loss value will be used. The more detailed approach is to use a thermal dynamic network, a Foster or Cauer model, however, the scope in this chapter is not to do a detailed temperature calculation, instead the ambition is to check that the integration of the inverter into the battery is possible from a temperature point of view. The analysis is therefore made conservative, overestimating the temperature increases.

When the heat transfer is dissipated into a cooling liquid with a fixed water flow, the temperature rise in the cooling liquid at this point can be expressed using

$$\Delta T_{water} = \frac{P_{water}}{C_p \cdot \frac{\Delta V}{\Delta t} \cdot \rho} \quad (8.2)$$

where  $C_p$  is the specific heat capacity for the cooling liquid,  $\rho$  is the density for the cooling liquid and  $\frac{\Delta V}{\Delta t}$  is the water flow.

## 8.1 Two-level inverter

To calculate the maximum requirements of the cooling circuit, the maximum loss of both the inverter and the battery are needed.

From Fig. 8.2, the maximum one minute average battery loss for the TLI battery corresponds to 433 W during the demanding US06 drive cycle. For a

water flow of 6 liters per minute, the temperature rise in the battery cooling circuit is given by

$$\Delta T_{water_{TLIbattery}} = \frac{P_{TLIbattery}}{C_p \cdot \frac{\Delta V}{\Delta t} \cdot \rho} = 1.1 \text{ K} \quad (8.3)$$

where  $C_p = 3770 \frac{J}{kg \cdot K}$ ,  $\rho = 1.036 \text{ kg/l}$  and  $\frac{\Delta V}{\Delta t} = 0.1 \text{ l/s}$  for a mixture consisting of 50 % water and 50 % ethylene glycol.

For the IGBT inverter used for the TLI system, which has a very small mass and has to be able to dissipate the loss immediately (on a second basis) to the cooling fluid, the maximum loss is equal to 1180 W and can be noted in the loss map for the TLI system, see Fig. 5.1. With the same water flow, the temperature increase for the water cooling circuit at the inverter would be equal to

$$\Delta T_{water_{TLIinverter}} = \frac{P_{TLIinverter}}{C_p \cdot \frac{\Delta V}{\Delta t} \cdot \rho} = 3.0 \text{ K} \quad (8.4)$$

at the worst operating point.

For a standard electrified vehicle, the cooling circuit for the electric machine and power electronics typically have a maximum temperature of 65 °C. According to the data sheet of the IGBT module, the thermal resistance per IGBT leg is equal to 0.1 K/W. With a water temperature of 65 °C the junction temperature in the IGBT modules would be

$$T_{junction_{TLIinverter}} = R_{th_{J-water}} \cdot \frac{P_{TLIinverter}}{3} + 65 = 105 \text{ °C} \quad (8.5)$$

which is an acceptable temperature, 20 °C below the maximum recommended value.

## 8.2 MOSFET equipped cell voltage monitor modules

When using a MLI instead of a TLI, the inverter consists of several modules that do not have to be placed as one unit. It is chosen here to place the H-bridges inside the battery, and the battery must of course be made slightly larger to support the additional H-bridges. In addition, the cooling circuit of the battery has to be upgraded with a higher flow, in order to handle the increased battery loss level.

A simple sketch of the proposed H-bridge inverter is shown in Fig. 8.4. In this picture, only the MOSFETs, the PCB and a heat sink is shown. In a real H-bridge inverter additional hardware is of course needed such as connectors, gate drivers and a processor etc. It is assumed that they can be

fitted between the MOSFETs. In Fig. 8.5 the H-bridge module from Fig. 8.4 is mounted on the already existing CVMM. It can be noted that the size increase is moderate compared to the original CVMM. The volume of the 9 added inverters is equal to 1.4 l (calculated from the measurements in Fig. 8.5), to be compared with over 100 l for a 10 kWh battery. Even though they are to be incorporated into the already existing battery circuit, the volume must be somewhat more increased due to an additional cooling need in the battery compartment. The extra cooling need will be determined in Section 8.2.5.

It should be noted that even though the MOSFETs do not have a mass to low pass filter the power loss, the PCB board and heat sink does. In the following analysis the PCB and heat sink is assumed to have a very low mass to be on the safe side in the analysis. This means that the maximum instantaneous (over one fundamental period) inverter loss is considered when comparing the temperature rise from junction to heat sink.

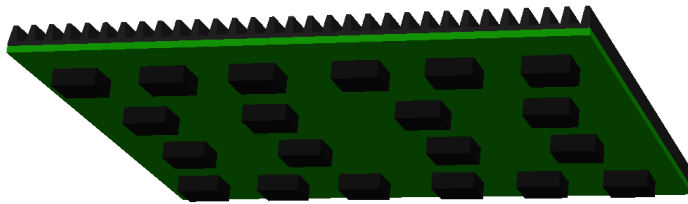


Figure 8.4: Proposed H-bridge inverter together with air cooled heat sink, one out of nine in the battery. Five MOSFETs are placed at each switch location, resulting in a total of 20 MOSFETs for each H-bridge.

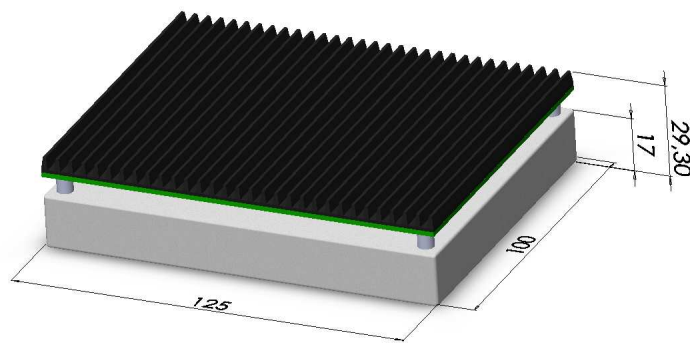


Figure 8.5: CVMM module with incorporated inverter and added heat sink.

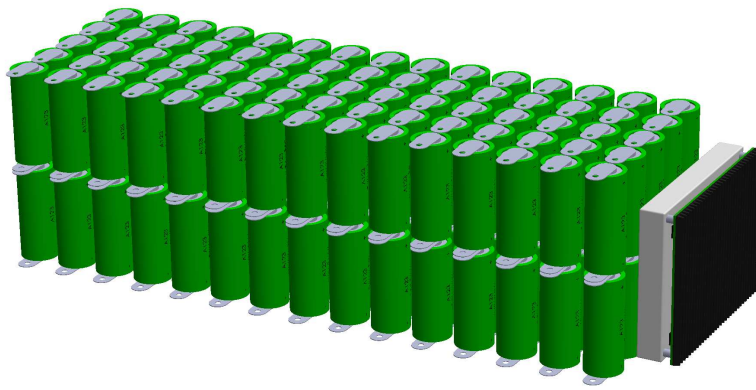


Figure 8.6: CVMM module with incorporated inverter together with battery module (150 cells).

### 8.2.1 Thermal resistance of the MOSFETs

The thermal resistance from the junction of the transistors to the case is according to the data sheet  $0.5 K/W$ . Since 20 transistors share the same loss (average over one fundamental period), the H-bridge equivalent thermal resistance from the junctions to the PCB board becomes

$$R_{th_{J-C}} = 0.025 K/W \quad (8.6)$$

when referring to the total H-bridge loss.

### 8.2.2 Thermal properties of the PCB

From the bottom side of the PCB, the heat flow must go through the whole PCB towards the heat sink. According to [56], the design of the copper layer has a very small influence of the thermal conductivity through the PCB, which instead is totally dominated by the glass fiber. Usually the PCB used is often FR4. According to the measurements done by [56] the thermal resistivity for heat conduction through an FR4 PCB is  $0.29 \frac{W}{m \cdot K}$  which would be too much for the design configuration illustrated in Fig. 8.4. However, if Metal-Core PCB (MCPCB) is used instead, the thermal resistivity is reduced significantly. In [57], the thermal resistance through a 1.5 mm PCB is calculated to  $0.2 K/W$  for a board of  $270 mm^2$ . The board in Fig. 8.4 has an area of  $12500 mm^2$ , a factor of 46 higher, resulting in a thermal resistance of

$$R_{th_{C-H}} = 0.004 K/W \quad (8.7)$$

between the equivalent transistor cases and the backside of the PCB.

### 8.2.3 Heat sink for CVMM

If the inverter loss would be dissipated through an air cooled heat sink, a heat sink is placed to cover the whole backside of the PCB. To calculate the thermal resistance of such a heat sink, data from a smaller available heat sink is used and extrapolated to the right geometry. Here, the heat sink "ICK SMD B 10 SA" from Fischer Elektronik GmbH is used [58] with a thermal resistance of  $35 K/W$  for an area of  $190 mm^2$ . The heat sink in Fig. 8.4 has an area of  $12500 mm^2$ , a factor of 66 higher, resulting in a thermal resistance of

$$R_{th_{H-A}} = 0.53 K/W \quad (8.8)$$

from the back side of the PCB to ambient air.

If instead the water cooling circuit of the battery is used to dissipate the heat from the power electronic, the thermal resistance would be even lower

than the air cooled heat sink, this would lead to a temperature rise from the junction of the transistors relative to the cooling water temperature of only a few degrees, which would be no problem at all, since the cooling fluid in a battery is typically low, at maximum  $40\text{ }^{\circ}\text{C}$ . Similarly as in (8.3), the water temperature would due to the MOSFET losses only rise

$$\Delta T_{water\_MLIinverter} = \frac{P_{MLIinverter}}{C_p \cdot \frac{\Delta V}{\Delta t} \cdot \rho} = 0.7\text{ K} \quad (8.9)$$

since the inverter loss are very low for the multilevel inverter case.

### 8.2.4 Cooling circuit temperature increase due to battery losses

The worst case battery loss when using a multilevel inverter without any filter capacitances to propel the vehicle is according to Fig. 8.2 equal to  $860\text{ W}$  when considering the minute based average. The temperature rise for a water flow of 6 liters per minute can then be calculated in the same way as in (8.3) and corresponds to

$$\Delta T_{water\_MLIbattery} = \frac{P_{MLIbattery}}{C_p \cdot \frac{\Delta V}{\Delta t} \cdot \rho} = 2.2\text{ K} \quad (8.10)$$

for the MLI case.

### 8.2.5 Resulting thermal analysis for the MOSFET-enhanced CVMM system

The total thermal resistance from the junction of the transistors to ambient air becomes

$$R_{th_{J-A}} = 0.025 + 0.004 + 0.53 = 0.56\text{ K/W} \quad (8.11)$$

when considering the total H-bridge loss for an air cooled inverter. The maximum inverter loss is according to Fig. 5.5 equal to  $280\text{ W}$ . This means that every H-bridge has to dissipate of  $280/9 = 31\text{ W}$ , the junction temperature will rise above ambient temperature with

$$\Delta T_{J-A} = R_{th_{J-A}} \cdot P_{H-bridge} = 0.56 \cdot 31 = 18\text{ K} \quad (8.12)$$

which is such a low temperature increase the it can be considered to be on the edge of over dimensioning.

A worst case scenario could be that one H-bridge has to deliver all the power. This happens if there is a very serious unbalance in the battery pack,

and the control system decides to use one H-bridge more than the others. If the output voltage is low at this instance, it could be that one H-bridge has to deliver all the power since only one H-bridge should be activated to create the desired voltage. That would lead to that the junction temperature increases to  $18 \cdot 3 = 54 \text{ K}$  above the ambient temperature in the battery compartment, which is still fully acceptable.

When using a water cooled inverter mounted at the battery, the loss from both systems increases the water temperature. The temperature difference between the input and output will for this case be equal to

$$\Delta T_{waterMLI_{total}} = \Delta T_{waterMLI_{battery}} + \Delta T_{waterMLI_{inverter}} = 2.9 \text{ K} \quad (8.13)$$

using (8.10) and (8.9) for the worst operating points.

### 8.3 Slim sized inverters

If the slim sized inverters presented in Section 5.4 are to be used, both the losses and the thermal performance of the system would change. For the slim sized TLI using the FS400 IGBT module, the inverter losses remain quite constant compared to the TLI with the FS800. However, the thermal resistance from the junction to the water is increased from  $Rth_{J-water} = 0.1 \text{ K/W}$  to  $Rth_{J-water} = 0.2 \text{ K/W}$  according to the data sheet. This would according to (8.5) result in a junction temperature of roughly

$$T_{junctionTLI_{inverter}} = Rth_{J-water} \cdot \frac{P_{TLI_{inverter}}}{3} + 65 = 144 \text{ }^\circ\text{C} \quad (8.14)$$

which is an unacceptable continuous temperature for the inverter if a good reliability is to be guaranteed. A degrading of the vehicle performance would have to be incorporated for some extreme occasions.

For the slim sized MLI case, the number of semiconductors is halved at the same time as the losses are about doubled. The equivalent thermal resistance from the junction of the 10 MOSFETs placed on each PCB then becomes

$$Rth_{J-C} = 0.05 \text{ K/W}. \quad (8.15)$$

Since the PCB and heat sink has the same size and performance the resulting thermal resistance from the junctions of the 10 MOSFETs to ambient air becomes

$$Rth_{J-A} = 0.05 + 0.004 + 0.53 = 0.59 \text{ K/W}. \quad (8.16)$$

which is just a slight increase since the thermal resistance from the heat sink to ambient air is the dominating part. With a worst case power loss of

$P_{H-bridge} = 560/9 = 62 \text{ W}$  per H-bridge, the junction temperature rise from ambient air temperature would be

$$\Delta T_{J-A} = R_{th_{J-A}} \cdot P_{H-bridge} = 0.59 \cdot 62 = 36 \text{ K}. \quad (8.17)$$

This is definitely acceptable even if the ambient air is very warm. One should also keep in mind that the heat sink has a thermal mass due to its size. Since the largest part of the thermal resistance is between the heat sink and ambient air, the MLI setup can withstand much higher losses for a short period of time than the steady state calculated ones.



## Chapter 9

# Conclusions

The investigation of using multilevel inverters (MLI) in electrified vehicles (EVs) shows that this inverter type has a great potential from an efficiency point of view. By reducing the voltage steps applied to the electric machine, as well as the switching frequency and slew rates, the EMI in the motor phase cables are reduced. The power loss in the power electronics is reduced due to the possibility to use the MOSFET technology and a system where the power electronics is placed in the already existing battery voltage measurement modules is proposed. These modules are placed inside the battery casing but since the losses are low, the heat dissipation of the power electronics can easily be dealt with either with internal air cooling and/or conduction into the already existing water cooling circuit for the battery.

Due to three separate single-phase systems, the battery modules are subject to a current with the second harmonic of the motor frequency. This increases the losses in the battery, especially at operating points where a lot of reactive power flowing in the electric machine is present. The drive cycle analysis shows that during most drive cycles the MLI drive system is the beneficial choice from a loss perspective compared to the TLI. In the commonly used NEDC the total inverter-battery losses are reduced with 30 % and in the in USA commonly used FTP75 by 23 % when using a battery with an energy content of only 10 *kWh* and without any filter capacitors. Only during the highly dynamic US06, the accumulated loss energy is larger (by 11 %) for the MLI system compared to the classical two-level inverter system.

If a larger battery with an energy content of 40 *kWh* is used, the battery loss is reduced, and the MLI system shows an even greater performance and potential due to that the battery losses are no longer dominant. For the NEDC drive cycle, the loss reduction is now as large as 75 % and for the

demanding US06 around 47 % when using the MLI system without filter capacitors compared to the TLI system for the combined battery-inverter losses.

Since the MLI forces very uneven waveforms in the battery it was needed to use a more detailed battery model compared with the case when a TLI system is investigated. Several models has been developed, parameterised and verified and by using a Randles model consisting of three poles and three zeros, the best accuracy was achieved. The selected battery model was experimentally verified and shows a good match to the measurements over a wide range of operating points. For the MLI system, a 30 % reduction of the predicted battery loss is achieved compared to using a purely resistive battery model. This is mainly due to the filtering effect of the double layer capacitance in the battery cell.

By placing capacitors to the input of the H-bridges in the MLI system, the battery current ripple is reduced. For low speed driving, super capacitors improves the performance more than using electrolytic capacitors, and at high speed driving the low resistance electrolytic capacitors are the most beneficial choice for a certain added mass. In the investigated examples, from a loss perspective, it is always beneficial to add a certain mass of capacitors compared to adding more battery cells (up to extreme limits), which could facilitate the cooling of the battery in addition to enhancing the driving range. For a cold battery the advantages are even larger since capacitors does not increase their inner resistance at all as much compared to the increase in the battery cells. This leads to that the performance at cold climate is significantly improved, even with a small amount of filter capacitors. Furthermore, worth mentioning is that by adding capacitors, the EMI spectrum from the battery cable and cells is also significantly lowered.

To sum up, from the energy efficiency point of view as well as from the packaging point of view, the MLI system shows a good potential compared to the TLI system.

## Chapter 10

# Future Work

This thesis has addressed and analysed some aspects of the possibility to use a multilevel inverter in electrified vehicles instead of the two-level inverter. However, some aspects and topics need further investigations in order to determine the suitability of the system. Following is a list of proposed investigations.

- With a MLI the possibility to take out other voltage levels can be made. One level can for example directly supply the 12 V system and the MLI could still make sure that this level is balanced with the remaining levels. The vehicle could then be made cheaper, since no DC/DC converter would be needed. The need for galvanic insulation in this case could on the other hand be a problem and needs further investigation.
- Investigate how the performance of a MLI would be when using more levels. What is the optimum for different drive cycles and car sizes?
- At low frequencies or at 0 Hz, the machine can not operate with selective harmonic elimination due to that the motor current would not be sinusoidal. Investigation about when it is necessary to start using PWM is accordingly needed. Since the MOSFETs has much lower switching losses, it could be beneficial use PWM at all speeds, without increasing the losses very much.
- The MLI has the opportunity to control from which modules the energy should be taken from, it can therefore also be used to control where the losses takes place. If one inverter or battery becomes too hot the MLI can be controlled to use this level less. Investigation about how this control can be made, and the benefits from it can be of interest.

- If a switch and/or in the MLI malfunctions, and is detected, the inverter can be controlled to keep operating without using that level, making the MLI a fault tolerant system. In vehicles this is a very important feature and investigation about the subject is of great interest.
- Investigation about different modulation strategies is of great importance. Reference [59] and [60] for example, show that space vector modulation is an alternative for MLI and shows good performance.
- Since the MLI can choose from which battery groups the energy should be taken from, it could be beneficial to compose the battery storage from different sorts of batteries and maybe even super capacitors. For very urban drive cycles it could be beneficial to use the super capacitors for acceleration and deceleration, and use the batteries as the average energy supply, reducing the losses.
- The economical analysis as well as life cycle analysis of having a MLI system instead of a TLI system are needed.

## References

- [1] R. Roy and J. Ghouili, "Numerical simulation of a multipowered onboard drive train," in *Electrical and Computer Engineering, 2004. Canadian Conference on*, vol. 4, may 2004, pp. 2069 – 2072 Vol.4.
- [2] S. Imai, N. Takeda, and Y. Horii, "Total efficiency of a hybrid electric vehicle," in *Power Conversion Conference - Nagaoka 1997., Proceedings of the*, vol. 2, aug 1997, pp. 947 –950 vol.2.
- [3] M. Ceraolo, A. di Donato, and G. Franceschi, "A general approach to energy optimization of hybrid electric vehicles," *Vehicular Technology, IEEE Transactions on*, vol. 57, no. 3, pp. 1433 –1441, may 2008.
- [4] N. Mutoh, Y. Hayano, H. Yahagi, and K. Takita, "Electric braking control methods for electric vehicles with independently driven front and rear wheels," *Industrial Electronics, IEEE Transactions on*, vol. 54, no. 2, pp. 1168 –1176, april 2007.
- [5] D. Gao, C. Mi, and A. Emadi, "Modeling and simulation of electric and hybrid vehicles," *Proceedings of the IEEE*, vol. 95, no. 4, pp. 729 –745, april 2007.
- [6] J. Wu, A. Emadi, M. Duoba, and T. Bohn, "Plug-in hybrid electric vehicles: Testing, simulations, and analysis," in *Vehicle Power and Propulsion Conference, 2007. VPPC 2007. IEEE*, sept. 2007, pp. 469 –476.
- [7] P.-S. Kim, "Cost modeling of battery electric vehicle and hybrid electric vehicle based on major parts cost," in *Power Electronics and Drive Systems, 2003. PEDS 2003. The Fifth International Conference on*, vol. 2, nov. 2003, pp. 1295 – 1300 Vol.2.
- [8] C. Chan, "The state of the art of electric, hybrid, and fuel cell vehicles," *Proceedings of the IEEE*, vol. 95, no. 4, pp. 704 –718, april 2007.
- [9] C. Chan and Y. Wong, "The state of the art of electric vehicles technology," in *Power Electronics and Motion Control Conference, 2004. IPEMC 2004. The 4th International*, vol. 1, aug. 2004, pp. 46 –57 Vol.1.

- [10] C. Chan and K. Chau, "Power electronics challenges in electric vehicles," in *Industrial Electronics, Control, and Instrumentation, 1993. Proceedings of the IECON '93., International Conference on*, nov 1993, pp. 701–706 vol.2.
- [11] J. Miller, "Power electronics in hybrid electric vehicle applications," in *Applied Power Electronics Conference and Exposition, 2003. APEC '03. Eighteenth Annual IEEE*, vol. 1, feb. 2003, pp. 23–29 vol.1.
- [12] Z. Shen and I. Omura, "Power semiconductor devices for hybrid, electric, and fuel cell vehicles," *Proceedings of the IEEE*, vol. 95, no. 4, pp. 778–789, april 2007.
- [13] F. Peng, W. Qian, and D. Cao, "Recent advances in multilevel converter/inverter topologies and applications," in *Power Electronics Conference (IPEC), 2010 International*, 2010, pp. 492–501.
- [14] M. Jongerden and B. Haverkort, "Which battery model to use?" *Software, IET*, vol. 3, no. 6, pp. 445–457, december 2009.
- [15] M. Einhorn, F. Conte, C. Kral, and J. Fleig, "Comparison, selection, and parameterization of electrical battery models for automotive applications," *Power Electronics, IEEE Transactions on*, vol. 28, no. 3, pp. 1429–1437, March 2013.
- [16] G. Plett, "High-performance battery-pack power estimation using a dynamic cell model," *Vehicular Technology, IEEE Transactions on*, vol. 53, no. 5, pp. 1586–1593, Sept 2004.
- [17] B. Enache, E. Lefter, and C. Stoica, "Comparative study for generic battery models used for electric vehicles," in *Advanced Topics in Electrical Engineering (ATEE), 2013 8th International Symposium on*, May 2013, pp. 1–6.
- [18] Z. Zheng, K. Wang, L. Xu, and Y. Li, "A hybrid cascaded multilevel converter for battery energy management applied in electric vehicles," *Power Electronics, IEEE Transactions on*, vol. 29, no. 7, pp. 3537–3546, July 2014.
- [19] R. Kroeze and P. Krein, "Electrical battery model for use in dynamic electric vehicle simulations," in *Power Electronics Specialists Conference, 2008. PESC 2008. IEEE*, june 2008, pp. 1336–1342.
- [20] A. Shafiei, A. Momeni, and S. Williamson, "Battery modeling approaches and management techniques for plug-in hybrid electric vehicles," in *Vehicle Power and Propulsion Conference (VPPC), 2011 IEEE*, sept. 2011, pp. 1–5.

- [21] A. Hentunen, T. Lehmuspelto, and J. Suomela, "Electrical battery model for dynamic simulations of hybrid electric vehicles," in *Vehicle Power and Propulsion Conference (VPPC), 2011 IEEE*, Sept 2011, pp. 1–6.
- [22] L. Y. Wang, M. P. Polis, G. Yin, W. Chen, Y. Fu, and C. Mi, "Battery cell identification and soc estimation using string terminal voltage measurements," *Vehicular Technology, IEEE Transactions on*, vol. 61, no. 7, pp. 2925–2935, Sept 2012.
- [23] J. Groot, *State-of-Health Estimation of Li-ion Batteries: Cycle Life Test Methods*. Licentiate Thesis, Chalmers University of Technology, 2012.
- [24] S. Haghbin, K. Khan, S. Lundmark, M. Alaküla, O. Carlson, M. Leksell, and O. Wallmark, "Integrated chargers for ev's and phev's: examples and new solutions," in *Electrical Machines (ICEM), 2010 XIX International Conference on*, sept. 2010, pp. 1–6.
- [25] L. Tolbert, F. Peng, and T. Habetler, "Multilevel inverters for electric vehicle applications," in *Power Electronics in Transportation, 1998*, oct 1998, pp. 79–84.
- [26] A. Verma, P. Thakura, K. Jana, and G. Buja, "Cascaded multilevel inverter for hybrid electric vehicles," in *Power Electronics (IICPE), 2010 India International Conference on*, jan. 2011, pp. 1–6.
- [27] O. Josefsson, A. Lindskog, S. Lundmark, and T. Thiringer, "Assessment of a multilevel converter for a phev charge and traction application," in *Electrical Machines (ICEM), 2010 XIX International Conference on*, sept. 2010, pp. 1–6.
- [28] O. Josefsson, T. Thiringer, S. Lundmark, and H. Zelaya, "Evaluation and comparison of a two-level and a multilevel inverter for an ev using a modularized battery topology," in *IECON2012*, 2012.
- [29] M. Dahidah and V. Agelidis, "Selective harmonic elimination multilevel converter control with variant dc sources," in *Industrial Electronics and Applications, 2009. ICIEA 2009. 4th IEEE Conference on*, may 2009, pp. 3351–3356.
- [30] E. Guan, P. Song, M. Ye, and B. Wu, "Selective harmonic elimination techniques for multilevel cascaded h-bridge inverters," in *Power Electronics and Drives Systems, 2005. PEDS 2005. International Conference on*, vol. 2, nov. 2005, pp. 1441–1446.
- [31] W. Shuanghong, Z. Qionghua, M. Zhiyuan, and Z. Libing, "Implementation of a 50 kw 4-phase switched reluctance motor drive system for hev," in *Electromagnetic Launch Technology, 2004. 2004 12th Symposium on*, may 2004, pp. 518–522.

- [32] (2013, Feb.) Tesla motors. [Online]. Available: <http://www.teslamotors.com/roadster/technology/motor>
- [33] Y. Guan, Z. Zhu, I. Afinowi, J. Mipo, and P. Farah, "Design of synchronous reluctance and permanent magnet synchronous reluctance machines for electric vehicle application," in *Electrical Machines and Systems (ICEMS), 2014 17th International Conference on*, Oct 2014, pp. 1853–1859.
- [34] M. Ehsani, K. Rahman, and H. Toliyat, "Propulsion system design of electric and hybrid vehicles," *Industrial Electronics, IEEE Transactions on*, vol. 44, no. 1, pp. 19–27, feb 1997.
- [35] J. Lindström, *Development of an Experimental Permanent-Magnet Motor Drives*. Licentiate Thesis, Chalmers University of Technology, 1999.
- [36] J. Hellsing, *Design and Optimization of a Permanent Magnet Motor for a Hybrid Electric Vehicle*. Licentiate Thesis, Chalmers University of Technology, 1998.
- [37] C. Du-Bar, *Design of a fault-tolerant fractional slot PMSM for a vehicle application*. Licentiate Thesis, Chalmers University of Technology, 2014.
- [38] I. Khan, "Battery chargers for electric and hybrid vehicles," in *Power Electronics in Transportation, 1994. [Proceedings]*, oct 1994, pp. 103–112.
- [39] L. Tolbert, F. Z. Peng, T. Cunnyngham, and J. Chiasson, "Charge balance control schemes for cascade multilevel converter in hybrid electric vehicles," *Industrial Electronics, IEEE Transactions on*, vol. 49, no. 5, pp. 1058–1064, oct 2002.
- [40] M. Yilmaz and P. T. Krein, "Review of battery charger topologies, charging power levels, and infrastructure for plug-in electric and hybrid vehicles," *Power Electronics, IEEE Transactions on*, vol. 28, no. 5, pp. 2151–2169, may 2013.
- [41] L. Wang, J. Liang, G. Xu, K. Xu, and Z. Song, "A novel battery charger for plug-in hybrid electric vehicles," in *Information and Automation (ICIA), 2012 International Conference on*, june 2012, pp. 168–173.
- [42] F. Lacressonniere and B. Cassoret, "Converter used as a battery charger and a motor speed controller in an industrial truck," in *Power Electronics and Applications, 2005 European Conference on*, 0-0 2005, pp. 7 pp. – P.7.



- [43] D.-G. Woo, G.-Y. Choe, J.-S. Kim, B.-K. Lee, J. Hur, and G.-B. Kang, "Comparison of integrated battery chargers for plug-in hybrid electric vehicles: Topology and control," in *Electric Machines Drives Conference (IEMDC), 2011 IEEE International*, may 2011, pp. 1294 –1299.
- [44] P. Haaf and J. Harper, "Diode reverse recovery and its effect on switching losses," unpublished. [Online]. Available: <http://www.fairchildsemi.com/onlineseminars/diodeReverseRecoverySwitchingLosses.pdf>
- [45] D. Graovac and M. Pürschel, "Igbt power losses calculation using the data-sheet parameters," unpublished. [Online]. Available: <http://www.element14.com/community/servlet/JiveServlet/download/20553-1-3493/IGBT\%20Power\%20Losses\%20Calculation\%20using\%20the\%20Data\%20Sheet\%20Parameters.pdf>
- [46] J. Jose, G. Goyal, and M. Aware, "Improved inverter utilisation using third harmonic injection," in *Power Electronics, Drives and Energy Systems (PEDES) 2010 Power India, 2010 Joint International Conference on*, dec. 2010, pp. 1 –6.
- [47] A123Systems, "Datasheet, battery cell anr26650m1a," unpublished. [Online]. Available: [http://e-motion.lt/wp-content/uploads/2010/01/ANR26650M1A\\_Datasheet.pdf](http://e-motion.lt/wp-content/uploads/2010/01/ANR26650M1A_Datasheet.pdf)
- [48] RIFA/KEMET, "Datasheet, electrolytic capacitor peh169gd5220q," unpublished. [Online]. Available: <http://www.kemet.com/>
- [49] Ioxus, "Datasheet, super capacitor rsc2r7107sr," unpublished. [Online]. Available: <http://www.ioxus.com/>
- [50] Infineon, "Datasheet, fs800r07a2e3," unpublished. [Online]. Available: [http://www.infineon.com/dgdl/Infineon-FS800R07A2E3-DS-v03\\_00-en\\_de.pdf?fileId=db3a304320d39d590121b0581fc82d8d](http://www.infineon.com/dgdl/Infineon-FS800R07A2E3-DS-v03_00-en_de.pdf?fileId=db3a304320d39d590121b0581fc82d8d)
- [51] —, "Datasheet, ipb025n10n3g," unpublished. [Online]. Available: [http://www.infineon.com/dgdl/Infineon-IPB025N10N3G-DS-v02\\_03-en.pdf?fileId=db3a30431ce5fb52011d1ab1d9d51349](http://www.infineon.com/dgdl/Infineon-IPB025N10N3G-DS-v02_03-en.pdf?fileId=db3a30431ce5fb52011d1ab1d9d51349)
- [52] I. Rectifier, "Datasheet, irf1324s-7ppbf," unpublished. [Online]. Available: <http://www.irf.com/product-info/datasheets/data/irf1324s-7ppbf.pdf>
- [53] V. Schwarzer and R. Ghorbani, "Drive cycle generation for design optimization of electric vehicles," *Vehicular Technology, IEEE Transactions on*, vol. 62, no. 1, pp. 89–97, Jan 2013.

- [54] General Administration of Quality Supervision, “GB/T 18387-2008: Limits and test method of electric and magnetic field strength from electric vehicles, 9 kHz to 30 MHz,” National Standard of the People’s Republic of China, China, Standard, Sept 2008.
- [55] A. Narula, “Modeling of ageing of lithium-ion battery at low temperatures,” 2014, 60.
- [56] K. Azar and J. Graebner, “Experimental determination of thermal conductivity of printed wiring boards,” in *Semiconductor Thermal Measurement and Management Symposium, 1996. SEMI-THERM XII. Proceedings., Twelfth Annual IEEE*, Mar 1996, pp. 169–182.
- [57] I. Cree, “Optimizing pcb thermal performance for cree® xlamp® leds,” unpublished. [Online]. Available: [www.cree.com/xlamp\\_app\\_notes/pcb\\_thermal](http://www.cree.com/xlamp_app_notes/pcb_thermal)
- [58] F. E. GmbH, “Datasheet, ick smd b 10 sa,” unpublished. [Online]. Available: <http://www.fischerelektronik.de/>
- [59] X. Hou, Y. Li, and Y. Liu, “A novel general space vector modulation algorithm for multilevel inverter based on imaginary coordination,” in *Power Electronics and Drive Systems, 2003. PEDS 2003. The Fifth International Conference on*, vol. 1, nov. 2003, pp. 392 – 396 Vol.1.
- [60] Y. Li, Y. Gao, and X. Hou, “A general svm algorithm for multilevel converters considering zero-sequence component control,” in *Industrial Electronics Society, 2005. IECON 2005. 31st Annual Conference of IEEE*, nov. 2005, p. 6 pp.